Departamento de Biología Molecular
Facultad de Ciencias
Universidad Autónoma de Madrid

FABRICATION AND CHARACTERISATION OF A MICROPATTERN-BASED PLATFORM TO MODEL EPITHELIAL TUBULOGENESIS AND TO PERFORM NEPHROTOXICITY ASSAYS

FABRICACIÓN Y CARACTERIZACIÓN DE UN SISTEMA DE CULTIVO BASADO EN MICROPATRONES ADHERENTES PARA ESTUDIAR LA TUBULOGÉNESIS EPITELIAL Y REALIZAR ENSAYOS DE NEFROTOXICIDAD

MADRID, 2018

Minerva Bosch Fortea

Licenciada en Biotecnología

Fernando Martín Belmonte

Thesis supervisor

Esta tesis ha sido realizada en el Centro de Biología Molecular Severo Ochoa (CSIC-UAM) bajo la supervisión del Dr. Fernando Martín Belmonte, Investigador Científico del CSIC.

La realización de esta tesis ha sido posible gracias al programa de becas de doctorado de la Obra Social "La Caixa" y a la beca de movilidad Short-term Fellowships de la "European Molecular Biology Organization" concedidas a Minerva Bosch Fortea. Este trabajo ha estado financiado por subvenciones del MINECO (BFU2015-71244-ERC; BFU2014-52125-REDT; BFU2014-57831), y la fundación de Ramón Areces a F M-B.

SUMMARY

La morfogénesis de algunos tubos epiteliales, como el sistema gastrointestinal o el páncreas, ocurre a través de un mecanismo de formación del lumen *de novo.* Durante este proceso, se generan múltiples lúmenes a lo largo del eje anteroposterior del órgano, los cuales se expanden y fusionan con los lúmenes adyacentes para formar una cavidad única. Debido a su complejidad, recrear este proceso en sistemas reduccionistas *in vitro* resulta muy complicado. Un método de cultivo con el potencial de simular y reproducir este proceso *in vitro* supondría una herramienta muy potente para estudiar los mecanismos moleculares implicados en la formación de tubos, ya sería un modelo más fisiológico que los que existen actualmente. En este sentido, hemos desarrollado un sistema de cultivo en micropatrones adherentes, generado mediante técnicas de microfabricación, que permite que las células epiteliales adquieran una arquitectura tridimensional y formen estructuras tubulares mediante un proceso que se asemeja a la tubulogénesis *in vivo*.

Podemos modificar la estructura de dichos túbulos cambiando la forma del micropatrón, lo que afecta a la formación del lumen y a la morfología, la proliferación y la orientación del huso mitótico. El sistema de micropatrones también permite variar la composición de la matriz extracelular y la rigidez del sustrato de cultivo, lo que resulta útil a la hora de analizar la respuesta morfológica a dichos factores. De hecho, los tubos cultivados sobre laminina tienen características morfológicas distintas a los cultivados en fibronectina a causa de diferencias en la adhesión. Además, la rigidez de la matriz controla el ensamblaje de las adhesiones focales y afecta a procesos de mecanotransducción, como la expresión y localización de YAP y provoca cambios en la contractilidad mediada por actomiosina

Los mecanismos que controlan el proceso de resolución de lúmenes no se conocen en profundidad. Utilizando estos sistemas de cultivo, hemos analizado el papel de la polaridad planar, la contractilidad de actomiosina y la expansión de los lúmenes en dicho proceso. Por un lado, las proteínas de polaridad planar, aunque expresadas en mayores niveles en tubos en comparación con monocapas epiteliales, no parecen modular la coalescencia de lúmenes, así como tampoco la contractilidad mediada por actomiosina parece tener un influencia sobre dicho proceso. Sin embargo, la expansión del lumen, ya sea por acumulación de fluido o por repulsión de las membranas apicales, sí tiene un papel determinante en la coalescencia de lúmenes durante la tubulogénesis *in vitro*.

Además, hemos utilizado esta herramienta de cultivo de tubos renales como una nueva plataforma para ensayos de nefrotoxicidad y validación de fármacos. En este sentido, se ha visto que algunos transportadores de fármacos específicos de túbulos proximales están más expresados en células creciendo sobre micropatrones que en cultivos de monocapas epiteliales. Este hecho hace de los tubos en micropatrones un modelo más funcional ya que el transporte de fármacos se ve favorecido en estas condiciones, y por tanto, los túbulos resultan altamente sensibles a los efectos nefrotóxicos. De acuerdo con esto, el tratamiento con dosis bajas de gentamicina, un conocido fármaco nefrotóxico, produce un aumento de la apoptosis en tubos en micropatrones pero no en monocapas epiteliales. De manera similar, debido a dicha estructura tubular, podemos observar otros defectos morfológicos en micropatrones que no podemos ver en las células creciendo en 2D.

En conjunto, hemos desarrollado un sistema de cultivo de túbulos epiteliales capaz de replicar *in vitro* los procesos morfogenéticos que ocurren *in vivo* durante la tubulogénesis. Además, podría ser de gran utilidad para la investigación farmacológica, ya que es fácil de manipular y podría ahorrar costosos e innecesarios ensayos preliminares con animales que son éticamente cuestionables.

Some epithelial tubes, such as the gastrointestinal tract and the pancreas, form through a process known as '*de novo*' lumen formation. This mechanism of tubulogenesis requires a first step of multiple lumen initiation (generating various foci) along the anteroposterior axis, which eventually expand and fuse to adjacent lumens to form a single cavity along the whole tubular structure, that later differentiates to accomplish its biological function. A system with the potential to recapitulate this mechanism *in vitro* would emerge as a very powerful device to study the molecular mechanisms involved in organ tube formation, providing a more physiological model of epithelial organs. We have developed a micropattern-based approach that allows renal epithelial cells to grow in a three-dimensional architecture and form tubes *in vitro* through a process that closely resembles *in vivo* tubulogenesis.

We are able to modify tube architecture by changing micropattern shape, which can impact lumen formation and morphology, proliferation and spindle orientation. The device also allows the modulation of extracellular matrix composition and matrix stiffness to analyse the morphological response to different environmental scenarios. Tubes cultured on laminin display different features from those grown on fibronectin. Laminin promotes the formation of tubes with more opened lumens and with a rounded shape whereas fibronectin coating favours a higher spreading and cell adhesion. Furthermore, matrix stiffness is controlling the assembly of focal adhesions as tubes grown on stiffer substrates show higher expression of focal adhesion proteins and the formation of focal adhesion clusters compared to tubes grown on softer substrates like silicone. Mechanotransduction processes are also being affected as shown by the down-modulation of YAP and lower actomyosin contractility in more compliant gels.

The mechanisms controlling lumen resolution are poorly understood and these tubular platforms provide a very potent tool to study these events. We have analysed the role of planar cell polarity, actomyosin contractility and lumen expansion in lumen coalescence. Planar cell polarity proteins, although higher expressed in tubes compared to epithelial monolayers, do not seem to modulate lumen coalescence and actomyosin-driven junctional shrinking is not controlling lumen fusion. However, a very significant role of lumen expansion, either by fluid accumulation or by membrane repulsion, in the achievement of a single lumen has been reported using this *in vitro* system.

Besides its potential use to study morphogenetic processes, growing renal tubes *in vitro* provides a new platform for drug discovery and nephrotoxicity assays. We have found that some proximal tubule drug transporters are upregulated in micropatterns compared to epithelial monolayers, making them more functional and favouring drug transport, which in turn makes them highly sensitive to nephrotoxic effects. Consistent with this, treatment with low doses of gentamicin, a known nephrotoxic drug, only induced increased apoptosis in tubes on micropatterns but not in epithelial monolayers. Similarly, because of the particular tubular shape, we are able to observe further morphological defects in micropatterns that we are not able to see in monolayers.

Altogether, we have developed an epithelial tube model system able to mimic tubulogenesis *in vitro.* Besides it can highly accelerate research as it is easy to handle and manipulate and, moreover, it presents a way to circumvent animal experimentation. This platform is very interesting since it does not involve the use of porous filter supports and the resulting tubules are well suited for high-throughput screening, high-content imaging and analysis and chemical modifications.

INDEX

GLOSSARY

2D: 2-dimensional

3D: 3-dimensional

ABCB1: ATP binding cassette subfamily B member

ABP: Actin-Binding Protein

AJs: Adherens Junctions

AMIS: Apical Membrane Initiating Site

AP: Antero-Posterior

β-cat: β-catenin

CE: Convergent extension

CIP: Contact Inhibition of Proliferation

ECIS: Electric Cell-substrate Impedance System

ECM: Extracellular Matrix

EMT: Epithelial-to-Mesenchymal Transition

FAs: Focal Adhesions

Ft/Ds: Fat/Dachsous

FBS: Fetal Bovine Serum

Fj: Four-jointed

FRAP: Fluorescence Recovery After Photobleaching

Fuz: Fuzzy protein

Fz: Frizzled

GFP: Green Fluorescent Protein

GGT1: γ-glutamyltransferase 1

hTERT: Human **Telomerase Reverse Transcriptase**

IF: Immunofluorescence

KD: Knock-down

LLC-PK1: Lewis-Lung Cancer Porcine Kidney 1

LRP2: Low density lipoprotein-related protein 2

MG: Matrigel

MDCK: Madin-Darby Canine Kidney II

MDR1: Multi-Drug Resistance Protein 1

μCP: Micro-Contact Printing

OCT2: Organic Cation Transporter 2

p-MRLC: Phospho-Myosin Regulatory Light Chain

PA: PolyAcrilamide

PIP2: Phosphatidylinositol(4,5)-bisphosphate

PIP3: Phosphatidylinositol(3,4,5)-trisphosphate

PCP: Planar Cell Polarity

PDMS: PolyDimethylSiloxane

Podxl: Podocalyxin

qPCR: Quantitative real-time PCR

RPTEC/TERT1: Renal Proximal Tubule Epithelial Cells/ Telomerase Reverse Transcriptase1

SHH: Sonic Hedgehog

siRNA: small interfering RNA molecules

TAJs: Tricellular Adherens Junctions

TER: Trans-epithelial resistance

TJs: Tight Junctions

TGN: trans-Golgi network

YAP1: Yes-Associated Protein1

ZO-1: Zonula Occludens 1

INTRODUCTION

I. EPITHELIAL MORPHOGENESIS

Simple epithelial tissues cover most internal surfaces of the organism with epithelial cells being the fundamental building blocks of many organs. Epithelial organs accomplish a plethora of different functions: from digestion in the intestine to excretion through the kidneys; from lactation in the mammary glands to breathing through the lungs (Figure I1). The wide array of epithelial functions relies on the diversity of developmental strategies, environmental patterns and cellular variability occurring during morphogenesis**.** These complex and distinct events have been a fundamental theme of research during the last century highlighting how important for our society is to understand the origins of life from its very beginning.

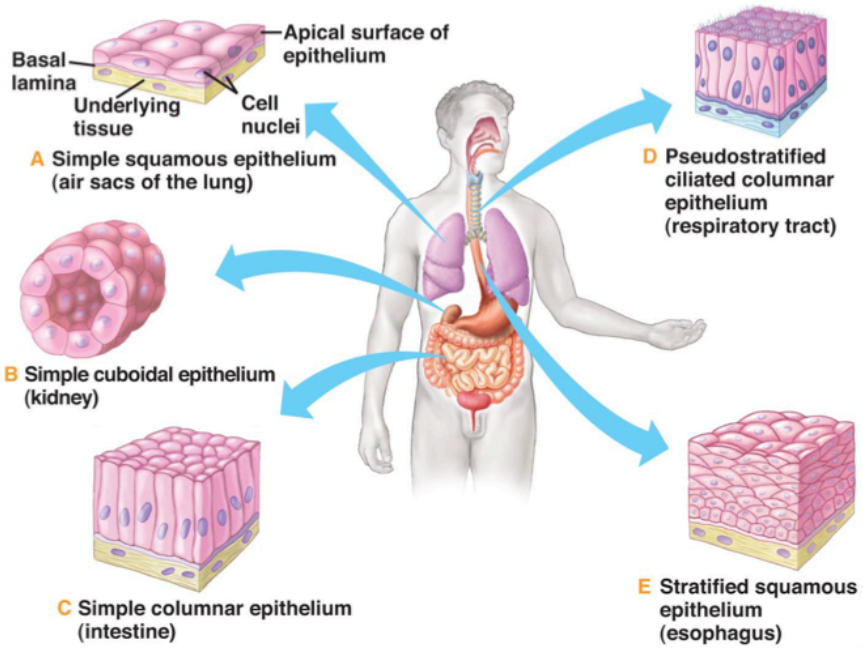

Figure I1: Variability in epithelial tissues. Depending on the organ, epithelial tissues show a wide diversity in configuration and function that arises from the many different morphogenetic processes occurring during development.

Epithelial morphogenesis embraces all the many different processes contributing to organ formation and the establishment of a determined body shape, comprising those effective molecular mechanisms driving cell shape changes, cell migration, cell division, and cell differentiation. The generation of a multicellular organism relies on the precise integration and coordination of all these morphogenetic events to achieve the appropriate biological outcome. To understand epithelial morphogenesis, it is paramount to further depict the mechanisms that drive the cellular rearrangement of epithelial tissues[1]. At first, cell fates are stated by a group of transcription factors, which specify the diverse cell groups determined to undergo those cellular changes [2]. At the same time, extracellular signals trigger specific morphogenetic events within a whole epithelial sheet or a particular subgroup of cells [3]. These responding cells execute a morphogenetic program, which requires the precise coordination of the cytoskeleton and adhesive properties to drive cell rearrangements and specific movements [4, 5].

Particularly, by reorganising the cytoskeleton cell shape changes, which causes a remodelling of epithelial shape as a whole, but does not involve changes in cell position within an epithelial sheet [6]. However, changes in cell position relative to other cells in an epithelium are achieved if the cytoskeletal reorganisation is accompanied by a breakdown and rebuilding of the cell-cell [7]. These cell rearrangements (such as intercalation, ingression, egression or fusion of epithelia) yield different outcomes and are paramount top produce long-range morphogenetic changes. Additional cytoskeletal-driven mechanisms are responsible for migratory behaviours of cells. Cell migration during morphogenesis is coupled to focal adhesions (FAs) because a dynamic interaction with the extracellular matrix (ECM) is required both to achieve single-cell migration or collective cell migration during a series of morphogenetic processes [8]. Finally, patterns of cell proliferation and cell death contribute to epithelial morphogenesis and the spatial and temporal regulation of these processes in some cases plays an important role in shaping tissues division [9-11].

Over the last decades, cell biology has successfully characterised the function of proteins or protein complexes in individual cells but rarely provided information on the relative physiological relevance of these observations for a particular morphogenetic process. Although developmental biology has been successful in establishing the epistatic relationship of transcription factors and signal transduction molecules required for cell fate determination and initiation of morphogenesis, much less is known about the function of the actual effectors of morphogenesis and its crosstalk with the coexisting morphogenetic processes. However, although we are far from a coherent picture of even a simple morphogenetic process that fully integrates the information from the steps mentioned above, more recent studies tend to delve into the whole picture of morphogenesis by analysing cell changes at the tissue-scale [12]. These studies have provided an abundance of new information on the role and regulation of the cytoskeleton, cell-cell adhesion, and cell-matrix adhesion in developmental and regeneration processes.

I.I Tubulogenesis in epithelial organs

Most of our internal organs are made of polarised epithelial cells forming tubes, which organise as an intricate network mostly in charge of transporting and distributing metabolites throughout the body [13]. The fine orchestration of the described morphogenetic processes is paramount for the coordination and synchronisation of the cells that would form these tubular structures. Interestingly, the variability of tubular organs derives from the broad diversity of different strategies to create epithelial tubes during development [14]. This variability generates a remarkable structural and cellular diversity: different tube sizes, shapes and connecting patterns [14-16]. Despite this diversity, the mechanisms of tube formation can be classified into two distinct groups depending on the initial polarisation state of the cells [13, 17] (Figure I2). A polarised epithelial sheet of cells can form a tube

through actomyosin-mediated apical constriction by two different processes: wrapping and budding. In the case of wrapping, the polarised epithelial sheet bends to enclose a hollowed cavity while during budding, the formation of the tubes relies on an invagination process. The neural tube of vertebrates forms through wrapping [18] and budding is required for angiogenic sprouting and the formation of the *Drosophila* tracheal system[19, 20]. Alternatively, tubes can also arise from an unpolarised cord of cells that acquire polarity in response to external cues during development. Mainly, two different processes for tube formation from unpolarised cells have been described: cavitation and 'cord hollowing'. During cavitation, the inner group of cells in a mass undergo apoptotic processes generating clearance of the lumen. Cavitation occurs at the mammary gland terminal end buds [21], and the zebrafish intestine and mammalian dorsal aorta are formed by 'cord hollowing' [22-24].

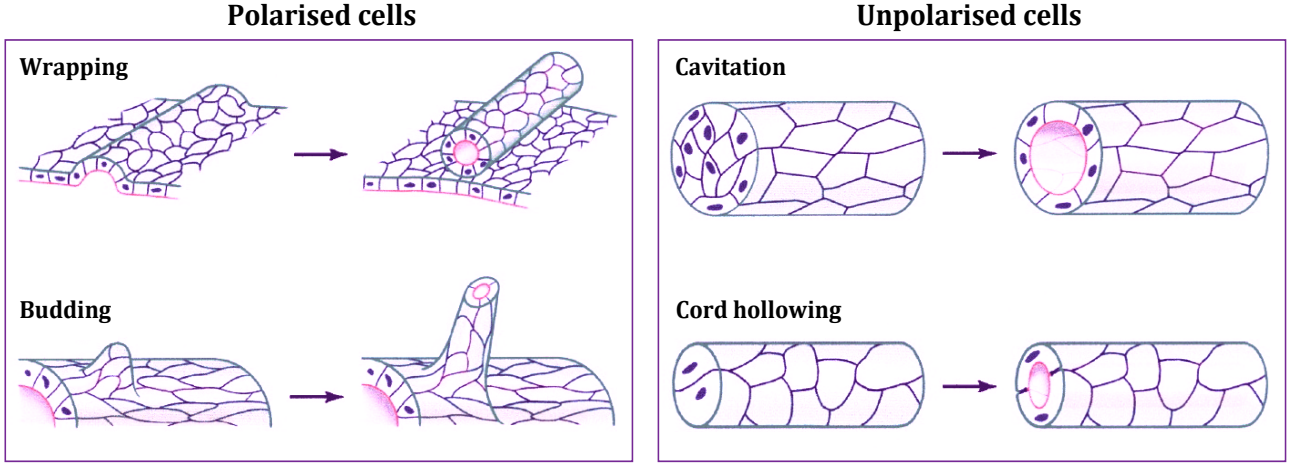

Figure I2: Epithelial tube formation. Epithelial tubes arise from either polarised or unpolarised cells and form using different mechanisms that give rise a well-defined structure consisting on a monolayer of epithelial cells with a single interconnected extracellular space, the lumen, which communicates with the external environment

While many different processes of tube formation exist, we are particularly interested in the 'cord hollowing' process of tubulogenesis, which has been the main model in this study (Figure I3). This process consists of a first step of polarity acquisition and *de novo* lumen formation that is triggered by extracellular polarisation cues that orient the apicobasal axis. Polarised vectorial membrane trafficking organise together with the cytoskeleton to form a new apical membrane known as Apical Membrane Initiating Site (AMIS). Then, the lumen is enlarged by different processes: electrostatic membrane repulsion, fluid secretion into the luminal space through paracellular ion transport, apical actomyosin contractility and oriented cell division [14, 25]. Once lumens reach a critical size and they are close enough, there is a lumen resolution stage that requires both junction shrinking mediated by actomyosin contractility and lumen fusion. During this lumen coalescence process, the multiple small lumens that have arisen throughout the whole growing tube coalesce into a single continuous lumen in an anterior to posterior manner. Then, tubes grow through convergent extension (CE) movements, and cells differentiate to create a mature organ. Tube morphogenesis is a very intricate process and

although many studies have been done on this topic, the precise mechanism mediating lumen resolution at a molecular level has not been completely elucidated yet. However, recent literature is providing very interesting insights into this process showing that lumen resolution seems to be mediated by Sonic Hedgehog (SHH) signalling in the zebrafish model, as smoothened mutants are unable to undergo the crucial process of lumen fusion and thus fail to form a single continuous lumen in the gut [26]. Besides, its crosstalk with the underlying smooth muscle is essential for gut formation as well [27].

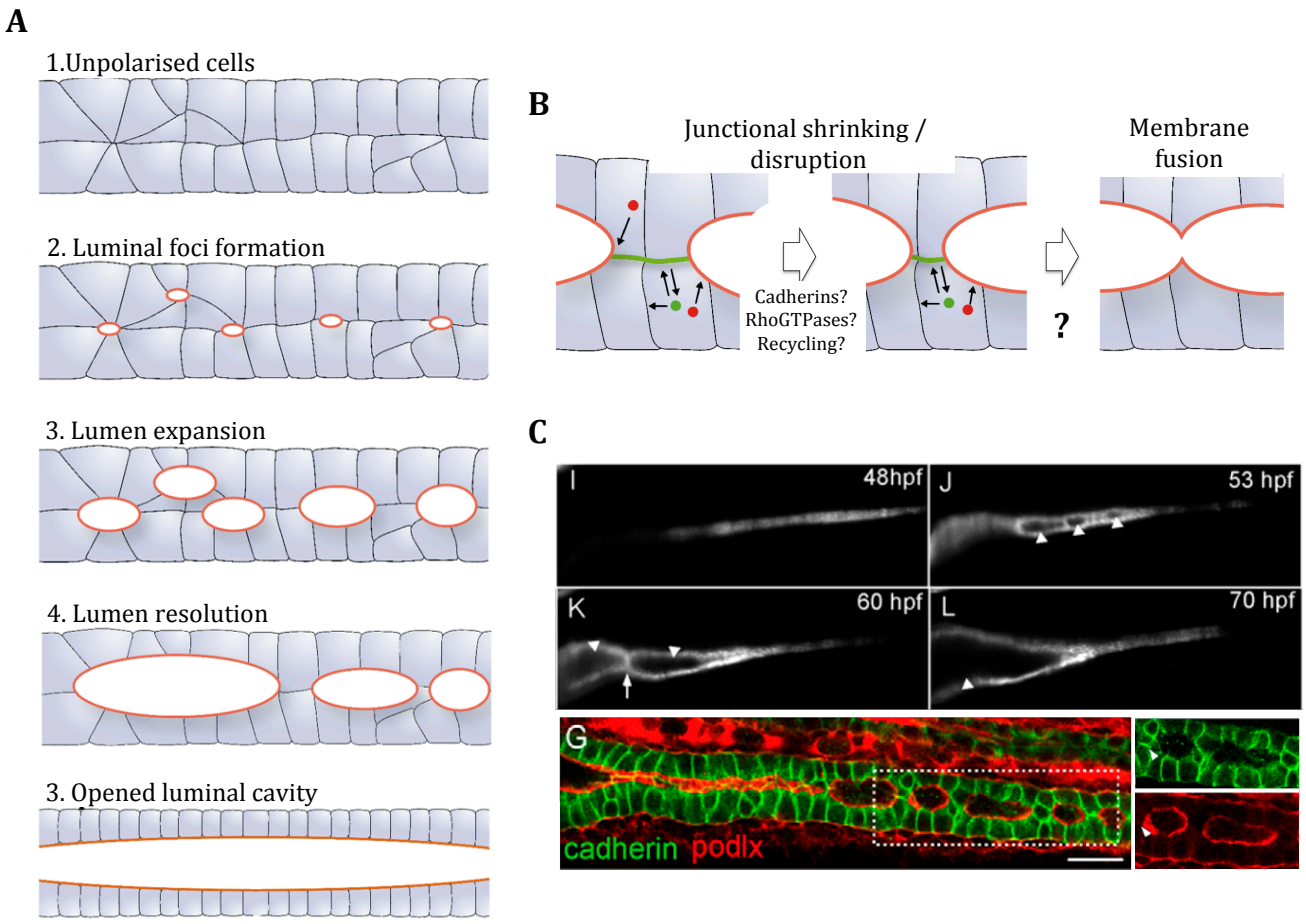

Figure I3: Cord hollowing process of tubulogenesis. (A) The formation of the intestine in vertebrates begins when a solid rod of endodermal cells differentiate into epithelial cells and undergo a cord hollowing process to form a tube. (B) Junction remodelling during tube formation requires junctional shrinking and membrane fusion. (C) Tube formation in zebrafish gut occurs through 'cord hollowing' (Image is taken from Alvers et al. 2014 [26]).

The establishment and control of a correct tubular architecture are fundamental, not only for the understanding of the development of organs but also because many diseases are often related with the loss of any of these epithelial characteristics. For instance, in some cancers cells undergo an epithelial-to-mesenchymal transition (EMT) that causes loss of cell adhesion and polarity markers, which results in the activation of migratory phenotypes [28]. This loss of epithelial integrity is associated with tumour progression and poor prognosis [29] also leading to invasion and metastasis [30]. Besides cancer, defects in epithelial morphogenesis during development also leads to other diseases like

polycystic kidney disease, atherosclerotic heart disease or faciogenital dysplasia among others. Therefore, to understand how an epithelium can self-organise and create a tube at a molecular level, developing new tools and strategies for diagnosis and treatment are paramount.

I.II Epithelial cell polarity

Most epithelial cells present two different types of polarisation. The most extensively studied is apicobasal polarity. Additionally, epithelial cells can also polarise within the plane of the epithelium, what is known as planar cell polarity (PCP). Apicobasal polarity and PCP are interconnected because core PCP proteins are localised at or near the position of adherens junctions and can bind or be bound by apicobasal determinants [31-34]. Both types of epithelial polarisation have key roles in developmental processes, regeneration and homeostasis. Loss of polarity through deregulation of the polarity program is critical for cancer cell invasion and tumour progression [35-37].

I.I.I Apico-basal polarity

Most of the epithelial organs, such as gut, kidney or mammary gland, consist of a layer of polarised epithelial cells enclosing a central cavity. These epithelial cells have two different membrane domains that vary in morphology and composition: an apical domain, lining the central lumen, and a basolateral domain, in contact with adjacent cells and the ECM [38]. The segregation of these membrane domains relies on the acquisition of apicobasal polarity, a process that implies polarised vesicle trafficking, adhesion complex formation, and cytoskeletal rearrangements [39]. The role of a whole genetic program at the onset of the epithelialisation process has been extensively studied.

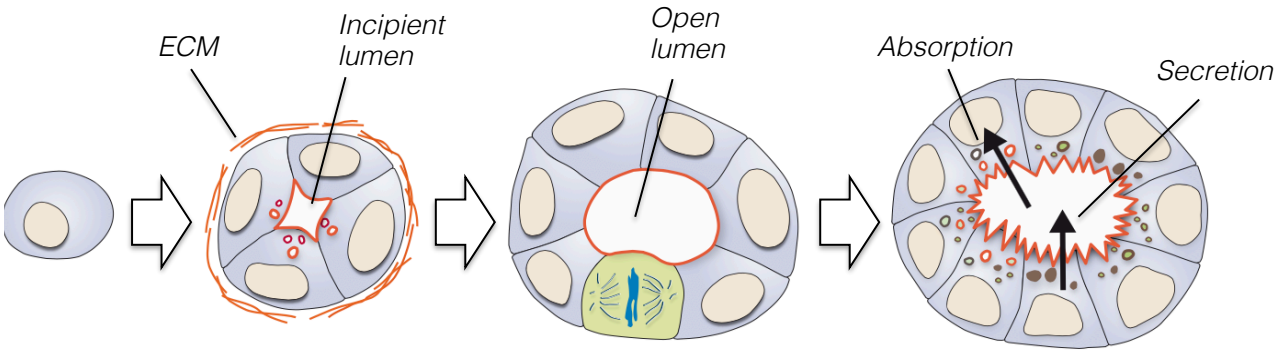

Figure I4: Steps in polarity acquisition during zebrafish gut formation. Apicobasal polarity initiates with the development of multiple actin-rich foci between cells in response to extracellular cues and is followed by the localisation of junctional proteins at multiple points within the intestine. Membrane identity requires the coordination between polarised vectorial trafficking and the junctional complexes. Lumens expand and grow by cell division and through paracellular ion transport. Cells within a tube ultimately differentiate to provide functionality to the developing gut.

Epithelial polarity complexes

One central question in the history of the study of epithelia has been to understand how this polarity is achieved and maintained by the epithelial layers. This question has been largely addressed, and the extensive literature postulates the existence of three different polarity complexes that determine the

different cell domains, and that show a close relationship [40]. Cell asymmetry is achieved through the coordination of these three central polarity complexes that are very well conserved among the different metazoans, indicating that the acquisition of polarity is a robust and critical process in development (Figure I5). These three complexes have antagonistic interactions and spatiotemporally regulate epithelial polarisation through their interactions with the cytoskeleton and adhesion proteins. The Par/aPKC complex, consisting in Par3, Par6 and atypical protein kinase C (aPKC) is a master regulator of polarity [41] and also maintains the integrity of the apical domain through interaction with Cdc42, recruiting components of the Crumbs and Scribble complexes. The Crumbs complex is apically located, and it controls the extension of the apical domain and restricts the Scribble complex to the basolateral domain [42]. The Scribble complex inhibits the formation of tight junctions in the basolateral domain, suppresses apical membrane identity by inhibiting Par3 and controls the basolateral expansion [43].

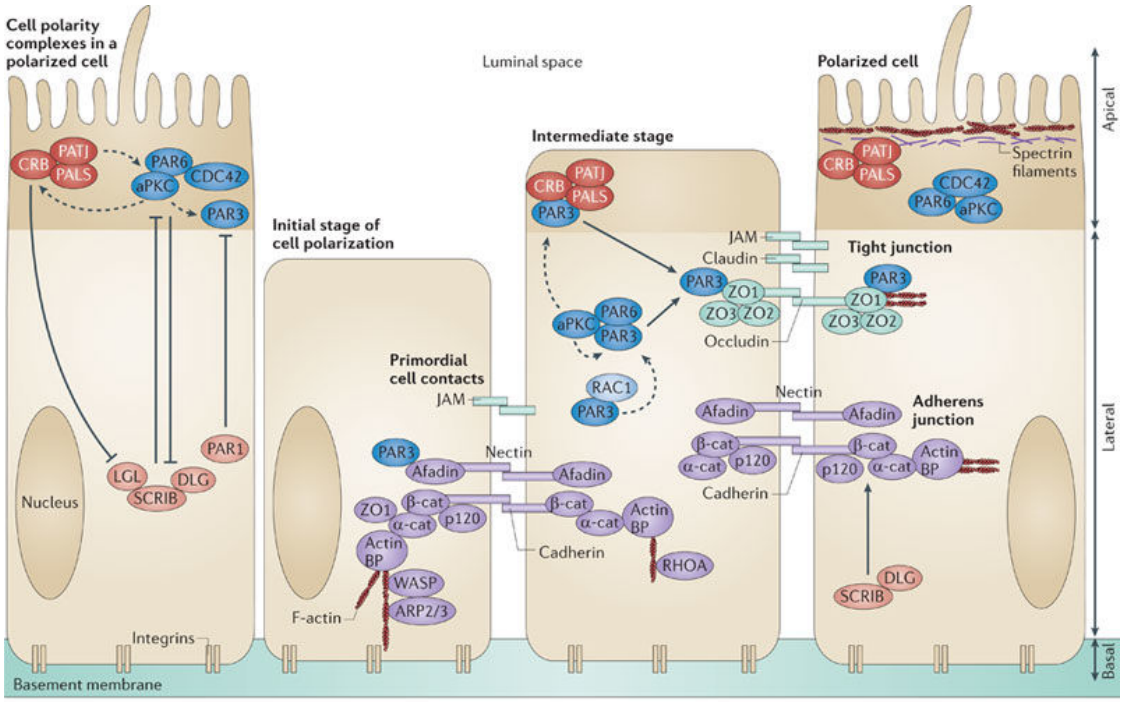

Figure I5. Polarity complexes Three major polarity complexes participate in the establishment of apical-basal polarity: the Crumbs complex (shown in red), the Par/aPKC complex (shown in blue) and the Scribble complex (shown in orange) At early stages of cell polarisation, PAR3 binds to afadin, and these primordial adhesions mature to form the belt-like adhesion junctions and tight junctions that localise at the apical-basal membrane border. This involves aPKC activity and the exclusion of PAR3 from primordial adhesions at intermediate stages of polarisation. This is followed by PAR3 exclusion from both the PAR/aPKC and Crumbs complexes to establish the apical-lateral border and the apical membrane; whereas, the SCRIB complex defines the basolateral membrane domain by antagonising the Par/aPKC and Crumbs complexes, which restricts their activity and the expansion of the apical domain. (Adapted from Martín-Belmonte, F. & Pérez-Moreno,M; 2011 [29])

Role of ECM composition

To coordinate tissue development cells must sense their environment, which includes their position in relation to the surrounding cells through adherens junctions (AJs), and the orientation axis by direct interaction of FAs with components of the ECM [44]. The initial cue for the establishment of the

polarity axis comes from the basal lamina, which is a functional part of the basement membrane, composed of a fibrous mesh of glycoproteins and proteoglycans such as laminins, fibronectin, collagen IV, perlecan and entactins [45]. The binding of ECM proteins to integrins and other transmembrane receptors promotes a variety of cellular responses including survival, proliferation, adhesion, and migration [46, 47]. Furthermore, the ECM is dynamically remodelled during development and disease states, as cells steadily degrade and resynthesize new ECM to promote remarkable changes in the microenvironment [48]. The correct deposition and assembly of this matrix is crucial for the orientation of polarity in the *Drosophila* egg chamber [49], and for the correct morphogenesis of the gut, trachea and nervous system [50]. The interaction of the basal lamina with the epithelial cells is mediated by β1-integrin and seems to be critical for the correct orientation of cell polarity and lumen formation in 3D-the Madin-Darby Canine Kidney II (MDCK) cell line [51] and *in vivo* [52, 53]. Rac1 is activated by the interaction between β1-integrin and collagen I, which induces secretion and assembly of laminin that in turn activates Rac1, which generates a positive feedback loop that reinforces this orientation signalling pathway. This mechanism also seems to relay in the orientation of the microtubule cytoskeleton since ILK-integrin (integrin-linked kinases plus β1-integrins) complexes anchor microtubule plus ends to the basolateral cell surface through the plus-end protein EB-1 [51]. Moreover, other findings have demonstrated a role for RhoA, ROCKI, myosin II, PI3K and protein kinase B in this polarity pathway [54], which also suggests an important role for the actin cytoskeleton.

Role of phosphoinositides

The aforementioned polarity defining cues induce the segregation of membrane phosphoinositide types, which are implicated in specifying membrane identity [55]. Diverse phosphoinositides are enriched in specific subcellular compartments, concentrated at the cytosolic surface of cellular membranes. In MDCK cells Phosphatidylinositol (3,4,5)-trisphosphate (PIP3) determines the basolateral membrane, whereas Phosphatidylinositol (4,5)-bisphosphate (PIP2) is required for apical membrane identity [57-60]. Phosphoinositides can recruit and activate Rho GTPases to the cell cortex [61], what is contributing to the generation of membrane identity. It has been proposed that the signalling mediated by the balance of PIP2 and PIP3 at the plasma membrane controls many important cellular processes such as growth, polarity, migration and proliferation [56], all of them being regulated by the enzymes PTEN and PI3K.

Role of vectorial trafficking

Epithelial cells have to ensure proper delivery of apical and basolateral cargoes to their respective target locations to maintain cell polarity. Polarised protein trafficking is regulated by sorting signals

contained within the proteins themselves, which are recognised by the specific sorting machinery [57-59]. The different trafficking routes and sorting mechanisms in epithelial cells include biosynthetic, endocytic, recycling and transcytotic pathways. The biosynthetic route provides newly synthesised proteins to the apical and basolateral membranes. After the synthesis of the proteins, they are transported along the secretory pathway: endoplasmic reticulum, Golgi and trans-Golgi network (TGN) and sorted into carriers to different membrane domains at either the TGN or the endosomes. Once at the plasma membrane, proteins can also be endocytosed and delivered to the early endosomes where they follow the endocytic route for degradation in the lysosomes [60, 61]. Proteins in the plasma membrane can also follow the recycling route by passing through recycling endosomes, which can sort them back to the original cell surface [62, 63]. These proteins can also be transported across the cell to the opposite plasma membrane through the transcytotic pathway [64, 65]. The importance of these pathways varies with the type of epithelial cell, but they must be finely regulated in order to induce and maintain apicobasal cell polarity.

Role of spindle orientation

Epithelial cells divide stereotypically with the plane of division always aligned perpendicular to the apicobasal axis. The midbody, an intercellular structure derived from central spindle microtubules, is asymmetrically localised near the apical surface during cytokinesis. Interestingly, the midbody colocalises with apical determinants such as Par3, aPKC and Crumbs3a and trafficking of Crumbs3a in Rab11 vesicles to the midbody is necessary for early lumen formation [66, 67]. Besides, the midbody does also control ciliogensis through the extracellular pathway in MDCK cells, indicating that the position of the midbody highly influences cell polarity features [68]. Since the orientation of the spindle determines the position of the midbody in mitosis and therefore the lumen initiation site and the formation of primary cilia, spindle misorientation may induce multiple dysfunctional lumens arising from multiple mislocalised midbodies in the epithelial structure as shown recently [66]. Thus, the control of the positioning of the mitotic spindle and the midbody requires a tightly regulated mechanism to ensure the maintenance of epithelial integrity after cell divison.

Spindle orientation is regulated through astral microtubule capture at the plasma membrane by a protein complex formed by the small G-protein Gαi, Pins (LGN) and NuMA [69]. Originally discovered in *Drosophila*, the mechanism was characterised in the regulation of asymmetric cell division during neuroblast differentiation [70-73]. When these cells divide, the mitotic spindle is initially formed with an apicobasal orientation, and rapidly rotates 90 degrees aligning itself parallel to the epithelial monolayer. Pins localisation to the lateral membrane enables astral microtubule anchoring in this region and prevents the spindle from realigning with the apicobasal axis [74-76]. Disruption or mislocalisation of Pins inhibits normal lumen formation and causes spindle misorientation. Pins

segregation appears to be regulated by aPKC-mediated phosphorylation at the apical membrane, which causes Pins sequestering in the cytoplasm [77]. Disruption of any of the components of the Par6/aPKC complex causes multiple lumen formation, abnormal spindle orientation, and loss of polarised localisation of Pins [78, 79]. Moreover, we have found that EGF-IQGAP1 regulates the spindle orientation, probably by the initial attachment of the microtubules to the EGF receptor through IQGAP1 [80].

Opening the lumen

As the creation of a novel apical membrane through vectorial trafficking is usually slower than the cell division, apical vesicles often fuse at the cell-cell junctions of daughter cells forming two layers of apical membranes that are very close one to the other. In this scenario, the secretion of proteins that helps to prevent membranes from sticking plays a prominent role. Proteins like glycoproteins and polysaccharides induce membrane detachment by steric hindrance of cell-cell adhesion. The sialomucin Podocalyxin (Podxl) is secreted by podocytes and it is necessary for the opening of intercellular urinary spaces and for lumen formation in the 3D-MDCK system, *Drosophila* tracheal tubes and blood vessels [20, 81-83]. Moreover, actomyosin contraction at the cell cortex of the apical membrane is also necessary to provide driving forces for lumen expansion. This process of contraction at the apical cortex drives morphogenesis in *Drosophila* [84], although actomyosin relaxation has shown to be required for luminal expansion, like in the zebrafish hindbrain [85]. This shows how the fine control of RhoGTPases and actomyosin contractility is modelling apical membrane formation [86]. Importantly, the apical actomyosin belt also connects with vectorial trafficking, since the apical actin belt orientates the centrosome to the apical pole [87], which is organising the microtubule cytoskeleton and therefore the traffic of vesicles.

Besides membrane repulsion and apical contractility, filling of the cavity with liquid is also contributing to lumen expansion (Figure I4). This fluid accumulation is mainly mediated by paracellular transport of ions through the tight junctions [88]. The TJs proteins Claudins form selective pores that allow the interchange of different ions, thereby controlling the permeability of epithelial junctions. Claudins are transcriptionally regulated during morphogenesis in different organs, like Claudin-2 in the kidney or Claudin5a in the brain ventricular lumen [89]. In zebrafish, Claudin-15a controls lumen coalescence in the gut and the claudin-15-like b regulates intrahepatic biliary duct morphogenesis [22, 90]. Other components such ion pumps are necessary, like the cystic fibrosis transmembrane conductance regulator (CFTR) channel, which increases the luminal concentration of chloride ions [91, 92]. The Na^+K^+-ATPases have revealed to be important for defining basolateral identity in *Drosophila* and for lumen coalescence in zebrafish [93, 94].

I.I.II Planar cell polarity in tube formation

PCP is perpendicular to the apicobasal axis and refers to the alignment of cell polarity across the tissue plane. PCP is evident in many features in epithelia of multicellular organisms such as primary cilia positioning [95-97], orientation of sensory hair cells of the vertebrate inner ear [98-100], and in the orientation of hair in the fur of mammals [101]. The most thoroughly studied tissues in the context of PCP have been the fly eyes, wings, abdomen, and notum. The molecular pathways and mechanisms involved in the establishment and control of PCP have been mostly characterised in the invertebrate organism *Drosophila*, in which the main PCP controlling modules have been described, giving rise to a model that is still not completely understood [102]. Genetic disruptions in the PCP signalling pathway cause severe developmental abnormalities in vertebrates, notably neural tube defects, left/right patterning defects, and ciliopathies, which highlight the essential requirement for PCP during development [96, 103-108].

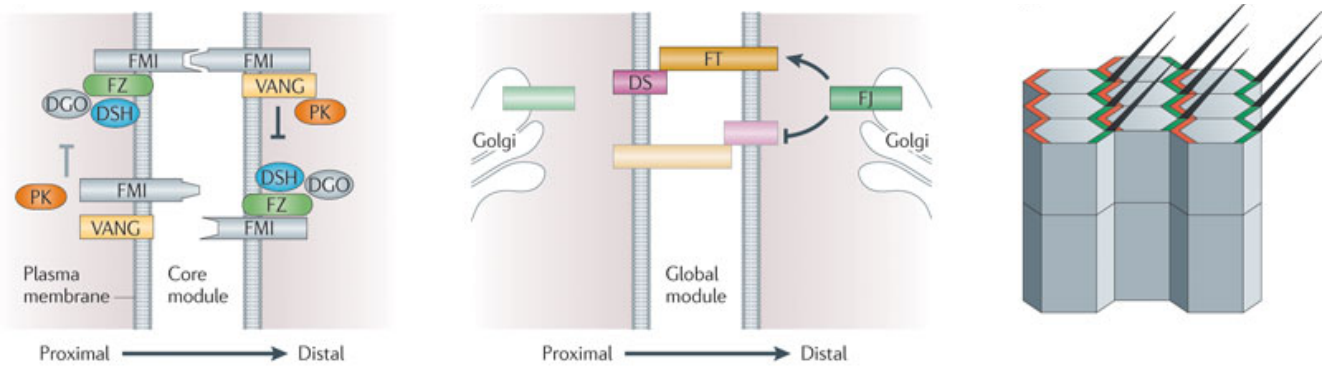

Figure I6: The PCP signalling mechanism is consits of three functional modules: a core module, a global directional cue and many tissue-specific effector modules that respond to the upstream modules to produce morphological asymmetry in individual tissues. (Adapted from Bayly and Axelrod, 2011 [109])

Key to the establishment of PCP is asymmetric partitioning of cortical PCP components and intercellular communication to coordinate polarity between neighbouring cells. It has been proposed that the PCP signalling mechanism consists of two major groups of proteins: the 'core PCP module' and the 'Fat/Dachsous' (Ft/Ds) system (also called global module) [110] (Figure I5). These proteins adopt a polarised subcellular distribution, accumulating in proximal and distal subsets on opposite sides of cell-cell junctions. The core PCP proteins are required to establish molecular asymmetry within and between cells, and encode transmembrane proteins as well as cytoplasmic components that associate with the membrane during PCP signalling (Figure I5, left pannel). In *Drosophila*, the transmembrane receptor Frizzed (Fz) and the cytoplasmic proteins Dishevelled and Diego are localised to distal cell junctions while the transmembrane protein Vang and the cytoplasmic protein Prickle lay proximally [111-115]. Besides, the atypical cadherin Flamingo is localised both proximally and distally forming homodimers between neighbouring cells [116]. The Fat/Dachsous (Ft/Ds) pathway, also known as the global module, includes the large protocadherins Fat (Ft) and Dachsous (Ds) and the Golgi resident

transmembrane kinase, Four-jointed (Fj) [117, 118] (Figure I5, middle pannel). Ds and its ligand Ft accumulate on opposite cell edges, where they form intercellular heterophilic interactions [119, 120]. Similar to the core system, Ft/Ds also displays molecular asymmetries in *Drosophila*. Unlike the core components, Ds and Fj are expressed in complementary gradients in the *Drosophila* eye and developing wing, which contribute to the cellular asymmetries of Ds and Ft. Both modules work together to integrate tissue-scale signalling into single-cell responses. Whether Ft/Ds/Fj gradients and asymmetries are conserved in vertebrate systems has yet to be determined.

The functions of gradients and mechanical forces as global cues that bias PCP orientation are beginning to be elucidated. Because Frizzled receptor can serve as a receptor for Wnt signalling molecules, and Wnt molecules are diffusible morphogens, capable of generating a gradient across the tissue, it has been hypothesised that members of the Wnt family may be directional cues for PCP signalling. To date, no Wnt has emerged from any study in *Drosophila* as a candidate for filling this role [121]. However, while Wnts appear to be dispensable for PCP signalling in *Drosophila*, Wnt molecules have been implicated in PCP regulation in the vertebrates. In zebrafish, Wnt5a and Wnt11 are required for CE movements during gastrulation, but uniform expression of Wnt11 rescues the mutant phenotype, which suggests that it is permissive rather than instructive [122, 123]. Wnt5a is expressed in a gradient along the axis of polarity in the mouse inner ear, where it interacts genetically with Vangl2 in cochlear hair cell orientation [124]. In the mouse limb, Wnt5a and its atypical receptor Ror2 are required for limb elongation and the asymmetric localisation of Vangl2 at the proximal face of converging and extending chondrocytes [125]. Wnt5a is expressed in a distal-to-proximal gradient, which induces a gradient of Vangl2 phosphorylation. The functional consequences of Vangl2 phosphorylation are unknown but Vangl2 cellular asymmetry appears to be strongest distally, where Wnt5a and Vangl2 phosphorylation levels are highest [125]. Although the evidence for Wnt gradients as global PCP cues is accumulating, the mechanisms by which they regulate core protein levels or activity remain to be elucidated. Wnts are clearly important regulators of PCP, but whether they act instructively or permissively remains unclear.

Convergent extension

Wnt/PCP signalling is an essential player in the processes that control CE and cell migration during gastrulation. CE was the first vertebrate process to be linked molecularly to PCP [126]. During CE, mesenchymal cells elongate, form mediolateral-directed protrusions, and intercalate mediolaterally, narrowing this axis while simultaneously lengthening the anterior–posterior (AP) axis (Figure I7) [127, 128]. Mediolateral polarisation, elongation, and intercalation are lost when core PCP components are disrupted, leading to a failure in CE [126, 129-131]. While several PCP-dependent mechanisms have been proposed to mediate CE movements, two recent studies provide direct mechanistic links between asymmetrically localized core PCP components and CE behaviours. In

neuroepithelial cells, PCP specifies the localisation of myosin to the AP faces of intercalating cells. Flamingo/Celsr1 and Dishevelled recruit the formin DAAM1 to the AP junction, which in turn binds and activates PDZ-RhoGEF. This likely activates RhoA and myosin contractility specifically at AP junctions, resulting in medial-directed cell intercalation and neural plate bending [132]. A similar mechanism was found to drive CE movements of mesenchymal cells during *Xenopus* gastrulation. In this case, Fz and Dishevelled help to localise septins to mediolateral vertices, where they spatially restrict cortical actomyosin contractility and junctional shrinking to AP cell edges, thus driving cell intercalation [108, 133]. These results indicate that Rho GTPase activity is required to establish a planar polarised actomyosin network, and that actin-binding proteins enhances myosin contractility locally to generate robust mechanical forces during axis elongation.

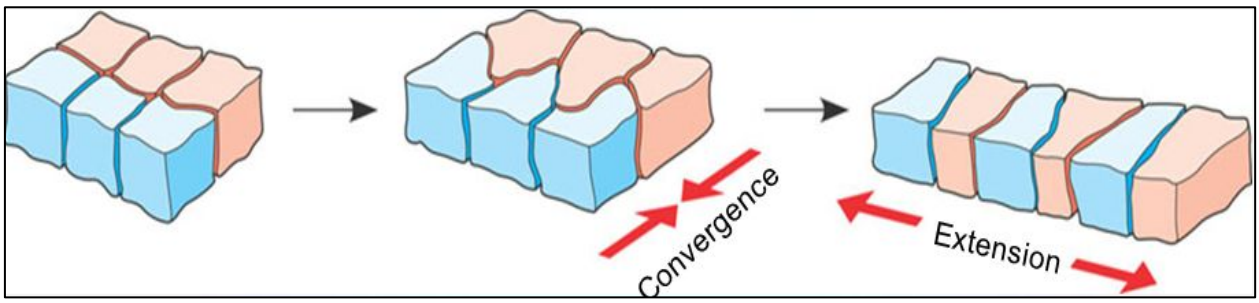

Figure I7: Convergent extension movements contribute to tissue elongation by expanding in one axis and shortening in the perpendicular axis through mediolateral intercalation and actomyosin-dependent junction remodelling.

Recent progress has been made towards understanding how protein transport, endocytosis, and intercellular interactions contribute to asymmetric PCP protein localisation in vertebrates. Together, these findings on the field of PCP regulation are shedding light on how global cues integrate with local cell interactions to organize cellular polarity at the tissue level. More importantly, these studies show how asymmetric PCP localisation produces collectively polarised cell behaviours through spatial modulation of the cytoskeleton, which can impact on tissue remodelling and growth.

II. Environmental regulation of Morphogenesis

Epithelial morphogenesis in multicellular organisms is tightly regulated by the formation of cell-cell junctions and cell-matrix adhesion. The cell-cell junctional complexes are along the lateral membrane that connects neighbouring cells and they delineate the apicobasal axis. Regarding cell-matrix adhesion, integrin sensing and clustering in response to specific ECM components has shown to be crucial to coordinate apicobasal polarisation among other morphogenetic processes [38]. Besides its role in directing cell polarity, many studies over the few last decades have led to major breakthroughs in our understanding of adhesion-dependent mechanotransduction pathways as critical regulators of epithelial morphogenesis. Among the many protein modules involved in sensing physical constraints

(Figure I8), FAs and AJs are responsible for detecting external forces exerted at the ECM level [134] and by neighboring cells [135] respectively, triggering cellular responses that are inherently linked to the reorganisation of the cytoskeleton and the initiation of complex signalling cascades [136]. At the same time, cell ability to sense and react to mechanical cues is not only essential to coordinate morphogenesis but also to maintain homeostasis. Importantly, disruption of epithelial cell architecture results in the appearance of diverse pathologies including fibrosis and cancer [28].

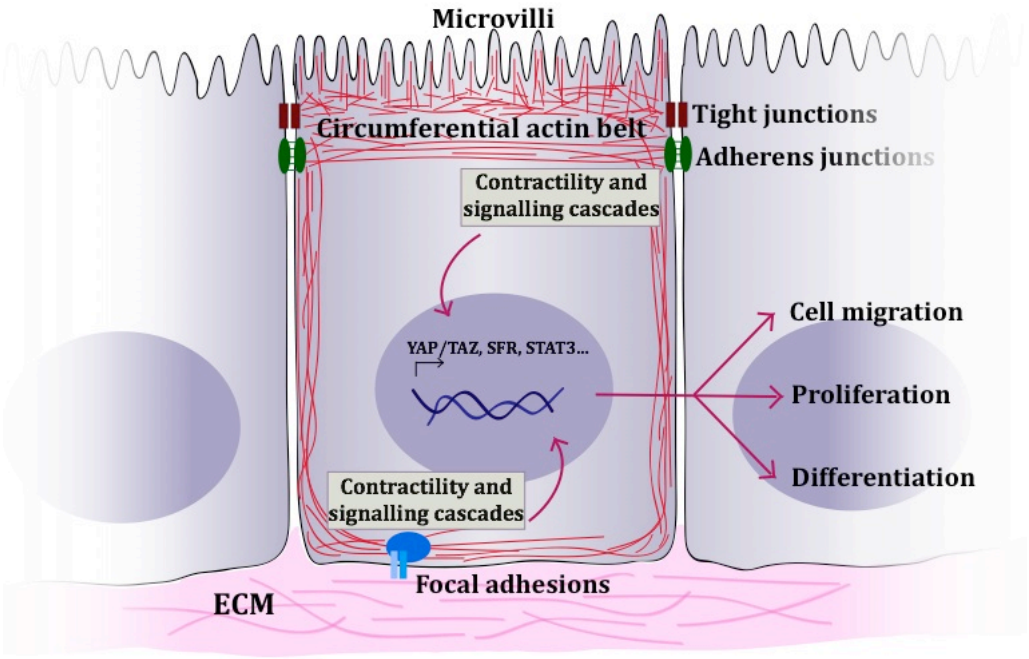

Figure I8. Cell-adhesion modules in mechanotransduction. Besides providing an anchor to the extracellular space, AJs and FAs can translate environmental forces into a bunch of cellular responses. Upon force sensing, these complexes can trigger cytoskeletal rearrangements through direct association with the actin network and activate diverse signalling cascades in response to forces. Consequently, downstream transcription factors translocate to the nucleus and promote the transcription of many genes. Mainly, FA complexes can sense matrix stiffness and regulate cell migration and intracellular forces in response to environmental strains. At the same time, cell confinement and intercellular tension are sensed by AJs, which have a central role in regulating tissue growth and polarity acquisition in epithelial cells.

II.II.I Focal adhesion complexes and matrix sensing in epithelial cell behaviour

Although many distinct types of adhesion complexes exist connecting the cell cortex to the ECM, the best characterised among them are FAs (Figure I9) [137]. FAs are bulky protein complexes anchored both to the ECM, through integrins, and to the actomyosin cytoskeleton through a complex set of linkages, providing a direct interaction of the ECM with the actomyosin cytoskeleton [138]. FAs, by coupling the actin cables to the ECM can transmit small amounts of mechanical loads in a bi-directional fashion [134]. Indeed, FAs enable epithelial cells to sense physical and topographical constraints and, consequently, they respond by remodeling the ECM and counterbalancing their own contractility [139]. These cytoskeletal rearrangements are also coupled to signalling networks such as YAP/TAZ, MAPK–ERK pathway and FAK/Src signalling cascade [140]. Many different proteins shape the FA complex, and the interplay between them is still under study. The assembly of FAs has conventionally

been associated to different small GTPases like Rho, Rac and R-Ras [141], but the assembly of FAs is also force-dependent and they tend to form mechanotransduction clutches [142]. FA proteins transcription levels and assembly are also regulated by YAP as shown recently [143].

These adhesion complexes are tightly regulated as the position, dynamics and interactions of the FA components modify its function and sensing [144-146]. In particular, the FA protein Talin, which directly binds integrins, plays a prominent role in FA mechanosensing by changing conformation in response to tension, exposing a cryptic domain and leading to increased recruitment of Vinculin, an actin-binding protein (ABP) whose levels at FAs correlate with the amount of local tension [147]. Moreover, Talin is cleaved by calpain and has a role in FA dissolution and cell cycle progression [148]. Recent findings demonstrate that Talin cleavage is also force-dependent [149].

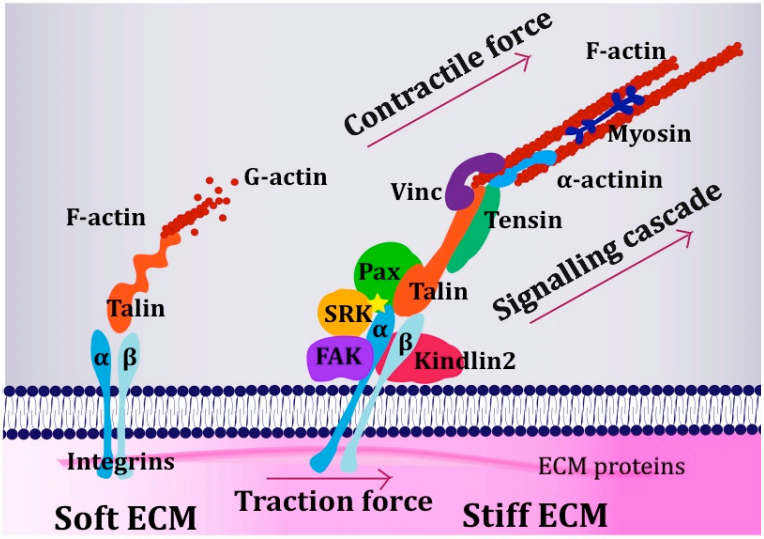

Figure I9. FA complexes can sense matrix stiffness. Integrin clusters form after activation by talin binding, providing a scaffold for initial actin polymerisation (left). Further FA proteins begin to tether, and a mature and functional FA complex is assembled (right). External and internal forces stabilise the FA complex through cycles of transient talin stretching and vinculin binding until the talin-actin bond is wholly established. Stiff substrates and myosin contraction trigger talin folding and unfolding. This promotes further integrin clustering, actin polymerisation, actomyosin contraction and activation of signalling pathways

As sensors of physical cues, FAs play an essential role in sensing matrix stiffness: in response to extracellular tension, the associated downstream signalling pathways can modulate a wide range of biological processes including cell cycle [150], and the circadian clock [151]. Variations in cell migration are a very well studied effect of FA sensing of matrix stiffness. Indeed, cells primed on a stiff matrix migrate faster, display faster actomyosin dynamics, form more massive focal adhesions, and exhibit YAP localisation in the nucleus than those spread on more compliant substrates [140]. When cells are primed in anisotropic matrices, they migrate from compliant to stiffer substrates in a very well characterised process named durotaxis [152]. But more importantly, matrix stiffness highly influences polarity acquisition. To analyse the role of mechanical matrix properties in epithelial differentiation initial studies attempted to use different ECM mimics of varying stiffness. In such experiments, increasing matrix rigidity was shown to block cell polarity and lumen formation, and to promote EMT and a cancer-like invasive behavior [153-155].

II.II.II Adherens junctions as force sensors in morphogenesis and homeostasis

Many studies have sustained the idea that geometrical and mechanical constraints provided by neighboring cells act as cues to coordinate actin and membrane dynamics and modulate several mechanotransduction pathways. AJs are the main sensors of these physical constraints, having a critical role in a plethora of morphogenetic processes [7], but also in maintaining barrier integrity in response to tension [156]. AJs are cell-cell adhesion complexes containing, among others, cadherin proteins that form homophilic interactions at intercellular junctions. The cytoplasmic domain of cadherins interacts with β-catenin (β-cat), which in turn is bound to actin filaments via α-catenin and other scaffolding and nucleating proteins (Figure I10). FAs and AJs function as cell anchors sharing many striking similarities in architecture, composition, and role. In fact, they both serve as hubs of cytoskeletal assembly and organisation, gathering many biochemical signalling networks. Interestingly, a mechanism of protein conformational changes in response to tension, analogous to that described for FAs, has been established for tension sensing at the AJs, α-catenin has been pointed as the paradigmatic protein able to change its conformation in response to stretch, in turn promoting Vinculin binding [157]

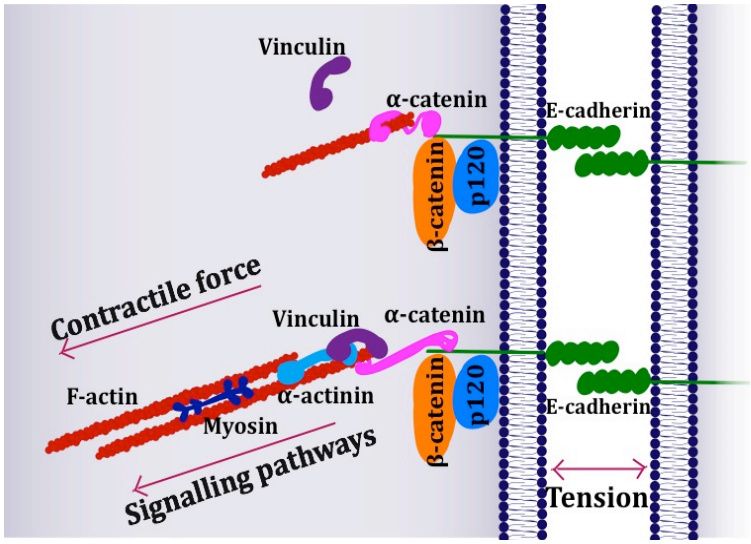

Figure I10. Adherens junctions can sense intercellular tension. E-cadherin is a transmembrane protein whose extracellular region (composed of five Ca2+-binding domains), form homophilic interactions with those on the neighboring cells. At the same time, E-cadherin associates with catenins, which are bound to the actin cytoskeleton forming stable AJs (top). External forces can induce α-catenin unfolding and vinculin binding (bottom). These mechanical events foster a cellular response through cytoskeletal remodeling and activation of many signalling pathways. The elongation of actin cables occurs through the activation of ABP, and the contraction of AJ-linked actomyosin networks is mediated by signalling downstream of RhoGTPases

E-cadherin is the most prominent AJs protein in epithelial cells [12]. In addition to its function in maintaining epithelial barrier integrity, some studies have also revealed that E-cadherin plays a role in sensing rigidity at cells boundaries [158] and coordinating formation and regulation of AJs under the control of this force. Additionally, tension at the level of AJs dependent on cell density has long been related to the regulation of cell proliferation. AJs sense cell confinement as cell density increases and the subsequent reorganisation of the cytoskeleton can either promote or terminate the progression of cell cycle. In this direction, recent studies have shown that compression of an epithelial monolayer rapidly leads to cell cycle arrest whereas stretching results in fast cell cycle reactivation [159]. Interestingly, some components of the Hippo pathway and the transcription of specific genes seem to

regulate cell division in response to E-cadherin-catenin control of intercellular surface tension [160]. At low cell density, YAP localises to the nucleus and elicits re-entry to the cell cycle, while β-cat promotes cell cycle progression. In highly dense cell culture, YAP is phosphorylated and sequestered in the cytoplasm, inducing quiescence through a process that requires coupling between E-cadherin extracellular domains [161]. Further studies have shown that E-cadherin cleavage by MT2-MMP metalloproteinase at apical junctions favors exit from quiescence, promoting proliferation and cell extrusion through tampering apical junctions [162]. Indeed, evidence indicates that loss of AJs and epithelial barrier integrity are also playing a role in cell extrusion [163], although the molecular mechanisms underlying cell extrusion have been traditionally associated either with activation of apoptotic pathways [164] or signalling through stretched-activated channel Piezo1 [10]. It has been suggested that the reformation of AJs underneath a dying cell is also mediating cell extrusion [165], showing that maintenance of adhesive forces during apoptotic cell turnover is essential to maintain tissue integrity. Recent studies have begun to resolve the long-standing debate about the link between tension sensing through AJs and cell extrusion by connecting YAP activity to cell extrusion [166, 167]. One of these studies demonstrated that epithelial monolayers behave like nematic fluids and topological defects are transduced into cell extrusion processes through a mechanism that implies YAP inactivation, and Caspase3 activation interestingly, tampering with the AJs increases both the number of topological defects and the extrusion rate [167].

Beyond regulating the tug-of-war between cell proliferation and death, AJs also mediate cell polarity in response to intercellular tension. By using micropatterns to restrict cell spreading, it was found that there is a remarkable link between physical restriction of adhesion and the positioning and stability of AJs [168]. The same technique was used to demonstrate that acquisition of polarity also relies on cell confinement, as low contractility promotes, cell polarisation, organelle positioning and lumen formation [87, 169]. Remodelling of actomyosin flows at the level of AJs may play a crucial role in these processes through its plausible modulation of the contractility state. In line with these observations, recent work has revealed a novel pathway for primary cilium assembly that requires the translocation of the midbody remnant from peripheral to central positions, where the centrosome is situated, through a process that is dependent on cell confinement [68]. Further studies have revealed a role for tricellular junctions (TAJs), a site of hot spots of epithelial tension where at least three cells meet [170], as polarity cues promoting mitotic spindle orientation in *Drosophila.* TAJs can localise and align force generators depending on anisotropic strain during interphase to assemble astral microtubules at specific sites [171]. Interestingly, perturbation of actomyosin activity at TAJs results in a loss of contractile force patterning in the epithelium and mispositioning of the apical domain [172]. Taking together, these findings suggest a model in which regulation of intracellular tension in response to intercellular forces by AJs provides physical landmarks to orient and direct cell polarity.

III. MODELLING EPITHELIAL MORPHOGENESIS

Due to the different patterns that epithelial organs follow to form tubules, many models have been used, including *in vitro* and *in vivo* models. Overall, these models have provided different insights in lumen and tube formation.

III.I *In vivo* systems

The most studied *in vivo* model systems for tubulogenesis include the *Drosophila* trachea and salivary gland, the zebrafish gut and vasculature. Because of its powerful genetics, the *Drosophila* trachea and salivary gland are widely studied model systems for branched and unbranched tubes, respectively. Both organs begin as polarised epithelial placodes, which through coordinated cell shape changes, cell rearrangements, and cell migration form elongated tubes [19]. In addition to shared machineries with vertebrate epithelial morphogenesis, certain mechanisms appear to be specific of *Drosophila* development. In particular, in the morphogenesis of the *Drosophila* trachea, the control of cell invagination, migration, competition, and rearrangement is accompanied by the sequential secretion and resorption of chitinal matrix proteins into and from the apical luminal space, a vital step in the elaboration of the trachea's complex tubular networks [173]. Although great advances have been made in *Drosophila*, the study of tube morphogenesis using vertebrates represents a closer approach to understanding human development and disease. For instance, genetic analysis using the zebrafish model has led to identification of mutations in molecules that are required for gut morphogenesis [174]. In the zebrafish gut, lumen formation occurs by *de novo* apical polarisation, and its individual steps have been recently characterised (Figure I3) [22, 26, 175, 176] Thus, studies of morphogenesis in zebrafish could be critical for elucidating the molecular basis of uncharacterised congenital gut defects and potentially provide novel insight into intestinal oncogenic processes [177, 178].

III.II *In vitro* systems

Many different cell models have been used to analyse the molecular and cellular events required to organise individual cells into 3D epithelial organs. Several *in vitro* systems consisting on cultured epithelial cell lines grown on a layer of (or embedded in) ECM have been developed (figure I11). The MDCK epithelial cell system is perhaps the best and most widely used *in vitro* model to investigate cell polarity during epithelial morphogenesis [14, 25, 179]. MDCK cells, which have properties of the kidney distal tubule and collecting duct, have been used for decades as a 2-dimensionl (2D) model to study epithelial polarity and protein trafficking. However, since the culture porous filter support provides an overriding extrinsic cue to orient cell polarity, they represent a less appropriate model to analyse morphogenesis. By contrast, MDCK cells embedded in ECM form cysts, spherical monolayers enclosing a central fluid-filled lumen [180], which has proven to be a very informative model system

(Figures I4, I10). Indeed, MDCK cells cultured in laminin-rich ECM extracts, such as Matrigel (MG), rapidly form clonal polarised structures with an enclosed lumen between two cells after just 24h. From then on, thecysts continue to grow by cell division and lumen expansion (Figure I10). This rapid polarised growth allows fast genetic analysis of lumen formation mechanisms, perhaps the main advantage of this system.

Nowadays, many laboratories are beginning to develop a promising cell culture system, denominated organoids. These structures are formed in culture systems of isolated stem cells or of a combination of stem cells with animal explants or cell lines that together create an organ-like structure *in vitro*. Organoids that share many similarities with the organ they derive from. Organoids derived from kidney [181], guts [182] mammary glands [183] or optic cups [184] have recently arisen, constituting a powerful tool for the study of differentiation and morphogenesis *in vitro.*

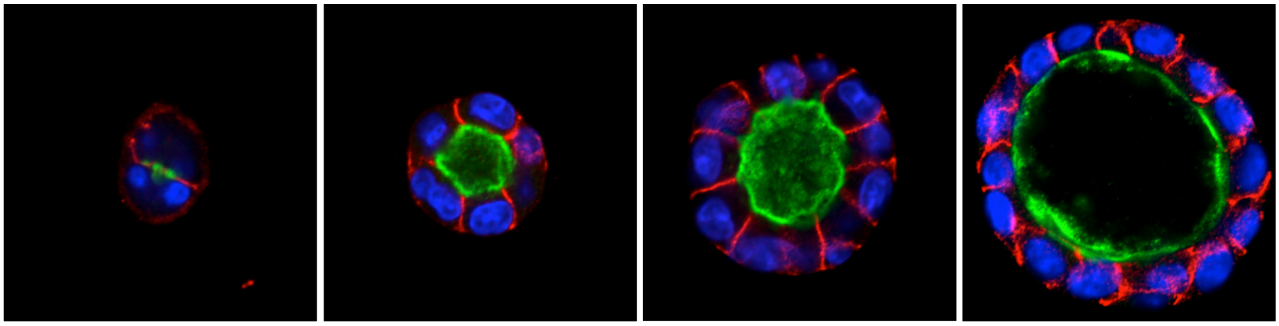

Figure I11. MDCK cyst formation. In the 3D-MDCK model cells are cultured in extracellular matrix, like collagen or matrigel, in which the cells grow in suspension and spontaneously form spherical structures containing a hollowed cavity or lumen. Cyst formation starts with the assembly of the AMIS by active trafficking of apical components. Fluid efflux into the initiating lumen and cell division promotes cyst growth. MDCK cells growing on a cyst are polarised in the apicobasal axis and thus, the apical membrane is functional.

Although studies using MDCK cysts and organoids have helped to gain insights into the complexity of morphogenesis, such conventional *in vitro* systems cannot fully recapitulate the complexity of lumen formation in in physiological condition, such as epithelial transformation and remodelling, which are necessary for the formation and resolution of tubular structures. Recently, new techniques of organotypic cell culture have been developed based on micropatterns and other microarchitecture-based models [87, 185]. These micropatterns have brought the possibility of interacting mechanistically with the cells, which provided new insights in the biomechanics of lumen formation and of pathogenic scenarios [186, 187].

IV. MICROPATTERNING TECHNOLOGY

The control of the cellular microenvironment allows understanding of the different cellular mechanisms that underlie cell-cell and cell-matrix interactions. In conventional 2D cultures, cells are randomly seeded and lack of a specific organisation as they are maintained on flat and homogeneous

substrates. Major drawbacks of these adherent cultures are the difficulty to control environmental parameters and the impossibility to recapitulate multicellular architectures, tissue-tissue interfaces and the physicochemical microenvironment found *in vivo*. On the contrary, organs and tissues are characterised by interacting cells organised in a 3D configuration. The absence of a physiologically relevant cell conformation strongly impacts on cell function and behaviour. However, micropatterning technology has emerged as a novel platform for cell culture allowing the mechanical interaction with the cells, which importantly provides new insights in the biomechanics of lumen formation, among others [87]. Micropatterning is the art of miniaturisation of patterns and it has become a standard in biomaterials engineering and for fundamental research on cellular biology. Micropatterns can be used to control the geometry of cell adhesion and substrate rigidity. This tool has helped to gain insights into how the extracellular environment influences processes such as the orientation of the cell division, organelle positioning, cytoskeleton rearrangement, cell differentiation and directionality of cell migration among others.

IV.I Basis of microfabrication

The fabrication of micropatterns is based on the treatment of specific substrates to create adhesive surfaces in order to obtain a better control over spatial cell organisation. The use of patterns of adhesive proteins at micrometer scale, offers the possibility of better controlling cell environment and thus the biological response to extracellular constraints. Although the first micropatterning methods for manipulating cell adhesion patterns have been developed more than 50 years ago [188], they have been commercially available and recently became an essential tool in cell biology laboratories. There are many different ways to create micropatterns. Among the numerous micropatterning techniques microcontact printing (μCP) has become the most popular and it is widely used. A polydimethylsiloxane (PDMS) stamp with the desired micro-features is used to print ECM proteins onto the culture substrate. It requires an initial etching step to microfabricate the stamp. Complementary, non-etching, methods have been developed on the basis of direct photo-patterning. Photosensitisers and fluorophores have also been used to produce reactive oxygen species upon light excitation, which induce protein grafting on polyethylene glycol surfaces [189]. UV light can also be used to excite any photosensitive chemical groups and to detach the protein-repellent part of a molecule that has been grafted on the substrate to allow further binding of ligands [190, 191]. Alternatively, high-energy light, such as deep UV light below 200nm [192] or concentrated light from pulsed lasers [193], have also proved useful to create local plasma and directly oxidise culture substrates. Exposure to plasma converts hydrophobic polystyrene culture substrates into hydrophilic [194] and also destroys the protein and cell repellent properties of polyethylene glycol, thus allowing for further protein grafting.

IV.II Main applications

The development of micropatterned platforms revealed important insights into how the geometry and chemical composition of the microenvironment impacts on cellular physiology, from intracellular organisation to multicellular morphogenesis.

VI.II.I Cell shape and polarity

Micropatterns allow the control of cell shape. Indeed, when cells adhere to micropatterns, they adopt the pattern shape, emulating its geometry. For example, on L-shaped patterns, cells attach to the adhesive micropattern spreading along the bars, and adopt a triangle shape. When cells are seeded on 'U'-shaped patterns, they cell adopts a squared form [195]. Differences in nuclear orientation and deformation can also be observed in response to physical constraints. Indeed, in high confinement conditions, the nucleus adopts an oriented ellipsoidal shape [196, 197]. Cell confinement can also regulate the actomyosin cytoskeletal contractility and impact polarity processes that depend on a controlled regulation of intercellular tension, showing that the ECM geometry determines the orientation of cell polarity axes [169]. For example, it was found that ECM and extracellular physical tension regulate the positioning and stability of AJs [168]. Besides, cell confinement also is regulating ciliogenesis [68, 198] and lumen formation [87].

VI.II.II Cell migration

Cell motility is also highly influence by patterns shape. Cell migration on thin micropatterned tracks allow directed cell movement, better mimicking cell migration *in vivo* compared to cell migration on homogeneous and not-confined surfaces. Cells plated on wide tracks of fibronectin migrate in a similar manner as cells grown on Petri dishes, with their centrosome and Golgi apparatus oriented towards the leading edge of the cell. By contrast, in cells confined to thin tracks, the centrosome is located behind their nucleus [199]. The width of the pattern is also influencing the migratory velocity as cells on narrow substrates migrate faster than those grown on a homogeneous substrate surface and display similar characteristics to those of cells migrating *in vivo* such as a coordinated displacement of cell front and cell body, and dependency on actomyosin contractility and microtubules [199, 200]. Strikingly, nuclear motility can also be regulated by attachment constraints, as nuclei can perform an auto-reverse motion when a migrating nucleus approaches the leading edge of an elongated cell [201]. Interestingly, during oriented cell migration on tracks, the Src signalling pathway, is activated homogeneously throughout in the cell, whereas Rac activation, which promotes lamellipodia formation, only occurs at the leading edge [187].

IV.II.III Cell division

The axis of division, which determines the position of the daughter cells, has been extensively studied using micropatterns. Spindle orientation is controlled by cortical cues and the cell microenvironment geometry. The combination of adhesive micropatterns with laser ablation to remove specific retraction fibers allowed the analysis of the role of physical parameters of the microenvironment in controlling the cell division axis [202]. Indeed, localised deprivation or accumulation of cell adhesion sites can change the local density of cortical cues, affecting the force balance on the spindle pole and switch the spindle from a symmetric to an asymmetric orientation [203].

IV.II.IV Cell differentiation

Micropatterning tools can be useful to allow the reconstitution of tissue-like conditions for *in vitro*. The role of cell shape and cell contractility in modulating cell reprogramming and stem cell fate has been shown using micropatterns. For instance, keratinocyte terminal differentiation is dependent on cell shape rather than ECM composition or concentration [204]. Moreover, human mesenchymal stem cells on a micropatterned island can differentiate into adipocytes or osteoblasts depending on the size of the island, which influences cytoskeletal contractility and the activation of the RhoA signalling pathway [205].

V. *IN VITRO* TESTING OF DRUG NEPHROTOXICITY

The astonishing cost of bringing a drug to the market is often coupled to the extremely high failure rate of potential drugs during early (and often late) stages of clinical trials owing to unexpected human nephrotoxicity [206]. Drug–induced nephrotoxicity remains especially difficult to predict in both preclinical and clinical stages and is often undetected until patient hospitalisation. This is due to numerous factors including the lack of well-established testing methods capable of accurately predicting clinical usefulness and drug toxicity during pre-clinical development. Thus, it is crucial to achieve more relevant biological models to better predict the nephrotoxic effects of developing drug.

In this direction, bioengineered tissues would present a more reliable model to assess drug nephrotoxicity in early pre-clinical stages prior to animal experimentation and clinical trials. This improvement, would allow for better prediction of the nephrotoxic effects of new drugs.

V.I Nephrotoxicity

Many medications are a common source of acute kidney injury and nephrotoxic drugs cause approximately 20% of episodes of acute renal failure [207]. Drug-induced nephrotoxicity tends to be

more common among certain patients and in specific clinical situations. As the world population has aged over the last decades, nowadays patients have a higher incidence of diabetes and cardiovascular disease, take multiple medications, and are exposed to more diagnostic and therapeutic procedures with the potential to harm kidney function [208]. Although renal impairment is often reversible if the harmful drug is discontinued, the disease can be costly and may require multiple interventions, including hospitalisation.

Drugs shown to cause nephrotoxicity exert their toxic effects by one or more common pathogenic mechanisms [209]. Renal tubular cells, and in particular proximal tubule cells, are vulnerable to the toxic effects of drugs because they play a prominent role in concentrating and reabsorbing the glomerular filtrate. This renal function exposes them to high levels of circulating toxins. Drugs causing tubular cell toxicity usually do so by impairing mitochondrial function, interfering with tubular transport, increasing oxidative stress, forming free radicals or eliciting an inflammatory response [210]. Drugs associated with these pathogenic mechanisms of injury include aminoglycosides, NSAIDs, antiretrovirals, cisplatin and contrast dyes among others [211-213].

V.II Biological models to study nephrotoxicity

Most widespread *in vitro* systems to test nephrotoxicity are renal biopsies [214] or 2D cultures of proximal tubule cell lines [215, 216]. The correlation and efficiency to *in vivo* conditions obtained with these systems are not satisfactory enough as, on the one side, animal biopsies and freshly isolated preparations are unstable and can only be used for a short period of time. These assays are also very laborious and low efficiency is obtained. On the other side, the configuration of *in vitro* cell-based assays is not natural for mammalian cells and, therefore, it is not physiologically relevant [217]. Moreover, cell monolayers present additional limitations when screening applications are performed such as a disordered distribution within the plane and heterogeneous phenotypes of cellular morphologies and organisation. Furthermore, renal cell lines cultured under 2D conditions show absence of some renal cell-specific transport processes and suffer biotransformations. Some new 2D assays have been proposed in order to overcome the above-mentioned drawbacks and important insights on cytoskeleton organisation have been observed. However, these assays still present one serious limitation: cells show a very spread phenotype in contrast to what is observed *in vivo*, where cells present a 3D architecture deconstructing [218]. These artifacts associated with the culture method may trigger non-physiological features such as enhanced stress fibers and lack of cell polarity [87].

Conversely, 3D cell culture assays provide multiple advantages when compared to 2D environments [219, 220]. They are physiologically more relevant and may predict nephrotoxic effects more

accurately. However, cells embedded in hydrogels show 3D-like structures but their morphologies differ from one cell to another, which complicates screening applications [221].

V.III Micropatterns as a tool to test nephrotoxicity

As mentioned above, current pre-clinical methods for determining renal toxicity include 2D cell cultures and animal models, both of which are unable of fully recapitulating the *in vivo* human response to drugs, contributing to the high failure rate of clinical trials, where high budgets are spent each year. Thus, it is necessary to develop a novel system to assay nephrotoxicity capable of providing stability and reproducibility in order to test realistic drug doses and permit the chronic administration to monitor toxicity due to repeat dosing. This may reveal cumulative tissue injury with repeated administration of subtoxic concentrations, a situation more relevant to the clinical practice. This new model should resemble *in vivo* human renal structures and express renal-specific drug transporters. More importantly, it should allow high throughput screening and facilitate multiple biochemical analysis *in situ.*

In this direction, a micropattern-based model combined with the ECM-gels to achieve 3D structures would pose a more physiological model to study the toxic effect of new compounds in the renal system [87, 222]. This device would allow recapitulation of cell microenvironment *in vitro* by providing restriction of the size and shape of the cell adhesion site, presenting similar geometrical and mechanical constraints to those of the microenvironment. Moreover, cell position, shape, polarity and internal organisation could then become normalised. Besides, the use of micropatterns has shown to be useful for the culture of diverse cell lines. Thus, different cell lines could be cultured through this method upon defining the most suitable for nephrotoxicity assays. Finally, the repetition of the same microfeature on a unique culture platform, as well as the adaptability of micropatterns to 96-well plate formats, allows the performance of high-content and high-throughput screenings as cell evolutions can be observed in parallel. Therefore, developing a patentable micropattern system would present a way to perform nephrotoxicity testing in a more reliable *in vitro* model than the ones currently used.

OBJECTIVES

The present project aims to exploit the micropatterning technology to create superior physiologically relevant kidney models that are easy to use and resemble the architecture and functionality of tubes *in vivo.* With this device we aim to:

1. Adapt and optimise the technology to recapitulate tubulogenesis in different epithelial cell lines.

2. Investigate the role of extracellular constraints in the morphogenetic processes underlying epithelial tube formation.

3. Explore the cellular and molecular events driving lumen coalescence in renal epithelial tubes.

4. Characterise and validate the micropatterned devices as high-throughput platforms for nephrotoxicity testing.

MATERIAL & METHODS

1. Microcontact printing

For the fabrication of micropatterns using µCP, a quartz photomask was designed using Mathlab software. This photomask was used to photolithograph a silicon wafer using SU-8 negative photoresist. Both the photomask and the silicone wafer were fabricated at the Molecular Biology Institute (Singapore). The photomasks were silanised with Trichloro(1H,1H,2H,2H-perfluorooctyl)silane (Sigma-Aldrich) for 1h in a vacuum dissecator. To produce the stamps, the PDMS Sylgard184 (Dow Corning) was used. Elastomer and crosslinker components were thoroughly mixed in a 1:10 (crosslinker:elastomer) ratio and kept under vacuum for 20-30min to degas the mixture. The silicone was then poured over the wafer and baked at 80ºC for 1-2h. The polymerised silicone was peeled-off and cut into squared small pieces containing the patterned regions. These stamps were incubated with either 50µg/ml fibronectin (Millipore) or 20µg/ml laminin (Sigma-Aldrich) solutions for 1hour at room temperature to adsorb them on the PDMS surface. Stamps were rinsed 2 times with PBS and a last wash with milliQ water was done. Stamps were then dried and kept at 4ºC for a maximum of 24h. To produce the cell culture surface, we used either PDMS-coated coverslips or IBIDI chambers. 18mm borosilicate coverslips were cleaned by sonication on isopropanol. Once dried, they were coated with 50µl of 1:10 PDMS (Stiff PDMS) or 300µl of 1:20 PDMS (soft PDMS) using a spin coater. Stiff PDMS coverslips were cured at 80ºC for 1h while soft PDMS coverslips were kept for 5 days at room temperature until they are completely polymerised. Both PDMS coverslips and IBIDI chamber were activated using an UV/ozone cleaner for 15min. Alternatively; oxygen plasma could also be used. Immediately after activation, the ECM-coated stamps were µCPrinted by placing the stamps on the activated surface with the patterned side in direct contact with it in order to transfer ECM proteins from the stamp into the surface. Contact was ensured by applying gentle pressure. The stamps were carefully removed and discarded and the surface was treated with 2% Pluronics12 solution at room temperature for 40min-1h or overnight at 4ºC. The patterned surface was thoroughly rinsed with PBS to prevent cell toxicity. Patterned surfaces can be stored in PBS for 2-3days at 4ºC.

2. Fabrication of 3D micropatterns

To build 3D micropatterns, a replica of the silicon wafer was fabricated by pouring 1:10 PDMS on the silicon wafer and baking them at 80ºC for 2h. This PDMS countermould was silanised with Trichloro(1H,1H,2H,2H-perfluorooctyl)silane (Sigma-Aldrich) in a vacuum chamber and used as a negative mould to fabricate 3D micropattern surfaces. These were done by pouring 1:10 PDMS on the countermold and curing at 80ºC for 2h. Cured PDMS was cut into pieces surrounding patterned areas and covered with either 50µg/ml fibronectin (FC010, Millipore) or 20µg/ml laminin (L2020, Sigma-Aldrich) solutions for 1hour at room temperature. Pieces were rinsed 2

times with PBS and a last wash with milliQ water was done. They were then dried and kept at 4ºC for a maximum of 24h. To remove the ECM proteins adsorbed to the outer surface of the wells, only keeping the proteins adsorbed in the inner walls of the patterns, 1:10 PDMS flat surfaces were done by pouring PDMS on p100 petri dishes using a spin-coater. Once cured, surfaces were activated using a UV/ozone cleaner. Proteins were desorbed by placing the 3D micropatterns on the activated surface and performing μCP as previously described. Flat surfaces were discarded and 3D micropatterns were incubated in a with 2% Pluronics-12 solution at room temperature for 40min-1h or overnight at 4ºC. The micropatterns were thoroughly rinsed with PBS to prevent cell toxicity and stored in PBS for 2-3days at 4ºC.

3. Cell culture

3.1 2D culture

MDCKII and T23-MDCK and cells were maintained in MEM supplemented with 5%Fetal Bovine Serum (FBS), 2mM L-glutamine, 100U/ml penicillin and 100mg/ml streptomycin at 37°C in a humidified atmosphere containing 5%CO_2. LLC-PK1 cells were maintained in DMEM supplemented with 10%FBS, 2mM L-glutamine, 100iU/ml penicillin and 100mg/ml streptomycin at 37°C in a humidified atmosphere containing 5%CO_2. All the above-mentioned cell lines were passaged approximately twice per week and subcultured at a 1:5 or 1:10 ratio. RPTEC/TERT1 cells were maintained in DMEM-F12 defined medium supplemented with 5μg/ml insulin, 5μg/ml transferrin, 5ng/ml selenite, 2mM L-glutamine, 100U/ml penicillin, 100μg/ml streptomycin, 10ng/ml epithelial growth factor and 36ng/ml hydrocortisone at 37°C in a humidified atmosphere containing 5%CO_2. RPTEC/TERT1 were passaged approximately once or twice per week and subcultured at a 1:2 or 1:3 ratio. MDCK cells stably expressing Podxl-GFP were made by co-transfection with the blasticidin-resistant gene (Lipofectamine 2000, Invitrogen) and selected for 15 days using medium supplemented with 0.5mg/ml blasticidin. Cells were cultured as single cell-clones and positive colonies were trypsinised individually. Micoplasma testing was regularly performed.

3.2 3D culture

To prepare MDCK, LLC-PK1 and RPTEC/TERT1 cysts in Matrigel (BD Biosciences), cells were trypsinised to a single cell suspension of $2x10^4$cells/ml in 2%Matrigel for MDCK and LLC-PK1 and in 5%Matrigel for RPTEC/TERT1 cells. The medium for RPTEC/TERT1 cells was supplemented with 2%FBS. Cells in Matrigel were plated in 8-well coverglass chambers (250μl/well) (Ibidi) covered with Matrigel (8-15μl/well). The medium was changed every 2 days and grown for 1–3

days until cysts with lumen formed for MDCK and LLC-PK1 cells and for 1-14 days for RPTEC/TERT1 cells.

3.3 Cells on CYTOO micropatterns

Custom micropattern chips were used for tube culture using proprietary technology obtained from CYTOO, Inc. Chips were coated with 20µg/ml Collagen Type I (PureCol from Nutacon), 50µg/ml fibronectin (FC010, Millipore) or 20µg/ml laminin (L2020, Sigma-Aldrich), in 2ml PBS per chip for 1h at room temperature. Then, chips were placed in a 6-well plate and rinsed with PBS avoiding them from drying. To prepare MDCK, LLC-PK1 and RPTEC/TERT1 tubes, cells were trypsinised to a single cell suspension and $6x10^4$ cells (MDCK), 10^5 cells (LLC-PK1) or $4\ x10^5$ (RPTEC/TERT1) per chip were seeded in their appropriate culture medium and incubated for 1h at room temperature and 2h at 37°C in a humidified atmosphere containing 5% CO_2. Once cells are completely attached, the culture medium is replaced with Matrigel-containing medium. MDCK medium is supplemented with 3%FBS and 3%Matrigel; LLC-PK1 medium is supplemented with 10%FBS and 1%Matrigel; and RPTEC/TERT1 medium is supplemented with 3%FBS and 3,5%Matrigel. Chips are kept at 37°C in a humidified atmosphere containing 5% CO_2. After 24h the LLC-PK1 medium is replaced with medium containing 3%Matrigel and 10%FBS. The medium was changed 2 days and grown for 1–4 days until tubes with lumen formed for MDCK and LLC-PK1 cells and for 1-14 days for RPTEC/TERT1 cells.

3.4 MDCK on microcontact-printing micropatterns

ECM-coated patterns were fabricated as described. To prepare MDCK tubes, patterned-coverslips were placed in a 6-well plate and rinsed with PBS and incubated with culture medium for 1 hour at 37°C. MDCK, cells were trypsinised to a single cell suspension and $6x10^4$ cells per coverslip were seeded in their appropriate culture medium and incubated for 1h at room temperature and 2h at 37°C in a humidified atmosphere containing 5%CO_2. Once cells are completely attached, the culture medium is replaced with 3%Matrigel-containing medium. 3%FBS. Coverslips were kept at 37°C in a humidified atmosphere containing 5%CO_2. The medium was changed every 2 days and grown for 1–4 days until tubes with lumen formed.

3.5 Cells on 3D micropatterns

ECM-coated 3D patterns were fabricated as described. To prepare MDCK tubes, patterned-stamps were attached to the bottom of a 6-well plate by sticking with a PBS drop. MDCK cells were trypsinised to a single cell suspension and 10^5 cells were resuspended in 250µl of culture medium and placed at the top of the stamp as a drop. Cells were incubated for 3-6h at 37°C in a humidified atmosphere containing 5%CO_2. As bubbles can form inside the microwells, pippeting medium

every 1-2 hours might be necessary to break the bubbles. Once cells are completely attached, the culture medium is replaced with 3%Matrigel-containing medium covering the whole well. Stamps were kept at 37°C in a humidified atmosphere containing 5%CO_2. The medium was changed every 2 days and grown for 1–4 days until tubes with lumen formed.

3.6 Isolation and 3D culture of mammary gland organoids

We purified mammary organoids from CD1 mice following the protocol previously optimised and described for FVB mice [183]. Mammary glands pairs #3, #4 (without lymph node), and #5 were harvested from virgin 8 weeks old females. They were minced and digested in collagenase buffer (DMEM/F12 medium with 2mg/ml collagenase, 2mg/ml trypsin, 5%FBS, 5µg/ml insulin, and 50µg/ml of gentamicin) for 40-60 min at 37ºC. Samples were centrifuged at 1500 rpm for 10 min. To recover additional epithelial tissue, the top fatty layer was resuspended in DMEM/F12 and centrifuged again. The epithelial pellets were resuspended in DMEM/F12 and treated with 40µl DNase-I (2U/µl) for 3min. They were then resuspended in DMEM/F12 and centrifuged at 1500rpm for 10min in order to obtain a compact red pellet. After 4 rounds of differential centrifugation (quick spin at 1500rpm) the final white pellet consisted mostly of organoids. For 3D culture, organoids were embedded in Matrigel Growth Factor Reduced (Corning) at 2organoids/µl and plated as 75µl drops in 4-well coverglass chambers (Ibidi) over a 37ºC-heating block. Matrigel drops were allowed to polymerise for 50min at 37ºC, 5%CO_2, and then overlaid with organoid medium (DMEM/F12 with 1%penicillin-streptomycin and 1%ITS). The medium was changed after 2 days and organoids were analysed after 3-6 days of culture.

3.7 Mammary gland organoids on microchannels

ECM-coated 3D patterns were fabricated as described. To prepare Organoid-derived tubes, patterned-stamps were attached to the bottom of a 6-well plate by sticking with a PBS drop. Organoid cells isolated as described above and the final white pellet was dissociated to single cells. To obtain a single cell suspension, the pellet was gently pipetted for 3min in 2ml of trypsin-EDTA 0.25%, centrifuged, and then pipetted for 3min in 2ml DispaseII (5 mg/ml) and 200µl DNaseI (1mg/ml). After resuspension in HBSS + 2% FBS, cells were passed through a 40µm cell strainer filter in order to dissociate cell clumps and centrifuged. The total amount of cells is resuspended in organoid medium. Cells divided into the final number of patterned stamps to be used taking into account that no less than $2x10^5$ cells and a maximum of 10^6 cells per stamp were used. Cells are resuspended in 250µl/stamp of culture medium and placed at the top of the stamp as a drop. Cells were incubated for 3-6h at 37°C in a humidified atmosphere containing 5%CO_2. As bubble can form inside the microwells, pippeting medium every 1-2hours might be necessary to

break the bubbles. Once cells are completely attached, the culture medium is removed and a 18mm coverslip coated with 50µl of Matrigel Reduced Growth Factor is glued to the top of the stamp. Stamps were kept at 37°C in a humidified atmosphere containing 5%CO_2 for 1-2more hours. Then the void space between the edges of the coverslip and the bottom of the well is filled with organoid medium supplemented with 5%Matrigel Reduced Growth factors. Medium is refilled every day and cells were grown for 1–9 days until tubes with lumen formed.

3.8 Osmolarity experiment

MDCK cysts were gown as specified above either in isotonic medium (MEM supplemented with 5%FBS, 2mM L-glutamine, 100U/ml penicillin, 100mg/ml streptomycin and 2% Matrigel) or in hypertonic medium, prepared by way of the isotonic medium but supplemented with NaCl. Cyst were grown for 3 days at 37ºC in a humidified atmosphere containing 5% CO_2.

3.9 Gentamicin treatment

LLC-PK1 monolayers and tubes were grown as specified above. Gentamicin sulphate was purchased from Sigma (ref. G1914) and dissolved in water. After 3 days of growth, the culture medium of treated cells cell was supplemented with either 0.1mM or 0.5mM of gentamicin stock solution (50mg/ml). Cells were grown for 4 days at 37ºC in a humidified atmosphere containing 5% CO_2.

4. Transcriptomic analysis

For Real time quantitative PCR (qPCR) assay MDCK and LLC-PK1 cells were grown either as epithelial monolayers in M12 dishes (150000cells/well), 3D cysts in Matrigel growing in p60 dishes (500000 cells/well) and on micropatterns using 3-5 micropatterns per condition. Total RNA was isolated at 72h and purified using RNeasy kit (Qiagen). 1µg of RNA per condition was used to retrotranscribe into cDNA with High Capacity cDNA Reverse Transcription kit (Applied Biosystems). To perform the qPCR, a set of primers was designed using NCBI primer designing tool (www.ncbi.nlm.nih.gov) (Supplementary Table 1, Appendix). All the amplicons were designed to span an exon- exon junction when possible. All primer sets were tested for primer efficiency using a six-fold dilution series containing six dilutions. qPCR was performed in 386 wells plates in ABI 7900HT SDS (Applied Biosystems) with (Master Mix SYBR Green Kit, Agilent, Santa Clara, CA). Every sample contained 2ng of total cDNA, 2,5µM of each primer in a final volume of 10µl. Conditions of Real Time quantitative PCR were as follows: 95ºC for 10min, then 40 cycles of 95ºC for 15s and 60ºC for 1min followed by a dissociation stage. Every condition was tested by 3 experimental replicates per gene. Experiments were conducted for an n=3-4.

4.1 Mathematical and statistical analysis

To analyze the data, HPRT gene was used as normalizer. Relative quantification analysis was used to determine the relative amount of RNA relative to 2D conditions in the planar cell polarity, the stiffness and the drug transporters screenings. To test gene silencing, the amount of RNA was relative to control siRNA sample. The Pfaffl model was used to calculate the N number (relative quantity of RNA relative to control) (Pfaffl, 2001):

$$N_{\text{gene A condition 1}} = \frac{E_{\text{gene A}}^{-\Delta CT\,(CT_{\text{condition1}} - CT_{\text{condition0}})}}{E_{\text{Normalizer gene}}^{-\Delta CT\,(CT_{\text{condition1}} - CT_{\text{condition0}})}}$$

E, represents the efficiency of the amplification (E ≤ 2) of the PCR. The efficiency was calculated for each gene by creating a standard curve with a gradient of concentrations of cDNA and calculating the slope of the straight line. CT is the cycle threshold, which is the cycle number at which the fluorescence generated within a reaction crosses the fluorescence threshold, a fluorescent signal significantly above the background fluorescence. At the threshold cycle, a detectable amount of amplicon product has been generated during the early exponential phase of the reaction. ΔCT is the difference between the CT of the two conditions examined (2D vs. micropatterns or Control vs KD). The three experimental replicates were used to calculate the standard error of the experiment. All the data with an SE > 50% was supressed and repeated.

5. Silencing by siRNA

siRNA sequences primers are listed in Table 1. For each gene, 25 nucleotide stealth siRNA duplexes targeting mRNA sequences were purchased from Sigma-Aldrich. Sequences were submitted to BLAST search to ensure targeting specificity and minimize off-targets. For siRNA transfection, MDCK cells were nucleofected using Amaxa Nucleofector-II (Lonza). Cell monolayers were rinsed with PBS for 20min and trypsinised for 10min to obtain a single cell solution that was centrifuged and resuspended in the nucleofection buffer containing 200µM siRNA and then nucleofected (program L-005). After 24h incubation, cells were again resuspended and plated either in 6-well plates, coverglass chambers coated with Matrigel to grow cysts or in micropatterns to grow tubes. Total cell lysates from 2D and 3D cultures were analyzed by immunoblotting or qPCR to confirm siRNA efficiency for the indicated time points.

Table1: Table shows siRNA sequences designed to down-modulate Fuzzy and Cesr1 expression. Sequences marked with an asterisk (*) were used to generate the presented data.

siRNA	Target sequence (5'-3')
Fuzzy_1*	CAUGGUUCUUCUUGUAGGACUUGA
Fuzzy_2	UCUCUCAAUGGAGUCCACAUGUUUG
Fuzzy_3	GAAGAAGGAGUUGAGGGCCAGUUAC
Celsr1_1	CCUCUGUUCUCCGAUUACAUGGAUU
Celsr1_2*	GAGCCCUGCGAGAACUACAUGAAGU
Celsr1_3	CCGUUGGAACGGUUAUCAUUGUCAA

6. Immunofluorescence

6.1 MDCK, LLC-PK1 and RPTEC/TERT1 monolayers and cysts

For Immunofluorescence (IF) of cells in 2D monolayers (over boroslicate coverslips), cysts (IBIDI chambers) and micropatterns, the cells were fixed in 4%PFA for 20min and then permeabilised with PBS+0,2%Triton Tx100+0,2%SDS for 10min at 4ºC. Cells were then blocked with PBS+3%BSA at room temperature for 30min (monolayers) or 1h (cysts and micropatterns). After that, primary antibodies were diluted in PBS+3%BSA and incubated for 30min at 37ºC in a humid chamber (monolayers) or 1h to overnight (cysts and micropatterns) depending on the antibody. After washes PBS+3%BSA secondary antibodies, phalloidin, DAPI or TO-PRO3 were incubated for 30min (monolayers) or 1h (cysts and micropatterns) in dark and then washed with PBS. Cells cultures as 2D monolayers and coverslip micropatterns (CYTOO chips and stiff PDMS coverslips) were mounted with Prolong Gold (Life-Technologies) over glass slides. Cells cultivated as cysts otr micropatterns in IBIDI chambers, were conserved with PBS+0.05% Azide at 4ºC for a maximum period of 2 weeks. To preserve chamber for longer periods of time, PBS+0.05% Azide was replaced with 200µl of fluoromount (Thermo Fisher Scientific). Soft PDMS and 3D micropatterns were glued to glass slides with a drop of fluoromont with the non-patterned surface facing the slide. Spreading vacuum grease around the patterns created a chamber around the patterns. 100µl of Prolong Gold were added over patterned side of the sample and a clean coverlip was fastened over the pattern.

6.2 Mammary gland organoids

They were fixed with 2% PFA (15min light shaking) and permeabilised with PBS + 0.5% TritonX-100 for 1hr at room temperature. After blocking with PBS + 10%FBS + 1%BSA for 2h at room temperature, organoids were incubated overnight at 4ºC with antibody solution (PBS +1%FBS + 1%BSA) plus the primary antibodies. Organoids were washed with PBS + 10%FBS (3X, 10min each) and incubated for 1h with antibody solution plus the secondary antibody, phalloidin-555,

and DAPI. After 3 washes with PBS, the chamber was removed by cutting it with a razor blade and the glass bottom coverslip was overlaid with PBS for imaging.

6.3 Mammary gland organoids on microchannels

Matrigel coated lid was carefully removed and both the micropattern and the lid were fixed with 2% PFA (15min light shaking). Once fixed, the lid is visualised under a microscope to assess the presence of attached structures. Normally, structures stay inside the microwells and the lid is usually discarded. Then, the samples are permeabilised with PBS + 0.5% TritonX-100 for 1hr at room temperature. After blocking with PBS + 10%FBS + 1%BSA for 2h at room temperature, microchannels were incubated overnight at 4ºC with antibody solution (PBS +1%FBS + 1%BSA) plus the primary antibodies. Organoids were washed with PBS + 10%FBS (3X, 10min each) and incubated for 1h with antibody solution plus the secondary antibody, phalloidin-555, and DAPI. After 3 washes with PBS, 3D micropatterns were glued to glass slides with a drop of fluoromont with the non-patterned surface facing the slide. Spreading vacuum grease around the patterns created a chamber around the patterns. 100µl of Prolong Gold were added over patterned side of the sample and a clean coverlip was fastened over the pattern. If the lid was also stained, it was mounted with Prolong Gold (Life-Technologies) over glass slides.

7. Antibodies

Table 2: The primary antibodies used in the present work.

Protein	Species	Reference	Dilution IF	Dilution WB
β-catenin	Rabbit	Santa Cruz Biotechnologies (sc7199)	1/500	-
Podocalyxin	Rabbit	ft Dr. Ojakian (State University of New Yorl Downstate Medical Center)	1/500	-
ZO-1	Rat	DSHB (R4076)	1/500	-
tylated-α-tubul	Mouse	Sigma-Aldrich Clone 6-11B-1 (T7451)	1/500	-
GM130	Mouse	Abcam (EP892Y)	1/300	-
PKC-ζ	Rabbit	Abcam (ab59364)	1/200	-
Ki67	Rabbit	ThermoFisher Scientific (RM-9106)	1/500	-
E-cadherin	Mouse	velopmental Studies Hybridoma Bank (rr1	1/500	-
Keratin 14	Rabbit	Sigma-Aldrich (SAB4501657)	1/200	-
Rab11	Rabbit	Life Technologies (715300)	1/500	-
Par-3	Rabbit	ThermoFisher Scientific (PA5-45056)	1/500	-
Laminin	Rabbit	Sigma-Aldrich (L9393)	1/500	-
Yap1	Rabbit	Cell Signalling Technology (4912)	1/200	1/500
p-MRLC	Rabbit	Cell Signalling Technology (3671S)	1/250	1/200
GGT1	Mouse	Santa Cruz Biotechnology (sc-166908)	1/200	1/500
OCT2	Mouse	Santa Cruz Biotechnology (sc-56822)	1/200	1/500
Megalin	Mouse	Santa Cruz Biotechnology (sc-515772)	1/200	-
Caspase3	Rabbit	Cell Signalling Technology (9661)	1/500	-
Paxillin	Rabbit	Abcam (ab32084)	1/500	1/500
GAPDH	Mouse	Santa Cruz Biotechnology (sc-32233)	-	1/1000
α -actinin4	Mouse	Covalab (pab0221)	-	1/1000

The secondary antibodies used in the present work are listed in Table 2.

Antibody	Species/Tracer	Reference	Dilution IF	Dilution WB
Anti-mouse IgG, HRP	Goat	Jackson Immunoresearch	-	1/5000
Anti-rabbit IgG, HRP	Goat	Jackson Immunoresearch	-	1/5000
ific Blue anti-Rabb	Donkey	Invitrogen (P10994)	1/1000	
Alexa Fluor 488 anti-Rabbit	Donkey	Invitrogen (A-21206)	1/1000	
Alexa Fluor 488 anti-Mouse	Donkey	Invitrogen (A-21202)	1/1000	
Alexa Fluor 555 anti-Rabbit	Donkey	Invitrogen (A-31572)	1/1000	
Alexa Fluor 555 anti-Mouse	Donkey	Invitrogen (A-31570)	1/1000	
Alexa Fluor 647 anti-Rabbit	Donkey	Invitrogen (A-31573)	1/1000	
Alexa Fluor 647anti-Mouse	Donkey	Invitrogen (A-31571)	1/1000	
Alexa Fluor 647anti-Rat	Goat	Invitrogen (A-21247)	1/1000	
TO-PRO-3	Nuclei	Invitrogen (T-3605)	00	
DAPI	Nuclei	Merck(268298)	1/1000	
Phalloidin-488	F-actin	Invitrogen (A-12379)	1/1000	
Phalloidin-555	F-actin	Sigma (P-1951)	1/5000	
Phalloidin-647	F-actin	Invitrogen (A-22287)	1/1000	

8. Microscopy

Zeiss laser scanning confocal microscopes LSM510, LSM710, two-foton LSM710 and Nikon AR1+ used for laser scanning confocal imaging. Objectives used were usually 40×/0.95 oil-Plan Apochromat and 63×/1.4 oil-Plan Apochromat (Zeiss) and a water-Plan Apochromat 40x/1.0 objective lens (Zeiss) was used for high magnification image acquisition of organoids. The analysis and composition of images taken from the microscopy were done with ImageJ, Fiji or Zen (Zeiss) programs. Then, images were treated using ImageJ software for producing x-z orthogonal slices, z-stack projections, and 3D deconvolution. For quantifications, more than three experiments were quantified. Significance was calculated using a paired, two-tailed Student's t test, and significant p-values are indicated in each experiment.

8.1 Time-lapse imaging

For live-cell imaging, MDCK cells stably expressing Podxl-GFP were seeded on CYTOOchips and incubated in CYTOOchambers for different times, according to manufacturer's instructions. Live imaging experiments were performed using incubator chamber accessories for each system at 37°C and 5% CO_2. Imaging medium was red-free complete MEM supplemented with 5%FBS, 3%Matrigel and 25mM Hepes. Images were acquired with a 40×/NA 0.60 dry objective using a

microscope AF6000 LX (Leica) and camera 885 EM (Andor). Metamorph was used for acquisition and video analysis and FIJI was used for video analysis.

9. Measurements and quantifications

The number of single lumen structures (cysts or tubes) was quantified considering one or two lumens as single lumen. In the case of tubes, if one of the lumens was longer than 2/3 of the total length of the tube, it was considered as single lumen too even if it had 3 or more lumens. When a tube had single or multilumen it was considered to be polarised.. When it has a 2D structure or inverted polarity it is considered as not polarised. The percentage of pattern coverage was quantified by measuring the length of the tube divided by length of the pattern in which it was adhered. Lumen height was defined as the z-axis of the lumen measured in a cross section. The longest lumen in tubes was measured as the length of the longest lumen in a tube divided by the total length of the tube. Aspect ratio was measured as the ratio between the size of the lumen in the y-axis (shortest axis) divided by the length of the lumen in the x-axis (longest axis) of a confocal image. The size of the lumens in cysts or isotonic and hypertonic media were quantified as the area of the cyst divided by the area of the lumen. The angle of tube walls with the substrate in fibronectin and laminin coated micropatterns was measured in cross sections of tubes in which the one of the sides of the angle was placed in line with the substrate and the other following the direction of the basal tube wall. The quantity of proliferating cells was measured as the percentage of ki67^{+} cells versus the total number of cells (visualised with DAPI). The survival rate was quantified as number of Caspase3^{-} cells versus number of cell (visualised with DAPI). For all the measurements, the number of independent experiments, the sample size and the statistical significance is specified in the figure legends.

9.1 Measurement of spindle orientation

To evaluate the spindle angle, pictures of mitotic cells within acini or in micropatterns were collected. When the two poles of the spindle were placed in different planes, a Z-stack was taken. ImageJ software was use to process images and measure angles. To measure the spindle orientation in the apicobasal axis, a line connecting the two spindle poles was drawn, and another line was drawn from the center of the apical membrane of the cell to the midpoint of the basal membrane, defining the apicobasal axis. The angle between the two lines was measured. When spindles oriented within 75°-90° from the apicobasal axis were considered to be correctly oriented. 30 spindle angles were measured in each experiment. Two different independent experiments were conducted .To measure the spindle angle in the tube axis, a line connecting the two spindle poles was drawn, and another line was drawn connecting the two ends of the tubes,

defining the tube axis. The angle between the two lines was measured. 30 spindle angles were measured in each experiment. Two different independent experiments were conducted.

9.2 Measurement of fluorescence intensity

Intensity of fluorescence was measured by pixel density of junctions connecting lumens and normal cell junctions. Every junction was measured three times and the average integrated intensity was calculated by multiplying by the junction length. The ratio between junctions connecting lumens and normal junctions was calculated for each tube. More than 6 junctions per tube were measured and more than 10 tubes were analysed in each experiment. Three different independent experiments were conducted.

10. Transepithelial resistance

Transepithelial resistance measurements MDCK and MDCK T-23 cells were trypsinised until single cell suspensions were obtained and plated onto ECIS plates (Applied BioPhysics) (100000cells/well in 200ml of culture medium). ECIS plate was connected to ECIS array station. ECIS plates were placed in an incubator at 37ºC for 48h with a single change of medium at 20h post seeding. TER was continuously measured as resistance (Ω) and posteriorly represented as normalized resistance, this is assigning 1 to time 0 (~500Ω) resistance and referring the records to this initial resistance. Graphic represent the average of 2 experimental replicates. Three different independent experiments were conducted, showing similar results.

11. Statistical analysis

To calculate statistical significance, the two-tailed Student's t-test was used. Significance level was set at 0.05. For small data sets, normal distribution was predicted from pooled data derived from previous similar experimental approaches (RNAi experiments, cyst formation quantification, tube measurements). For large data sets, we verified normal distribution using χ^2. In cases where variance was conspicuously different between two treatments Levene's test was used to verify. Most results are expressed as the mean ± standard deviation (SD). Sample size n is reported for each experiment in figure legends. All calculations were performed using Prism software.

RESULTS & DISCUSSION

I. DEVELOPMENT OF A MICROPATTERN-BASED SYSTEM TO MODEL RENAL TUBULOGENESIS

To design and fabricate an *in vitro* system to grow renal epithelial cells and recapitulate tube morphogenesis, we have used micropatterning technology. As there is no universal solution to produce micropatterns, a compromise between simplicity, reproducibility and excellence of patterning, together with an appropriate optical quality of the substrate has to be found. Different adhesive micropattern prototypes were designed using either photopatterning or µCP techniques. Each platform has different features and serves different purposes. However, all of the developed micropatterned systems rely on the supplementation with MG to provide apicobasal polarisation cues to allow cells to attain a 3D architecture. We have optimised the culturing protocol for three different renal epithelial cell lines as each of the cell lines impose specific growth requirements.

I.I Photopatterning-based prototype

In collaboration with the French company CYTOO SA we designed and micro-fabricated a cell culture device using photopatterning (Figure R1.A). This technique allows printing of the microfeatures on glass substrates, which provides a very an ecellent optical quality suitable to perform imaging experiments (Figure R1.B).

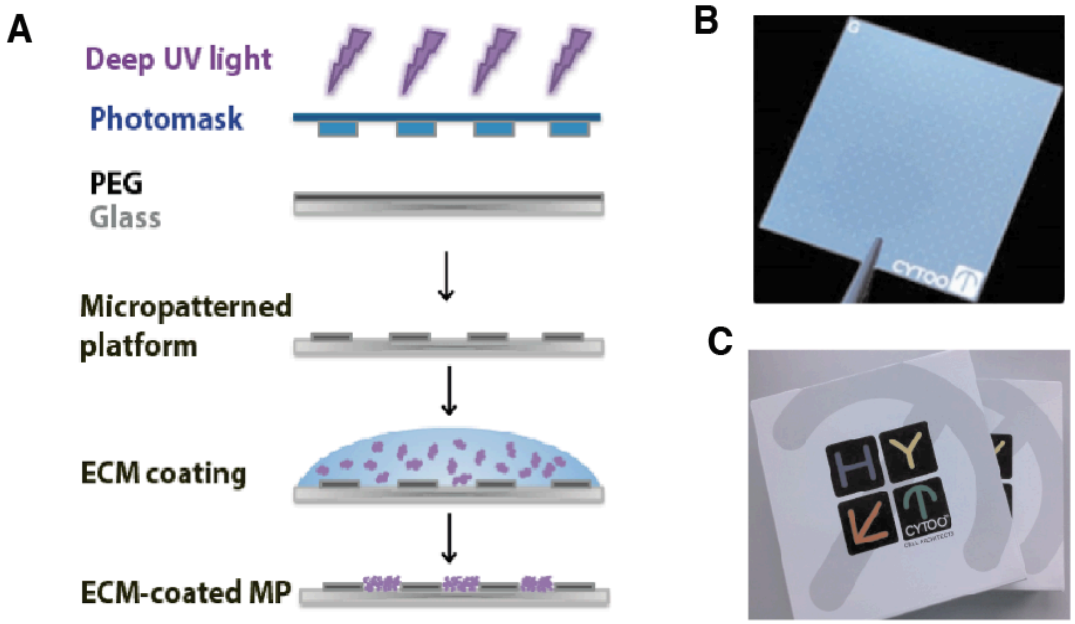

Figure R1. Micropatterning on borosilicate glass with deep UV light. **(A)** Photopatterning with UV light requires the design of a quartz photomask (blue) containing the microfeatures that will be printed on the culturing device. This photomask is exposed to deep UV light (<200nm) and placed onto a PLL-g-PEG-coated glass coverslip. The UV light oxidizes the PLL-g-PEG, destroying its anti-adhesive properties. These coverslips are then coated with soluble ECM proteins (in purple) that attach to the PLL-g-PEG-free surface. Since PLL-g-PEG is a cytophobic substance, seeded cells will only adhere to the ECM-coated regions, which will have the patterned shape. **(B)** Commercial CYTOO chips are 19.5x19.5 mm and made of high quality and low fluorescence borosilicate glass. Grid coordinates are also printed on the underside of the chip to provide orientation and location if required. **(C)** Selling format for CYTOO chips.

When designing the photomask, we had several factors into account (Figure R2). The first of them was the shape of the pattern. The most apparent shape to achieve a tubular structure is a line, so this was the canonical adhesive shape used in the majority of the following experiments. However, given the wide diversity of growing patterns occurring *in vivo*, other shapes were also taken into consideration like circular lines and S-shaped lines (Figure R2.A).

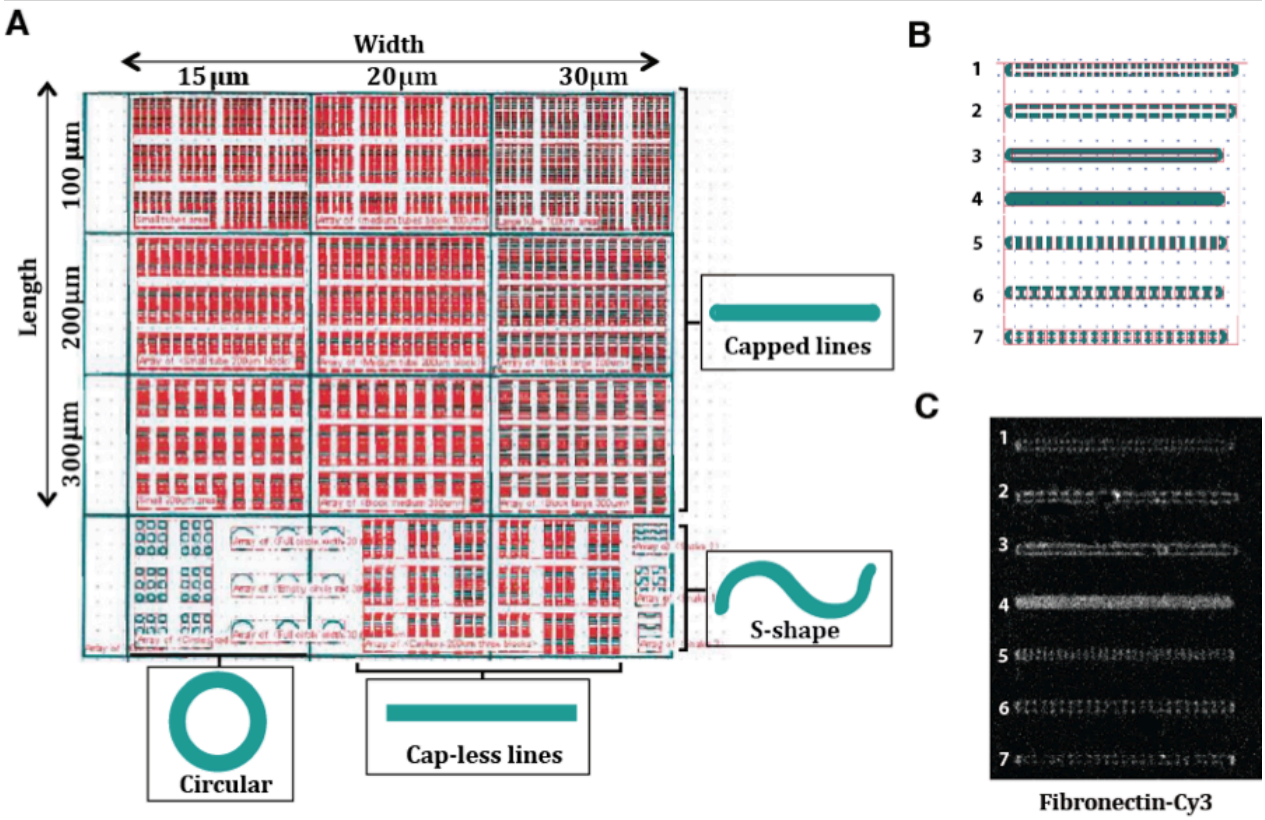

Figure R2. Maps representing the quartz photomask. **(A)** The designed mask has different shapes (green) and different sizes. Line lengths (upper) range from 100µm to 300µm and tube widths comprised between 15µm and 30µm. Lines are spaced with a 40µm gap in the vertical axis and with an 80µm gap in the horizontal axis. Canonical lines are capped at the ends providing a rounded end. Cap-less lines (lower center) have sharper squared ends and 200µm length and 20µm width. S-shapes (lower right) vary between 200µm to 500µm in length while S-shape patterns are 20 µm in diameter. Circular patterns (lower left) are 20µm width and have between a 50-100µm radius. Repetitions of the same patterns are separated from the others through a micropatterned grid composed of 40µm width continuous line. **(B)** Different adhesive configurations were designed (left). Adhesive areas are coloured in green while non-adhesive areas are in white. A number identifies each pattern. **(C)** Fluorescent microscopy image showing a micropatterned CYTOO chip with microfeatures was visualized by fibronectin-Cy3.

The second issue is the length of the patterns, corresponding to the AP axis of the tube. We selected three different measures based on the capability of adapting them to an automated quantification procedure and on the sizes able to fit into a microscopy image taken at high magnification (40X-63X). Patterns of 100µm, 200µm and 300µm were selected (Figure R2.A). Third, we also selected the width of the patterns that would be the dorso-ventral axis of the tube. We designed 15µm, 20µm, 30µm and 40µm in width patterns (Figure R2.A). Taking into account that the basal size of cells decreases through polarisation process, we expected these patterns to provide adhesion from 2 to 6 cells in a Y-cross-section of a fully polarised tube. The fourth concern was the configuration of

the adhesive areas (Figure R2.B-C). Seven different adhesive configurations were designed to analyse its effect on the formation of a continuous lumen and in the organisation of the FAs.

I.II Microcontact printing-based prototype

Photopatterning is especially suitable to perform glass patterning. However, we required a technique that allows patterning on other substrates with lower rigidity than glass to assess the role of matrix stiffness in tube formation. The above-mentioned technique, μCP, can be used to fabricate micropatterns on silicone substrates. Besides, the set up of the technology was easier and cheaper for our laboratory given the availability of materials and technologies. Using μCP techniques, we developed a device in which we could change matrix stiffness by printing on substrates different Young's Moduli values. The principles of μCP consist of the transfer of the microfeatures to an activated surface by direct contact with an ECM-coated stamp (Figure R3).

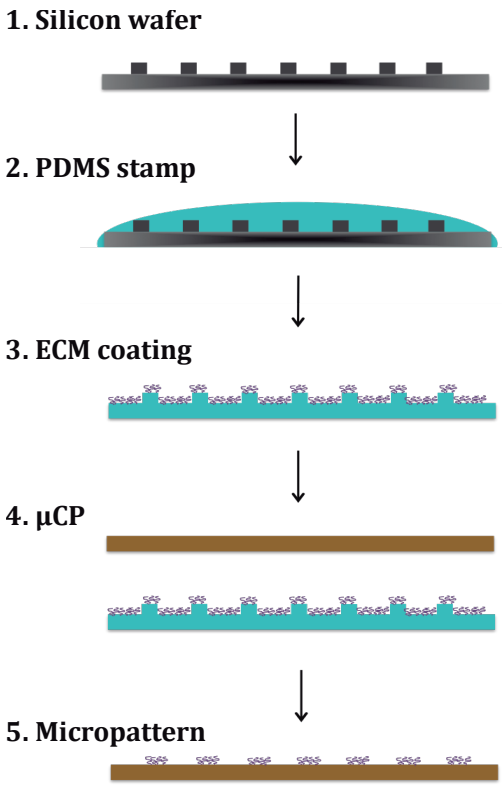

Figure R3. Microcontact printing. μCP requires an etched wafer (1) to replicate the features into a silicone stamp (blue). PDMS silicone is fabricated by mixing siloxane oligomers with a siloxane cross-linking agent, giving rise to a viscous solution that is poured over the silicon wafer (2). These stamps are then cured at high temperatures and, when solidified, they are peeled from the wafer and cut into pieces. The stamps are uniformly covered with ECM proteins (3). At the same time, the stamping surface is prepared. We do so, by coating clean and sonicated borosilicate coverslips with PDMS using a spin coater. The coverslips are then cured. Since the PDMS silicone is hydrophobic, it should be activated with an ozone-cleaner to oxidyse the surface. After this, coverslips are ready to be stamped (yellow line). μCP is performed by carefully putting the activated surface and the ECM-coated stamp in contact (4). Proteins are transferred from the non-activated PDMS stamp to the activated surface (5). To prevent cells from spreading out of the patterns, the activated surface is passivized by using a surfactant agent.

To perform μCP, we first designed a quartz photomask similar to that used for photopatterning on a silicon wafer (Figure R4). To design the photomask for μCP (Figures R4.C and R5.A), we followed similar principles to those used for the design of the photopatterning photomask (Figure R2). Some changes were done on the new design regarding the adhesive configurations as this second device was designed after the characterisation of the CYTOO micropatterns when we already knew the best conditions. For example, in this photomask, we only used full patterns (number 4, Figure R2.B-

C). We also modified the size of the gap between lines, making it wider (from 40µm to 150µm) to prevent adjacent tubes from fusing (Figure R5.B) and added some other patterns that could allow a different cell organisation (Figure R5.C).

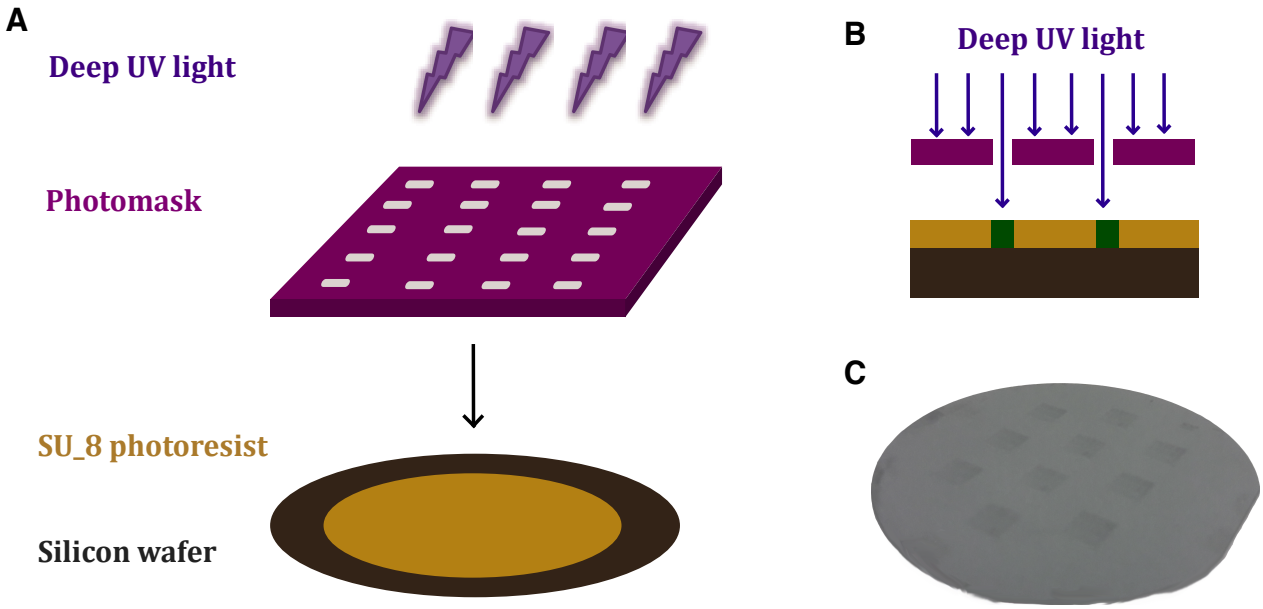

Figure R4. Microfabrication of the wafer. (A) Photolithography procedure was used to fabricate the silicon wafer. It uses UV light that passes through a photomask and etches the microfeatures on the wafer. **(B)** To generate three-dimensional features by photolithography, a SU_8 negative photoresist (yellow) was used. When exposed to 365nm light through a photomask, the exposed part crosslinks and becomes hard (green). After exposure, the wafer is developed and the not-crosslinked SU_8 photoresist is dissolved. **(C)** The resulting patterned silicon wafer.

When performing photolithography (Figure R4), the depth of the microfeatures can be controlled by modulating the UV light exposure time. We fabricated two silicon wafers with 20µm and 30µm in depth respectively. As the resulting silicon wafers (Figure R4) had three-dimensional microfeatures, they could be used to replicate the microfeatures into silicone stamps. These stamps were, then, used to do µCP on an activated PDMS surface (Figure R3).

The main improvement of the µCP technology compared to photopatterning is that we were able to fabricate micropattern on substrates of different stiffness. To obtain a very stiff matrix, we used IBIDI polymer®, which is a hard plastic suitable for µCP with Young's Modulus of around 1400MPa. To produce more compliant substrates we used PDMS silicone. We used PDMS because of its optimal rheological conditions, which make them suitable for cell culture. PDMS is viscoelastic, optically clear, inert, non-toxic and non-flammable so no other hydrogels or soft substrates were further used for simplicity. PDMS stiffness can be modulated depending on the curing temperature, the oligomer-crosslinker mixing ratio and the volume of PDMS. By varying these conditions, we could fabricate substrates with rigidities fluctuating between 2MPa and 0,2MPa [223-225].

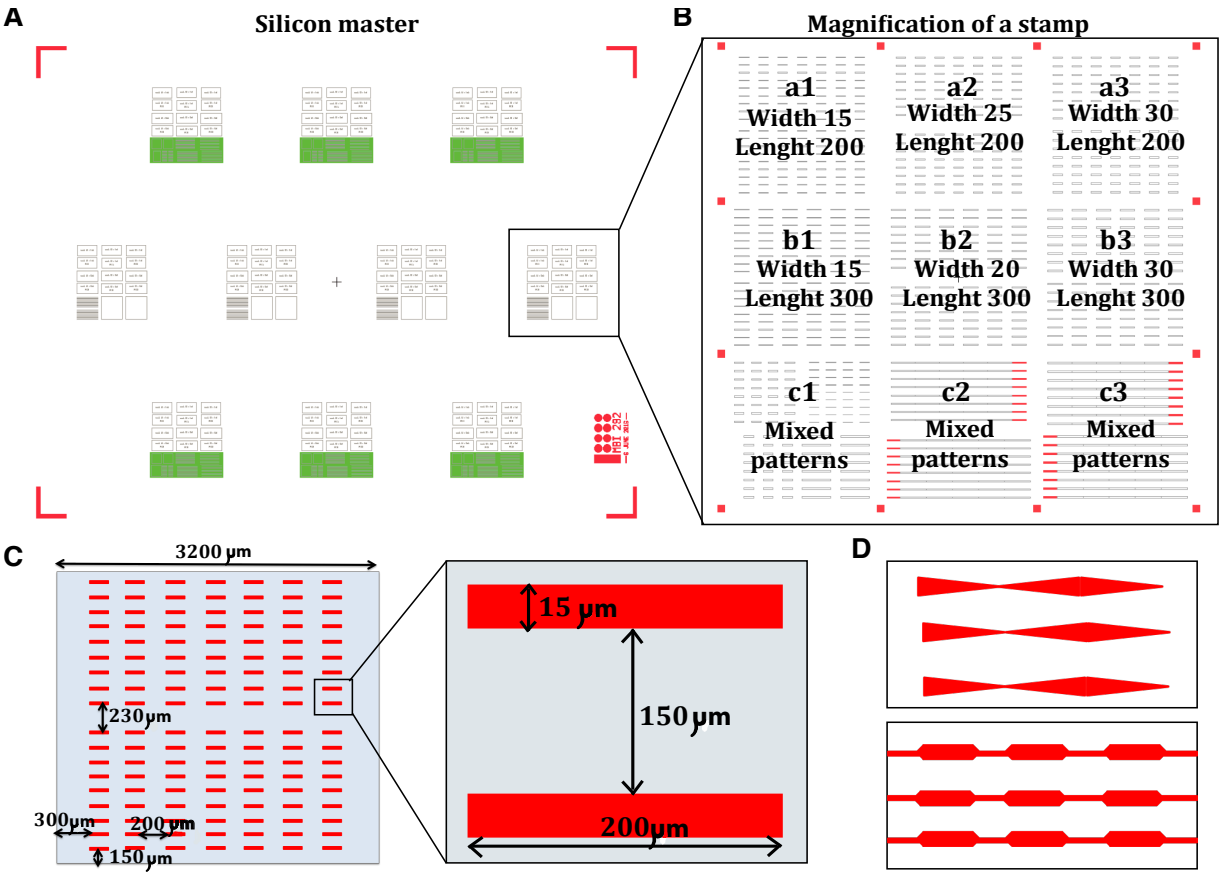

Figure R5. Design of the silicon wafer. (A) Schematic representation of the silicon wafer. Wafer contains ten stamps each of them measuring 1cm x 1cm with a spacing of 1cm from the adjacent stamps. Green boxes represent variable patterns that differ between stamps. **(B)** Magnification of a stamp. A letter and a number identify each set of patterns. Patterns in the upper row are 200µm in length and 15µm, 20µm and 30µm wide. Patterns in the middle row are 300µm in length and 15µm, 20µm and 30µm wide. Patterns in the lower row are composed of diverse features different from the canonical ones. **(C)** A magnification of a set of patterns from the a1 region. The dimensions of the patterns and the spacing regions are represented. **(D)** Examples of mixed patterns contained in the mixed regions c1, c2 and c3 of the stamps.

I.III Three-dimensional prototype

The prototypes mentioned above are 2D devices. However, we also developed a 3D prototype by using similar technology. While 2D platforms only permit the adhesion of the cells in the basal part of the tube, the 3D device allows cells located at the laterals regions of the tube to adhere to the substrate (Figure R6). By adding a third dimension to the platform, we created rectangular well-like microfeatures that could also provide physical confinement to the system.

A variety of methods to fabricate 3D micropatterns exist [226, 227], but we invented a simple technique, based again on µCP, to manufacture these devices. We used the same silicon wafer (Figure R4.C) to create a mould. This mould was silanised to make a negative countermould that was used to generate the 3D PDMS substrate. This last substrate was coated with ECM proteins that adhered to the whole PDMS surface. To remove the ECM proteins adhered outside of the micropatterned wells, we performed µCP repeatedly on an activated PDMS flat surface. Coating the micropatterns with ECM proteins conjugated to a fluorophore should be used to assess the

successfulness of the technique. By visualising the substrates under a fluorescence microscope, the absence of ECM proteins outside of the wells should be confirmed.

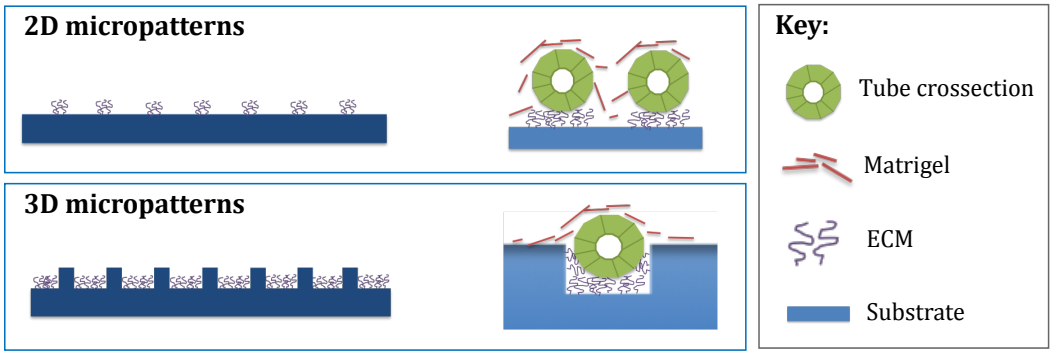

Figure R.6. Comparative analysis of 2D and 3D devices. While 2D devices (upper) only provide adhesion to the cells on the basal part of the tube, 3D platforms (lower), which have a well-like shape, provide adhesion also to the lateral parts of the tube.

I.IV Optimisation of the culturing procedure

The vast majority of studies using micropatterns have been done either with single cells or with a group of cells growing in 2D condition. However, building a tube *in vitro* requires a third dimension that, in this case, was provided by the supplementation with MG [87]. Taking this into consideration, we established a culturing protocol for three different renal epithelial cell lines: MDCK cells, Lewis-lung cancer porcine kidney 1 (LLC-PK1) cells and renal proximal tubule epithelial (RPTEC/TERT1) cells. In addition to adjusting the concentration of MG, other parameters were optimised such as the medium to be used, the FBS concentration, the number of cells to seed, and the ECM coating. The timing of the protocols was also determined as cell lines displayed different growing dynamics. All the protocols were established using the CYTOO chips, but its validity was confirmed on the other prototypes. The following table (Table R1) summarizes the optimised conditions to grow tubes in micropatterns for the three cell lines used.

Table R1. Summary of the optimised culture conditions for three renal epithelial cell lines to grow tubular structures on CYTOO micropatterns.

Cell line	Medium	Growth time	Matrigel	FBS	Num. of cells
MDCK	MEM	3 days	3%	3%	60000 cells
LLC-PK1	M199	3 days	1%(for 24h) – 3% (for 48h)	10%	100000 cells
RPTEC/TERT1	DMEM F-12	14 days	3.5%	3%	400000 cells

I.IV.I Optimisation of the protocol for MDCK cell line.

MDCK cell line is a long established canine epithelial cell line isolated from the nephron collective duct. It is a widely used cell line, especially indicated to study epithelial cell polarity, vesicle trafficking and cell dynamics. MDCK rapidly acquire apicobasal polarity when culture in porous

filter supports or in the presence of an extracellular matrix (i.e. collagen gel or MG) [65]. Providing an extracellular matrix substrate allows MDCK cells to grow in cyst-like structures resembling an epithelial organ, which permits the study of the early cellular events occurring during epithelial morphogenesis. Thus, this cell line was selected as the most suitable to perform tubulogenesis studies *in vitro*. We designed a protocol that allows cells both to adhere to the micropatterned surface and the acquisition of a 3D architecture by providing a MG-supplementation step following cell adhesion (Figure R7*).*

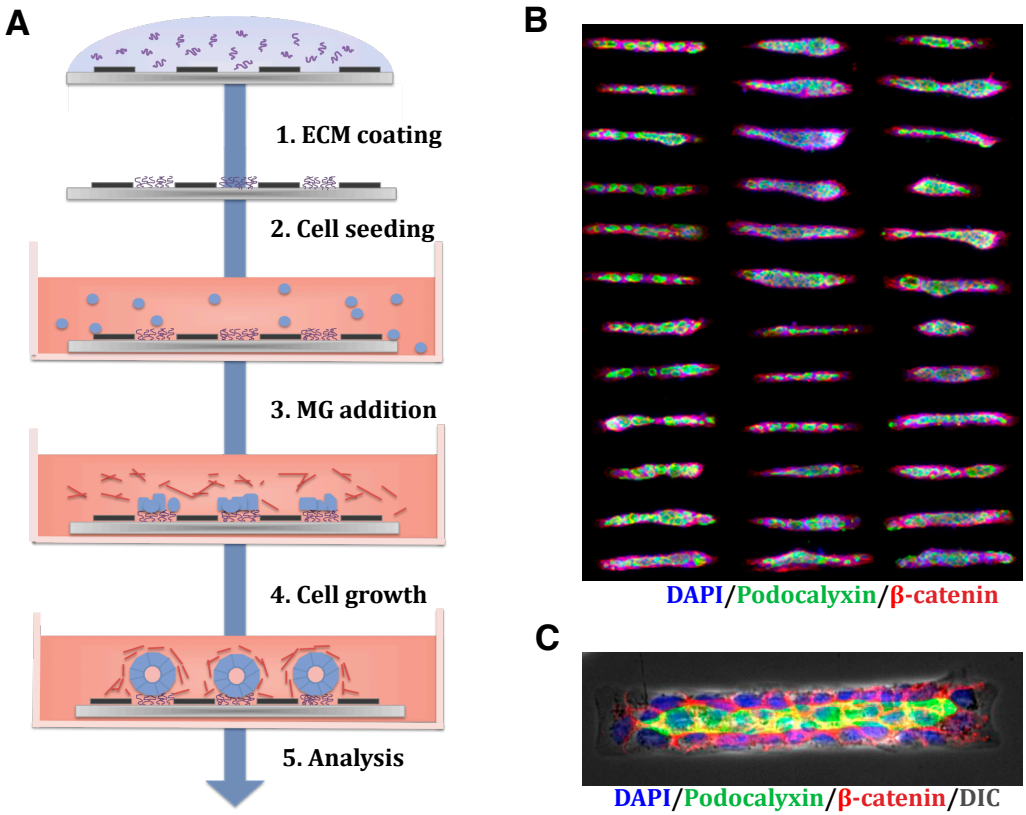

Figure R7. Protocol to grow MDCK cells on CYTOO chips. (A) Chips are coated with a solution of purified ECM components (1) and cells are seeded on top (2). After cells adhere to the micropatterns, MG solution is added to the medium (3). Micropatterns are then placed in the incubator until cells reach a tubular structure (4). At that point, they are suitable for cell imaging, or for biochemical studies (5). **(B)** Image of different MCDK tubes growing on CYTOO chips. Images of single tubes were taken individually. **(C)** Example of MDCK cells grown on a micropattern for 72 hours.

MDCK cells were able to acquire a tubular shape when growing on micropatterns coated with different ECM proteins (Figure R8.A). Differences in tube morphology depending on ECM coating were analysed and are presented in a different part of this section. The optimal cell number was also assessed. Around 45000 cells per chip allowed cells to cover the patterns and grew inside the adhesion zone while overcrowding the patterns by seeding too many cells resulted in cells migrating outside of the patterns (Figure R8.B). We also determined optimal serum concentration and found that the addition of 3%FBS resulted in a higher number of hollowed tubes. When supplementing the medium with 10%FBS cells spread out of the patterns and tubes presented abnormal polarisation (Figure R8.C-D). MG addition provided the cues to polarise in 3D. Assessing

when to add the MG and which concentration would impact the formation of the lumen. We found that it is necessary to add the MG after cell adhesion since adding it before cell seeding or at the same time as cells are added, promoted cell migration out of the patterns because MG deposits covering the hydrophobic regions of the patterns and provides further adhesion to cells. Besides, as MG surrounded the cells and the micropattern-based restricted adhesion was abrogated, cells could grow to form rounded structures resembling cysts. (Figure R8.E-F). Besides, MG concentration is also critical as low concentration produced inverted apicobasal polarisation and absence of lumens while too high concentrations resulted again in the deposition of MG over the whole surface, which endorsed cell spreading outside of the patterns (Figure R8.G).

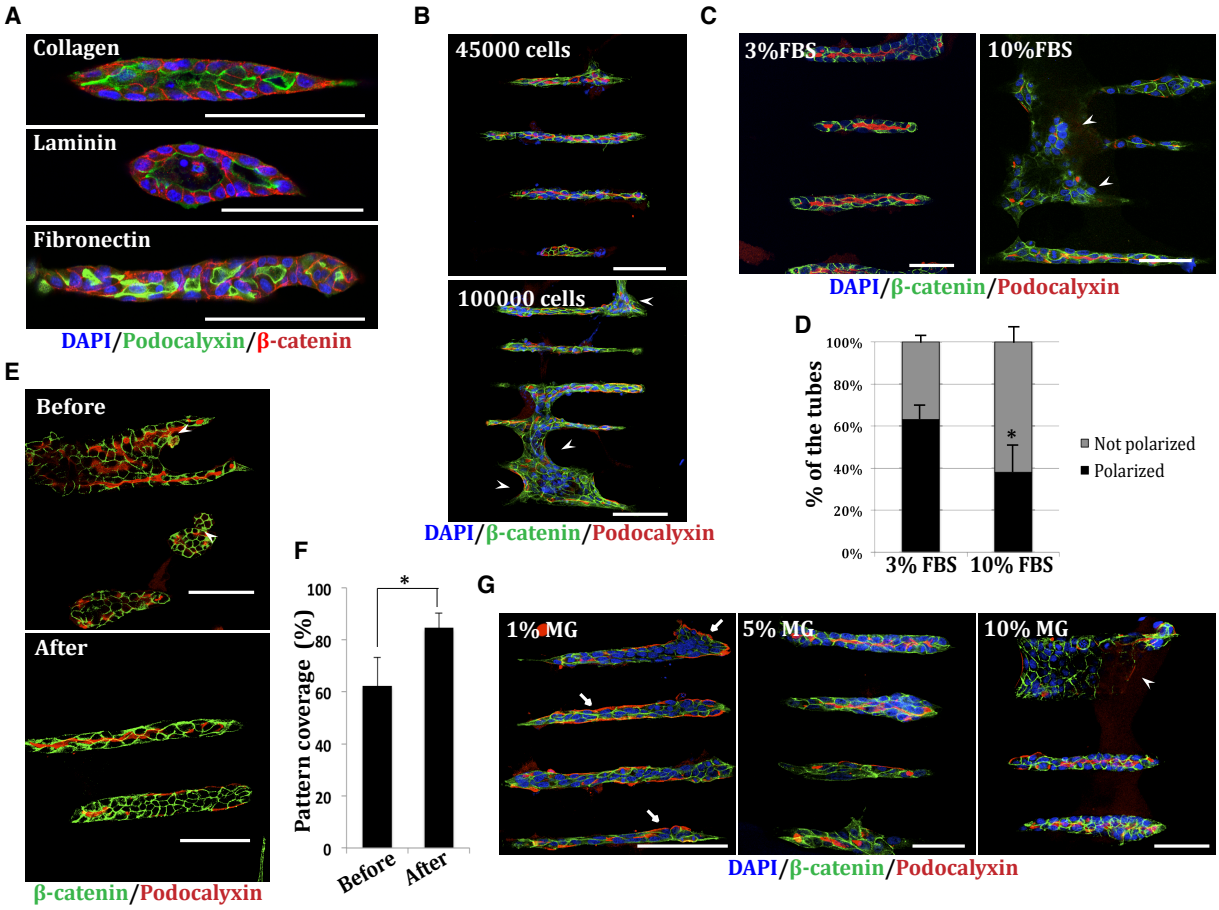

Figure R8. Optimisation of the culturing conditions to grow MDCK tubes on micropatterns. (A) MDCK cells growing on different ECM components present a polarised architecture within 72h. 60000 cells were seeded in collagen-IV, laminin or fibronectin-coated micropatterns. Culture medium was supplemented with 3%FBS and 3%MG. Scale bar, 100µm. **(B)** 45000 cells and 100000 cells were seeded in micropatterns. Arrowheads indicate zones where cells spread outside of the patterns. Scale bar, 100µm. **(C)** MDCK cells cultured in micropatterns and supplemented with 3%FBS and 10%FBS respectively. Arrowheads indicate zones where cells spread outside of the patterns. Scale bar, 100µm. **(D)** Quantification showing a higher percentage of tubes polarised with a 3D architecture in tubes grown in 3%FBS compared to tubes grown on 10% FBS (right). Values are mean ±SD from three different experiments (n>50 tubes/experiment; *, P<0,05). **(E)** MG supplementation done either before cell seeding (upper) or once cells are attached to micropatterns (lower). Arrowheads indicate tubes that do not spread correctly on the patterns and acquire a rounded shape. **(F)** Quantification shows the percentage of the micropattern length covered by cells in both conditions. Values are mean ±SD from three different experiments (n>50 tubes/experiment; *, P<0,05). **(G)** Tubes grown in 1%MG, 5% MG or 10% MG-supplemented medium. Arrows indicate tubes with inverted polarity in which Podxl is in contact with the ECM. Arrowheads indicate zones where cells spread outside of the pattern. Scale bar, 100µm.

I.IV.II Optimisation of the protocol for LLC-PK1 cell line.

LLC-PK1 cells are porcine renal epithelial cells from the proximal tubule of the nephron. The proximal tube is the part of the nephron in charge of drug secretion and reabsorption, a process through which drugs are concentrated inside the cells, causing nephrotoxic effects. Thus, LLC-PK1 cell line has mostly been used as a model to perform pharmacological studies but also to study intracellular trafficking. This cell line is interesting to our work since we also wanted to set-up the micropatterned device to be used as a platform to perform nephrotoxicity assays.

While MDCK 3D cultures have been long established and widely characterised, studies using LLC-PK1 cells have been performed in epithelial monolayer configurations. Given the protocol that we have designed to culture MDCK cells on micropatterns, we also optimised a culture procedure to grow LLC-PK1 tubes.

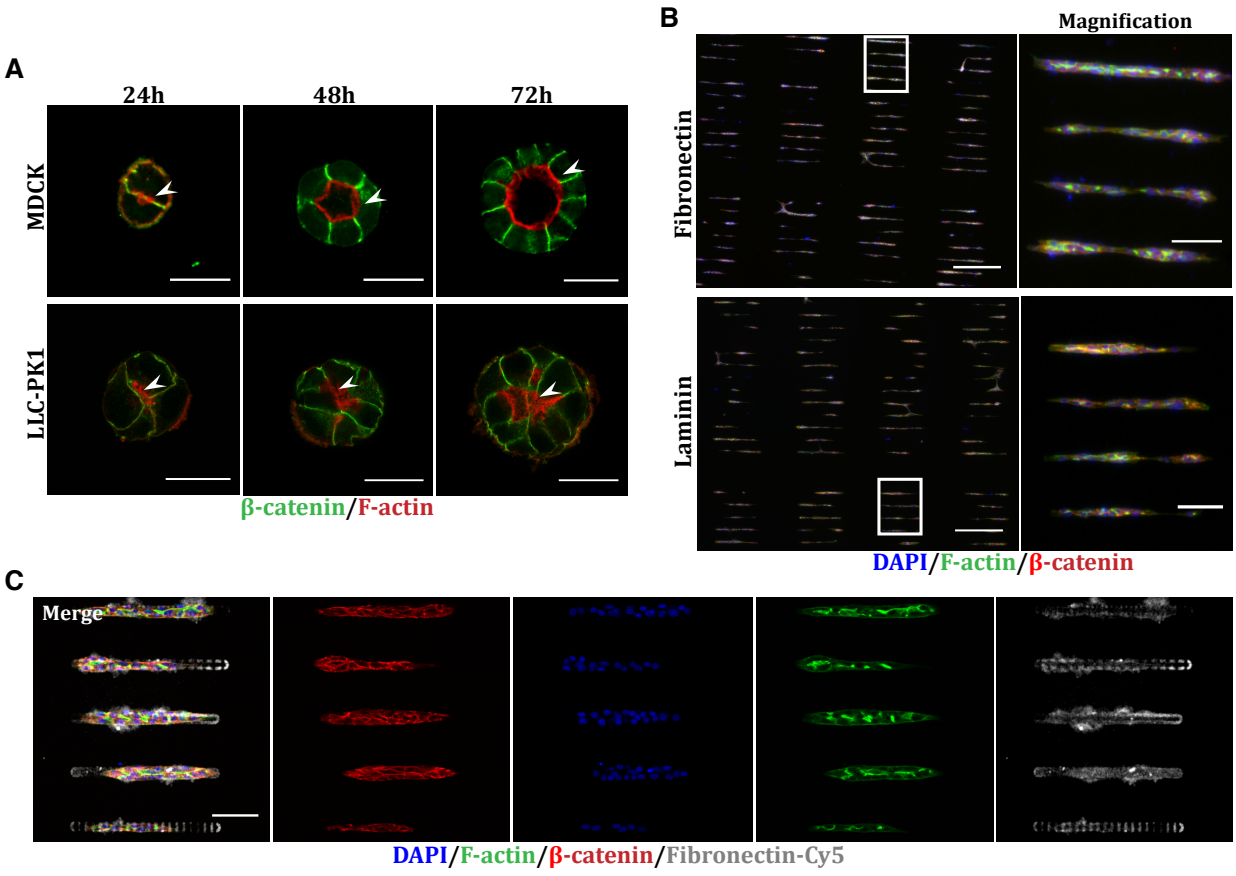

Figure R.9. Apico-basal polarisation of LLC-PK1 cells in MG-based substrates and micropatterns. (A) Time-course of MDCK (upper panels) and LLC-PK1 cysts (lower panels) growing on MG. Arrowheads indicate the forming lumen stained with F-actin. Note the larger microvilli of LLC-PK1 cells. Scale bar, 20µm. **(B)** Tile scan of LLC-PK1 tubes growing on fibronectin-coated micropatterns (upper) and laminin-coated micropatterns (lower) for 72h. The medium is supplemented with 3% FBS and 3% MG. Scale bar, 200 µm. Magnification scale bar, 50 µm. **(C)** Tubes of LLC-PK1 growing on micropatterns. The different pattern configurations are visualized by Fibronectin-Cy5. Scale bar, 50µm.

LLC-PK1 cells were able to grow in 3D-like structures similar to MDCK cysts when growing them on a MG-based substrate. They could acquire apicobasal polarity and formed luminal cavities (Figure R9.A). These lumens were less opened and with longer microvilli, resembling proximal tubules.

Knowing that LLC-PK1 cells can polarise in response to ECM and form a 3D structure, we primed them on micropatterns following conditions similar conditions to those used for MDCK. We introduced some slight variations in the protocol (Table R1). We found that they formed hollowed tubes when cultured on micropatterns coated with laminin and fibronectin (Figure 9.B), being able to grow over different pattern configurations. (Figure 9.C).

However, they displayed some morphological differences when compared to MDCK tubes, including different cell spreading and lumen size (Figure R10). LLC-PK1 cells were slightly better spread on fibronectin-coated patterns than MDCK cells, which presented a lower percentage of pattern coverage. (Figure R10.A-B). Regarding lumen morphology, MDCK lumens on fibronectin patterns were bigger in diameter than LLC-PK1 lumens (Figure R10.C-D), although the exact size of LLC-PK1 lumens was difficult to assess because the long microvilli occluded the lumen.

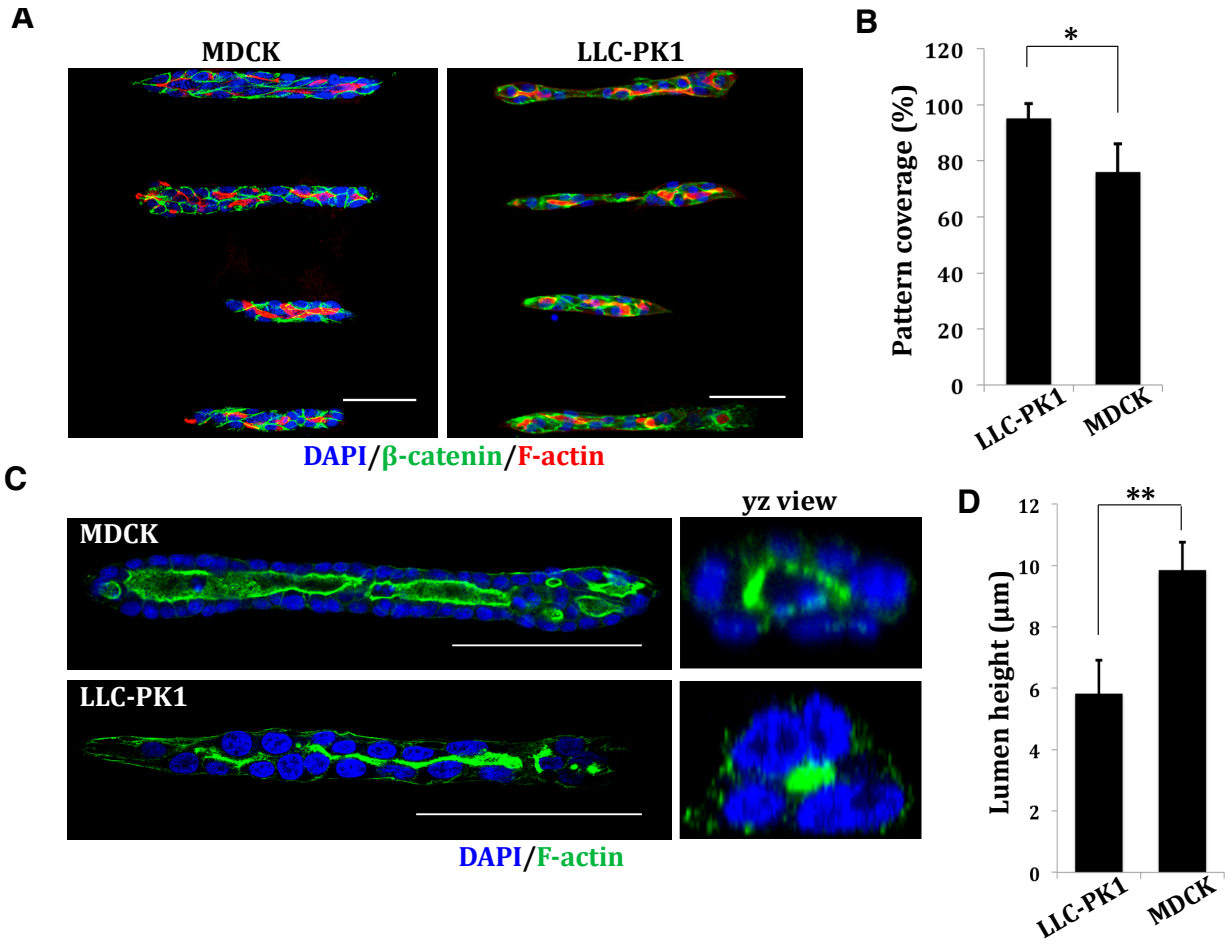

Figure R10. Comparative analysis of MDCK and LLC-PK1 tubes (A) MDCK (left panel) and LLC-PK1 (right panel) tubes growing on fibronectin-coated micropatterns. Scale bar, 500µm. **(B)** Quantification shows the percentage of the micropattern length covered by MDCK and LLC-PK1 cells respectively. Values are mean ±SD from three different experiments (n>50 tubes/experiment; *, P<0,05). **(C)** Tubes of LLC-PK1cells growing on micropatterns. The different pattern configurations are visualized by Fibronectin-Cy5. Scale bar, 50µm. **(D)** Quantification shows the lumen height in µm measuring the top-bottom diameter of the lumen in cross-sections of MDCK and LLC-PK1 tubes, respectively. Values are mean ±SD from three different experiments (n>50 tubes/experiment; **, P<0,01).

I.IV.III Optimisation of the protocol for RPTEC/TERT1 cell line.

RPTEC/TERT1 is a relatively new human renal cell line from the proximal tubule. RPTEC cells are transformed with human telomerase reverse transcriptase (hTERT) and present similar characteristics to those of primary cell lines. This cell line has been mostly used for toxicology assays in 2D monolayers [228].

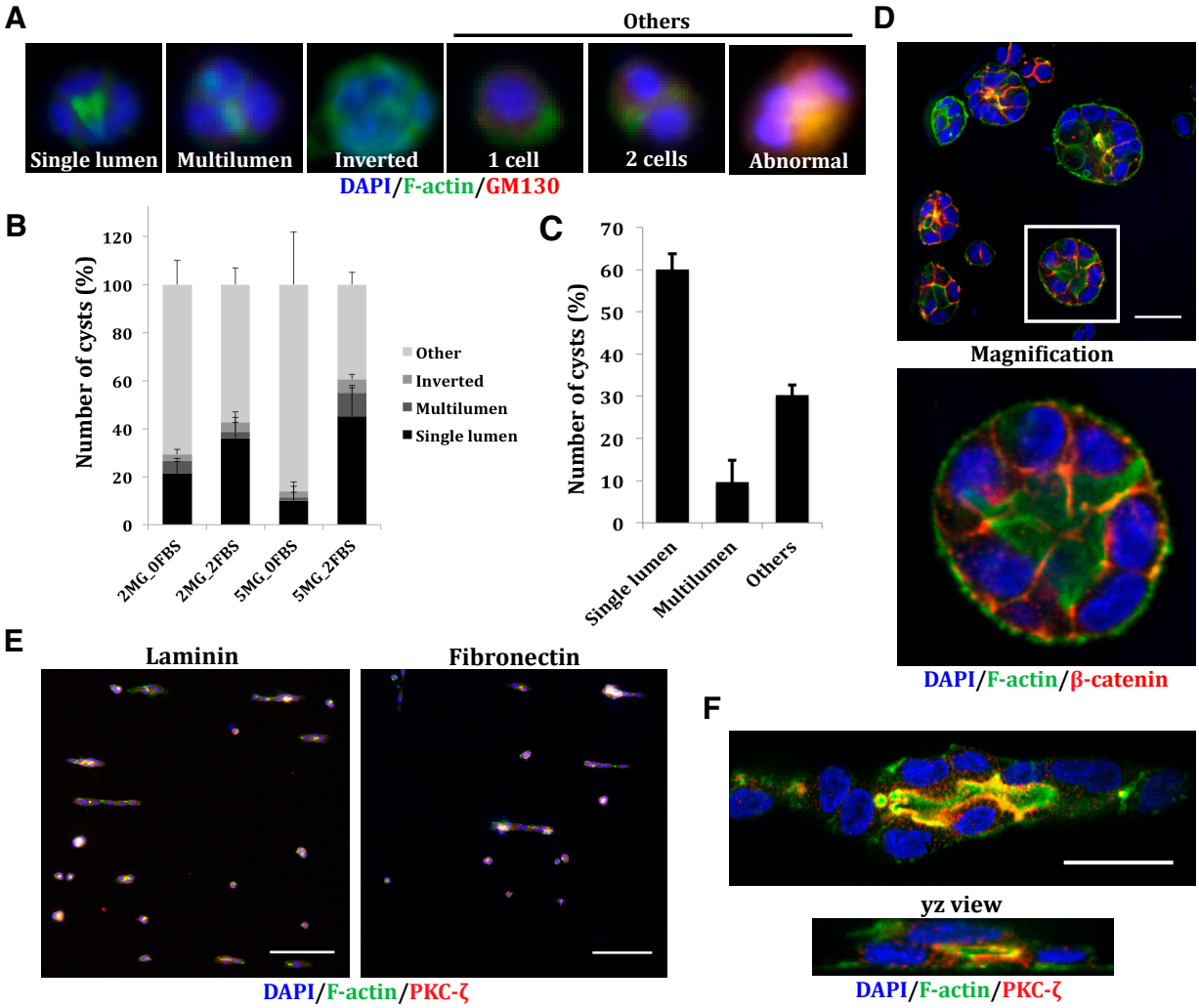

Figure R11. 3D culture of RPTEC/TERT1 cells (A) Classification of the different morphologies of RPTEC/TERT1 cells growing on MG-coated substrates for four days **(B)** Quantification shows the percentage of four days RPTEC/TERT1 cysts displaying the morphologies described in (A). Cells were grown for four days on different culture conditions. Values are mean ±SD from three different experiments (n>50 cysts/experiment). **(C)** Quantification shows the percentage of 14 days RPTEC/TERT1 cysts displaying the morphologies described in (A). Cysts were cultured in medium supplemented with 5%MG and 2%FBS. Values are mean ±SD from three different experiments (n>50 cysts/experiment). **(D)** 14 days RPTEC/TERT1 cysts growing in MEM supplemented with 5%MG and 2%FBS. Note, single lumen shown in the magnification (lower). Scale bar, 50µm. **(E)** 14 days RPTEC/TERT1 tubes growing on laminin- and fibronectin-coated micropatterns. Scale bar, 200µm. **(F)** 14 days RPTEC/TERT1 tube growing on laminin. Note, yz view (lower) shows cells enclosing the lumen. Scale bar, 50µm

As a first approach, we set the protocol for the growth of RPTEC/TERT1 cysts in an ECM-rich substrate. We tried different FBS and MG concentrations, among others. For a 4-days culture, we observed some different phenotypes regarding the cysts' morphology (Figure R11.A). We selected the combination of factors that gave a higher number of cysts with a single lumen (Figure R11.B)

and cultured them under these conditions for longer periods of time. In a 14-days culture we could observe a very high rate of mature cysts with single opened lumens (Figure R11.C-D). Based on these results, we cultured RPTEC/TERT1 cells on micropatterns coated either with fibronectin or laminin. By 14 days culture, we could observe both structures with a tubular shape and tubes with cyst-like morphologies (Figure R11.E). Those structures presenting a tubular configuration did have a central lumen surrounded by cells as shown by confocal microscopy (Figure R11.F).

I.IV.IV Optimisation of the protocol for 3D topography patterns

Besides the 2D platform, we also developed a novel approach for tube formation on a 3D device (Figure R6). To provide extracellular cues for the cells to polarise we set-up two different strategies. Either we supplemented the growing medium with MG or we created microchannels by using MG-coated coverslips as caps, placing them at the top of the platforms (Figure R12.A).

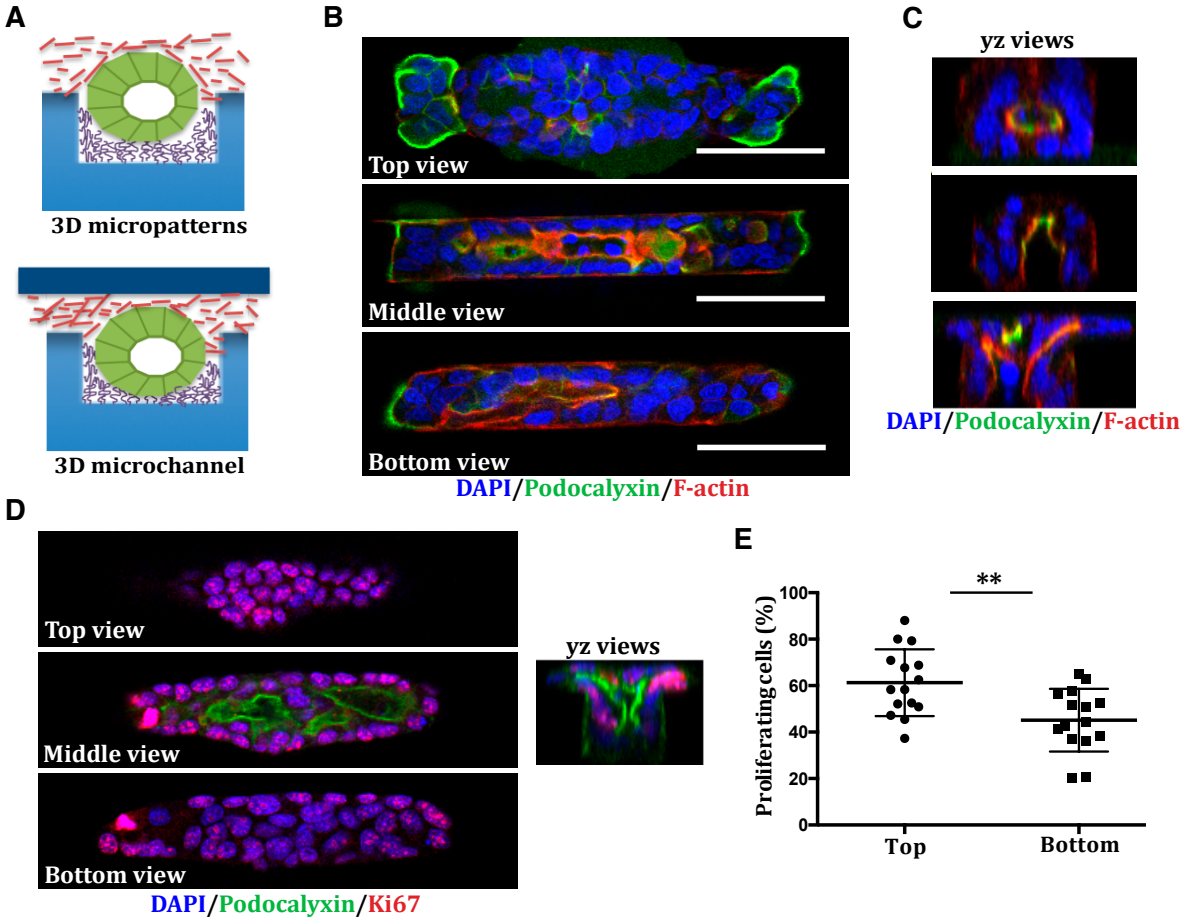

Figure R12. Culturing MDCK cells on 3D micropatterns (A) Schematic images showing cells cultured on 3D micropatterns growing on MG supplemented medium (upper) or in microchannels done by covering the cells with MG-coated coverslip. **(B)** Different confocal sections of an MDCK tube growing on a 3D micropattern. Sections are from the upper part of the tube exposed to the culture medium, the middle and the bottom part where cells attach to the ECM. Scale bars, 50µm **(C).** yz views of confocal stacks taken from three tubes showing different morphologies. **(D)** Tube stained with a proliferation marker (Ki67) and yz view (right). Note, Ki67 staining changes depending on the region of the tube. **(E)** Quantification shows the percentage of proliferating cells in the top and the bottom slices of tubes growing on 3D micropatterns. Values are mean ±SD from 15 different tubes (n>50 cells/tube; **, P<0,01).

These 3D-micropattern devices prevented cells from growing out of the patterns and better confined them into a tube-like shape with cells enclosing a central lumen (Figure R12.B; Figure R12.C, upper). However, when the MG-coated lid is not used, MDCK cells acquired different morphologies as they could grow outside of the pattern (Figure R12.B, top view; Figure R12.C, lower) or were able to detach from the basal part of the microwell (Figure R12.C, middle). The proliferation rates at the different sections of the tubes indicated that the basal part of the tube provided higher confinement as fewer cells were proliferating when compared to the top part, where the absence of a MG-coated lid allowed cells to grow in a less compressive environment (Figure R12.D-E).

Although renal epithelial cells are the main cellular model in this study, we also optimised the technology to culture mouse mammary gland organoid-derived cells in micropatterns. Mammary gland organoids are multicellular structures that, when embedded in MG, organise as an epithelial sheet that encloses a central lumen and is surrounded by a layer of myoepithelial cells in contact with the MG. (Figure R13.A). To grow tubular structures, mammary gland organoids needed to be disaggregated by trypsinisation so individual cells could fit inside the microwells. By doing this, we were able to grow tubular structures in fibronectin-coated microchannels, with cells acquiring a similar structure to that of organoid growing in pure MG (Figure R13.B). Myoepithelial cells were disposed in the external part of the tube and epithelial cells surrounded a central lumen as soon as at three days of culture (Figure R13.B). To date, organoids have been grown in non-patterned substrates or microwells biomaterials [229] but with this technique, we have been able to provide a physical constraint to control organoid tubular shape and confinement.

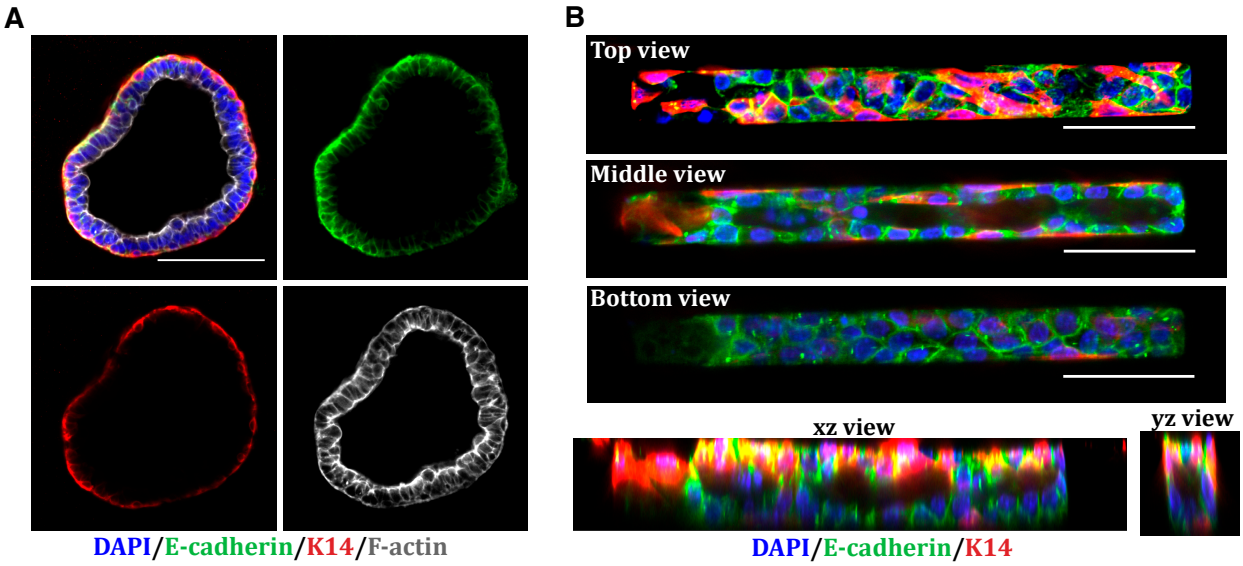

Figure R13. Culturing mammary gland organoids on micropatterns (A) 3 days mouse mammary gland organoid. Note that luminal epithelial cells (green) are surrounded by myoepithelial cells (red). Scale bar, 100µm **(B)** Different confocal sections of mammary gland organoid-derived cells growing on a 3D channel. Sections are from the upper part of the tube exposed to the MG-coated coverslip, the middle, and the bottom part where cells attach to the ECM. Note, xz and yz views show cells enclosing the central lumens. Scale bars, 50µm.

I.IV *In vitro* tubulogenesis as a physiological model

For this micropatterned device to be used both to perform epithelial tubulogenesis studies and nephrotoxicity assays *in vitro*, epithelial cells should be able to mimic those morphogenetic processes occurring *in vivo*. As mentioned in the introduction, tubulogenesis occurs through different mechanisms depending on the organ. Particularly, during gut morphogenesis, epithelial cells acquire apicobasal polarity, form and expand lumens and by junction remodelling, these lumens coalesce into a single opened cavity (Figure R14.A) [26]. Using our *in vitro* device, we analysed the steps of tube formation to examine whether tube formation on micropatterns resembles the mechanism of tube formation *in vivo.* We used MDCK cells as they are known to form lumens *de novo* when growing in MG [65]. Knowing that the acquisition of apicobasal polarity is a critical step in tube formation, we did time-lapse microscopy to track tube formation in MDCK cells stably expressing the apical marker Podxl-GFP. Cells were grown on micropatterns for 72h (Figure R14.B-C). As observed in the still images, small lumens appeared at early stages. These lumens expanded and fused to adjacent lumens, mimicking the physiological process [26].

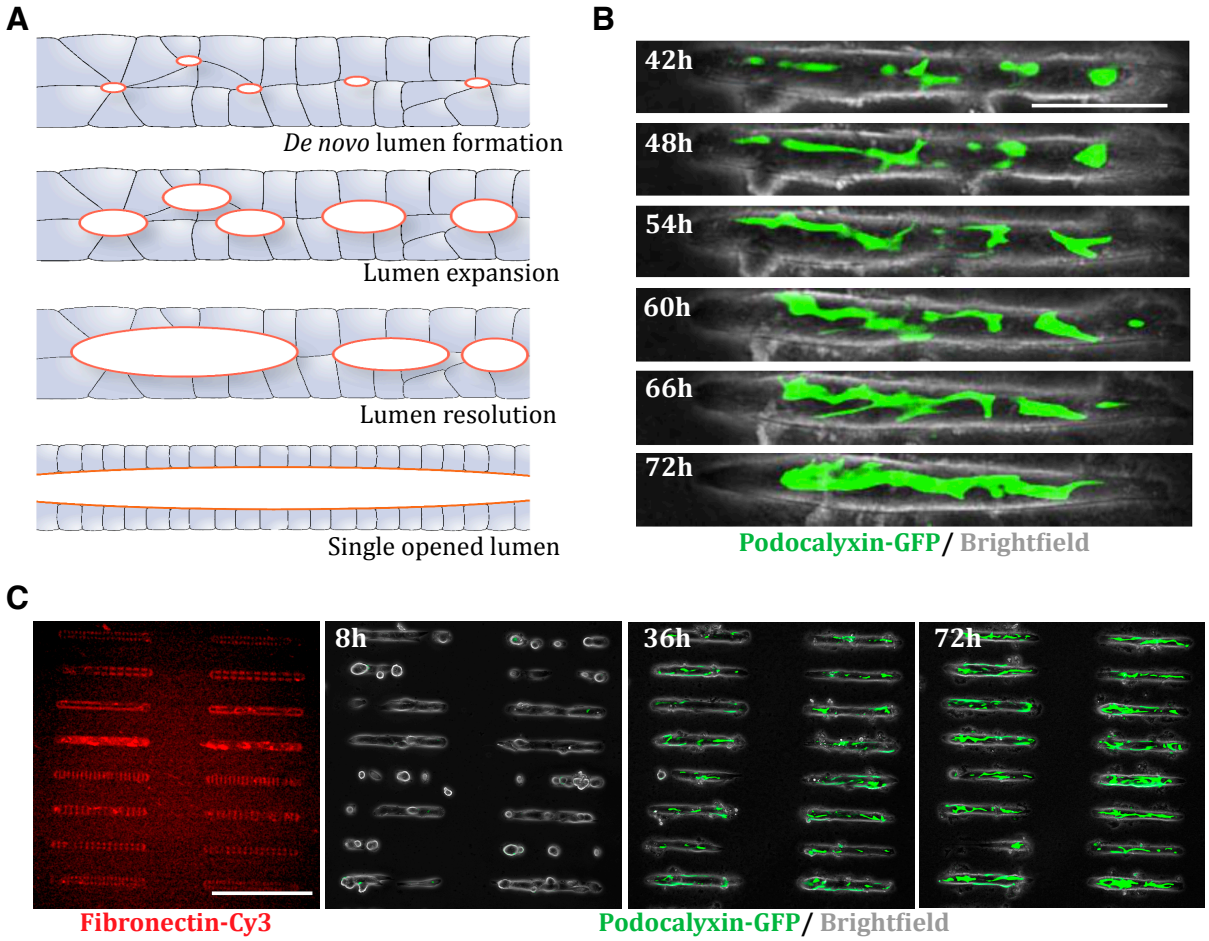

Figure R14. Tube formation in micropatterns resembles tube formation *in vivo* (A) Schematic representation of tube formation *in vivo.* **(B)** Time-lapse images of MDCK cells stably expressing Podxl-GFP growing on micropatterns. Scale bar, 50µm. **(C)** Time-lapse images of MDCK tubes stably growing on micropatterns. Micropattern configurations are visualized by fibronectin-Cy3 (right). Note, tubes can grow out of single cells or from a group of cells. Scale bar, 200µm.

The traditional models used in our laboratory to study epithelial morphogenesis are *in vitro* 3D organotypic cysts and *in vivo* zebrafish gut and pronephros tubes. This combined strategy is generating exciting new insights on the coordinated development of cell polarity and lumen formation in epithelium [61]. Additionally, as a result of a narrow collaboration between our lab and CYTOO SA, a new method for the formation of epithelial structures on micropatterns was characterised and patented (EP11305965) [87]. The invention describes a method to construct epithelial acini with a defined optimal size, shape and number of cells within three days of culture. Taking advantage of this method, we have generated a device able to mimic the fundamental steps of tube formation *in vitro* (Figure R14). Besides, we have optimised the technique to grow different renal epithelial cell lines. The *in vitro* platform will allow the control of the size and shape of the adhesive area providing additional extracellular constraints to guide tube formation. We are also able to control the composition of the ECM and the stiffness of the substrate. These tuneable conditions will permit the evaluation of the contribution of extracellular signals in shaping tube architecture. Furthermore, the fabrication of the 3D micropatterns allows the control of cell proliferation by physically confining cells into a restricted area (Figure R12). Morever, 3D microchannels provide the optimal environment for mammary gland-derived organoids to organise into a tubular architecture (Figure R13). Finally, the production of this organ-on-a-chip device could be useful to deeper study the role of environmental cues in tubulogenesis, to depict the molecular and cellular events underlying lumen coalescence and to conduct nephrotoxicity and drug discovery assays.

II. MORPHOLOGICAL CHARACTERISATION OF MDCK TUBES GROWING ON MICROPATTERNS

MDCK tubes growing on micropatterns did show similar growing dynamics to that of developing tubes *in vivo* (Figure R14). We next investigated how these tubes form and how environmental constraints affect their morphology and organisation. When tubes grew on CYTOO micropatterns, they acquired the shape of the adhesive area and grew in 3D due to the polarising cues provided by the MG (Figure R15.A). However, during growth, tubes could adopt different morphologies depending on how they polarise (Figure R15.B). They could either acquire polarity and form a large lumen (single lumen, when one or two lumens are formed or a lumen larger than 2/3 of the total length of the tube is formed) and small lumens (multilumen) or stay in a 2D configuration acquiring an inverted polarity phenotype (not polarised) (Figure R15.B). Most of the tubes growing in the established culture conditions were polarised and the percentage of polarised tubes increased over time (Figure R15.C).

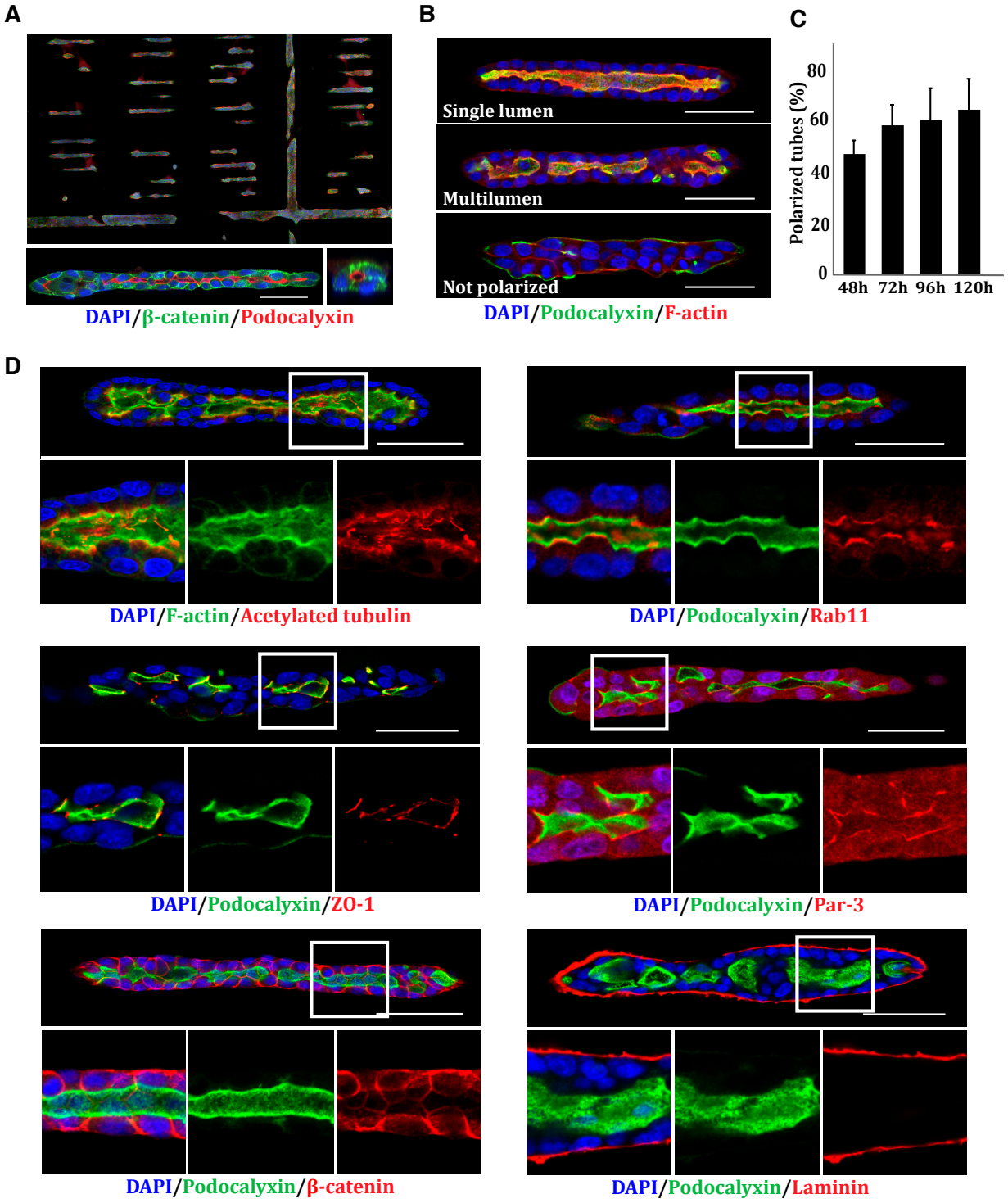

Figure R15. Apicobasal polarity in MDCK tubes (A) Tile-scan of MDCK tubes growing on CYTOO chips (upper). Magnification of a tube (lower left) and yz view of the tube (lower right). **(B)** Distinct polarisation in MDCK tubes. Tubes can have a single opened lumen (single lumen), more than one lumen (multilumen) or do not form lumens (not polarised). Scale bar, 50µm. **(C)** Quantification shows the percentage of polarised tubes over time. Values are mean ±SD from 3 different experiments (n>50 tubes/condition). **(D)** MDCK tubes from 72h stained with different polarity markers. Scale bar, 50µm.

By staining with known polarity markers, we could further depict the organisation and morphology of the tubes (Figure 15D). Podxl stained the apical membrane where primary cilia were labelled with acetylated tubulin while Rab11 marker for recycling endosomes localised to the subapical

endosomal compartment. Par3 and ZO-1 localised to the apical domain but concentrated at the tight junctions. The AJs protein β-cat localised to the lateral membrane and laminin surrounded the tubes localising to the basal membrane (Figure R15.D). The distribution of these polarity markers showed that the tubes growing on micropatterns are properly polarised in the apicobasal axis.

II.I Control of tube morphogenesis by pattern shape

We designed a device in which we printed lines with different widths, lengths and adhesive configurations on glass coverslips through photopatterning techniques (Figure R2). The design of the micropattern, allowed us to analyse how the adhesive area is influencing tube morphology, apicobasal polarity and organisation.

Regarding the different adhesive configurations (Figure R16.A), we analysed how the seven distinct shapes could influence tube formation and single lumen phenotype. As observed, all the configurations allowed the arrangement into 3D structures and the formation of luminal cavities upon addition of MG (Figure R16.B). However, no evident effect in the rate of single lumen formation was observed (Figure R16.C), showing that all seven configurations can direct successful tube formation.

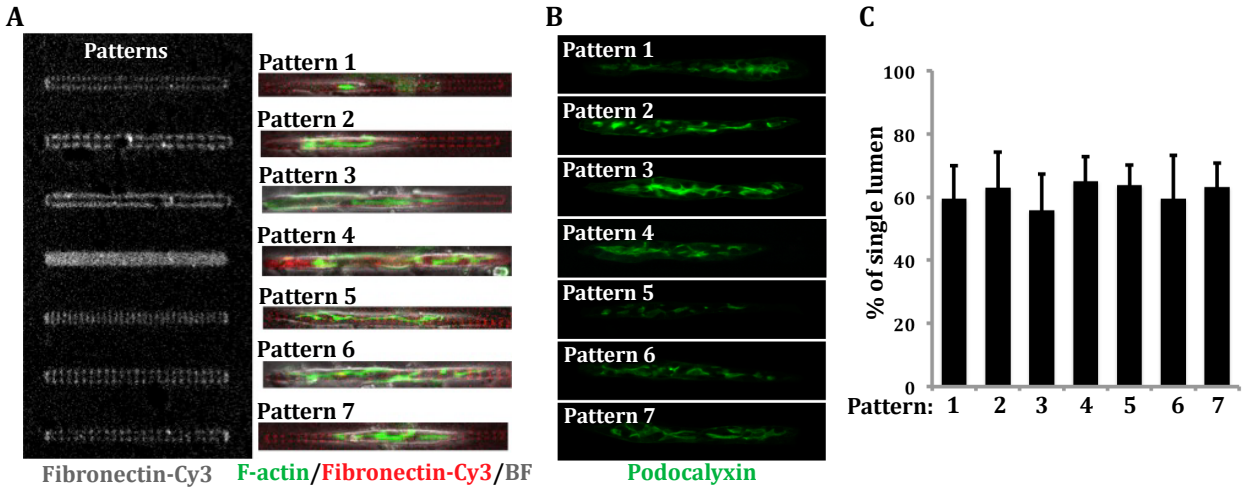

Figure R16. Pattern adhesive configuration in MDCK tubulogenesis (A) MDCK tubes growing on different pattern configuration. Pattern configurations are visualize by fibronectin-Cy3 (right) **(B)** Examples of tubes growing on the different configurations. **(C)** Quantification shows the percentage of single lumen tubes growing on the different pattern configurations. Values are mean ±SD from 3 different experiments (n>80 tubes/configuration).

Using these micropatterns, we also assessed how the line dimensions affected tube formation and found that hollowed tubes could form in all the different pattern sizes (Figure R17.A). We observed that in shorter patterns (100μm), a higher percentage of single lumens formed when compared to 200μm and 300μm tubes, where a gradual decrease in single lumen-tubes could be observed. The width of the patterns did have a slight influence on single lumen formation that was more evident in longer patterns (Figure R17.B). Interestingly, wider patterns allowed the formation of adjacent

lumens in the *y*-axis, what could account for the slight reduction in single lumen formation observed in 30µm patterns (Figures R17.A-B). Besides, pattern width was also influencing the enlargement of the lumens as tubes growing on narrow patterns could form higher lumens while tubes growing on wider patterns are less high but more wide (Figure R17.C-D). Similarly, the number of cells that can fit in a *y*-section of the basal part of the tubes did also depend on the width of the patterns, with number of cells positively correlating with the width of the pattern (Figure R17. E-F) At the same time, this might explain the differences in the shape of the lumens as a higher number of cells in the basal part of the tube in 30µm patterns would be translated in a higher surface of apical membrane in the basal layer. And the contrary would be true for narrower patterns, less cells would induce the formation of thinner lumens and, at the same time, tall lumens are also be favoured by the fact that cells would only be able to grow on the Z-axis as they do not attach outside of the patterns.

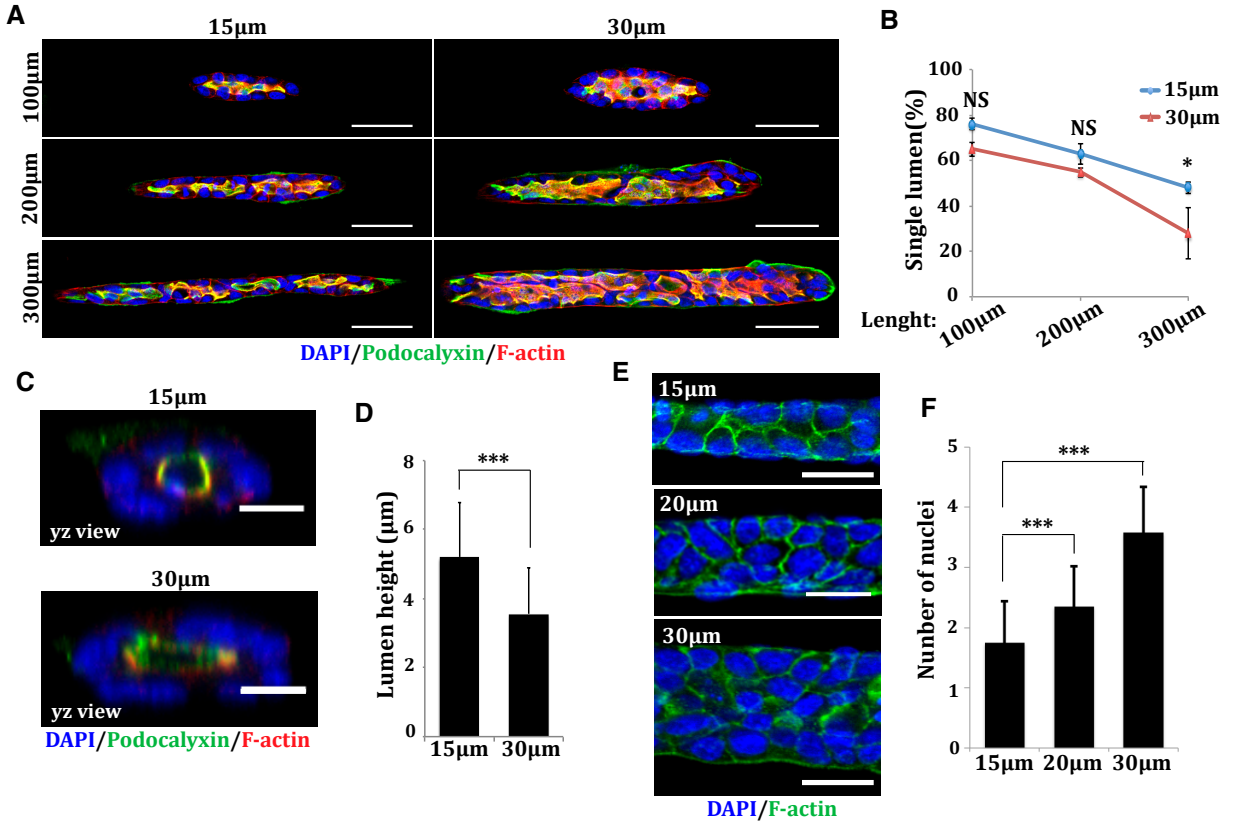

Figure R17. Patterns sizes in MDCK tubulogenesis (A) Tubes of MDCK cells growing on different pattern widths and lengths coated with fibronectin. Scale bar, 50µm. **(B)** Quantification shows the percentage of single lumen tubes depending on the width and the shape of the patterns. Values are mean ±SD from 3 different experiments (n>25 tubes/condition; NS, P>0,05; *, P<0,05). **(C)** yz sections of tubes growing either in patterns of 15µm or 30µm in width. Scale bar, 10µm. **(D)** Quantification shows the height of the lumens of tubes growing on 15µm and 30µm patterns. Values are mean ±SD from 2 different experiments (n>30 tubes/condition; ***, P<0,001). **(E)** Tubes of MDCK cells growing on 15µm, 20µm and 30µm-width patterns. Scale bar, 20µm. **(F)** Quantification shows the number of nuclei in the basal part of tubes growing on 15µm, 20µm and 30µm-width patterns. Values are mean ±SD from 2 different experiments (n>30 tubes/condition; ***, P<0,001).

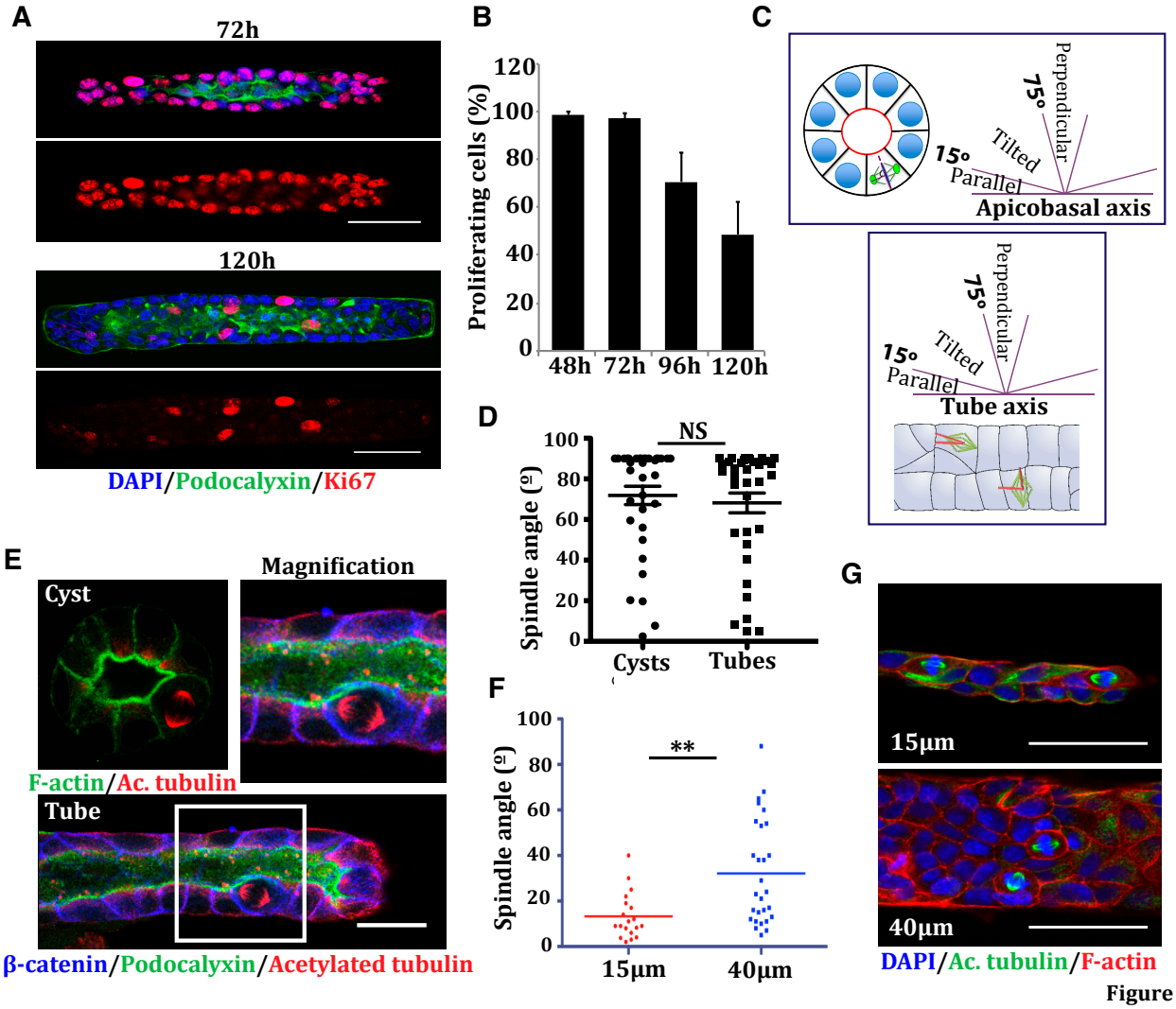

Figure R18. Control of cell division in micropatterns (A) MDCK tubes growing for 72h or 120h in fibronectin-coated patterns. Scale bar, 50µm. **(B)** Quantification shows the percentage of cells positive for Ki67 in tubes at different time-points. Values are mean ±SD from 3 different experiments (n>30 tubes/condition). **(C)** Schematic representation of the measure of spindle angle with the apicobasal axis (upper) and with the tube axis (lower) **(D)** Quantification shows spindle angles with the apicobasal axis in cysts and tubes. Values are mean ±SD from two different experiments (n>30 spindles/experiment; NS, P>0,05). **(E)** MDCK cells growing in MG (cyst) or in micropatterns (tube). Note that spindles are perpendicular to the apicobasal axis. Scale bar, 20µm. **(F)** Quantification shows spindle angles with the tube axis in cells growing on patterns of 15µm and 40µm in width. Values are mean ±SD from two different experiments (n>30 spindles/experiment; **, P<0,01). **(G)** MDCK tubes growing on 15µm, and 40µm-width patterns. Note that spindles are parallel to the tube axis in narrow patterns. Scale bar, 50µm,

During the first days in culture, MDCK cells have a very high proliferative rate (visualised by Ki67). When growing as monolayers, proliferation is controlled by contact inhibition and cell cycle is arrested when the monolayer reaches confluency [161, 230, 231]. In micropatterns, proliferation was also high at the initial stages but started to decrease by the fourth day in culture (Figure R18.A-B), indicating that the physical restriction of cell adhesion provided by the micropatterns allowed the modulation cell proliferation by contact inhibition. We next investigated how the micropatterns can be influencing spindle orientation both in the apicobasal axis an in the tube axis. (Figure R18.C). MDCK cysts have been extensively used to study the mechanisms controlling spindle orientation in the apicobasal axis, a process that is tightly linked to the organisation of epithelial tissues and

contributes to tube growth and homeostasis [232]. Indeed, it is widely known that cell polarity proteins and microtubule modulators control spindle orientation perpendicular to the apicobasal axis [80]. We wondered whether the additional external cues provided by the micropatterns in terms of restriction of cell adhesion would either disrupt or favour spindle orientation perpendicular to the polarity axis. However, by measuring spindle angles with the apicobasal axis both in MDCK cyst and MDCK micropatterns, we found that no differences in spindle orientation exist and that most cells divided in a perpendicular orientation (Figure R18.D-E). This indicates that spindle orientation in the apicobasal axis is not controlled by additional physical determinants provided by micropatterns but through the already known mechanisms. Additionally, spindle orientation of cells within a growing tissue is also highly regulated by physical shaping forces [233]. In our case, we found that spindle orientation in the tube x-axis was controlled by the width of the pattern as when cells grew in a narrow pattern the mitotic spindle oriented parallel to the tube axis (Figure R19.F). This was likely because pattern width did also influence cell shape, causing its elongation in the tube axis (Figure R19.G) and, very likely, changing the force balance. This is consistent with previous reports linking elongation of a tissue with cell division in the same direction to dissipate tensional stress [171, 234].

II.I Influence of ECM composition in tube morphology

Many different substances can be used to coat micropatterns such as cytoskeletal and adhesion proteins among others [235-237]. In our case, as MDCK cells have the capacity to recognise and adhere to various ECM proteins laminin [238-240] collagen-I, fibronectin and laminin when optimising micropatterning procedure We found that cells were able to form tubes in these three conditions (Figure R8.A, R9.B and R11.E). Despite this fact, all the experiments performed with MDCK tubes were done on fibronectin-coated micropatterns in search of simplicity.

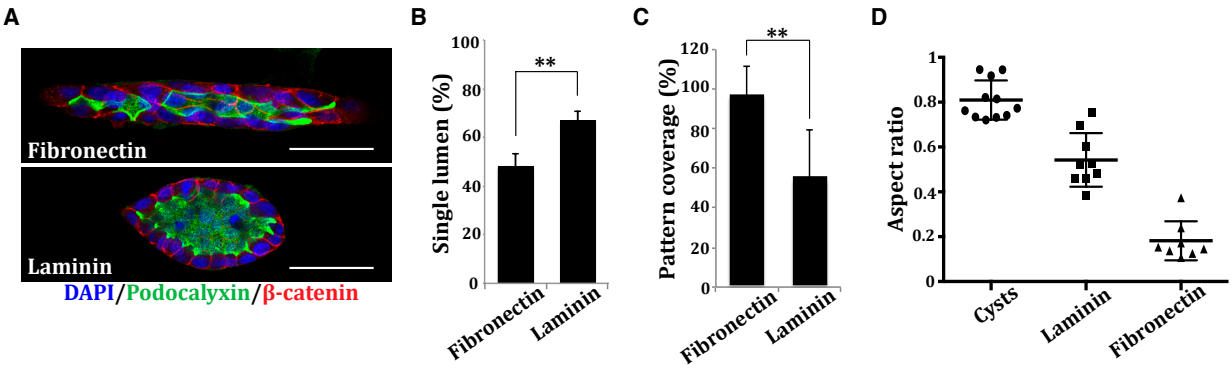

Figure R19. Tubes in micropatterns show different morphologies depending on the ECM coating (A) MDCK tubes growing on fibronectin- and laminin-coated patterns. Scale bar, 50µm. **(B)** Quantification shows the percentage of tubes with a single lumen. Values are mean ±SD from 3 different experiments (n>100 tubes/experiment; **, P<0,01). **(C)** Quantification shows the percentage of a pattern covered by tube cells. Values are mean ±SD from 3 different experiments (n>20 tubes/experiment; **, P<0,01). **(D)** Quantification shows aspect ratio of lumens in MDCK cyst and tubes. Values are mean ±SD from 2 different experiments (n>30 spindles/experiment).

However, striking differences in tube morphology were observed depending on the ECM component used for pattern coating (Figure R19.A). When comparing tubes on fibronectin- and laminin-coated patterns, we saw that laminin tubes presented a higher rate of single lumen formation (Figure R19.B). At the same time, patterns coverage of fibronectin tubes was higher than that of laminin tubes (Figure R19.C). This last observation could explain why laminin tubes had a higher percentage of single lumen, as the reduction in pattern coverage accounts for the decrease in tube length what, as shown before, is also influencing the rate tubes with a single lumen tubes (Figure 17.B). By measuring the width/length ratio (aspect ratio) of lumens in fibronectin and laminin tubes, we could get an estimation of the circularity of the lumens. We saw that while the aspect ratio of fibronectin tubes was close to 0, like most physiological tubes, the aspect ratio of laminin tubes was around 0.5. This value was in between the aspect ratio of a cyst and a physiological tube (Figure R19.D). Due to these morphologies, the majority of the characterisation, morphogenesis and nephrotoxicity experiments were done on fibronectin-coated micropatterns.

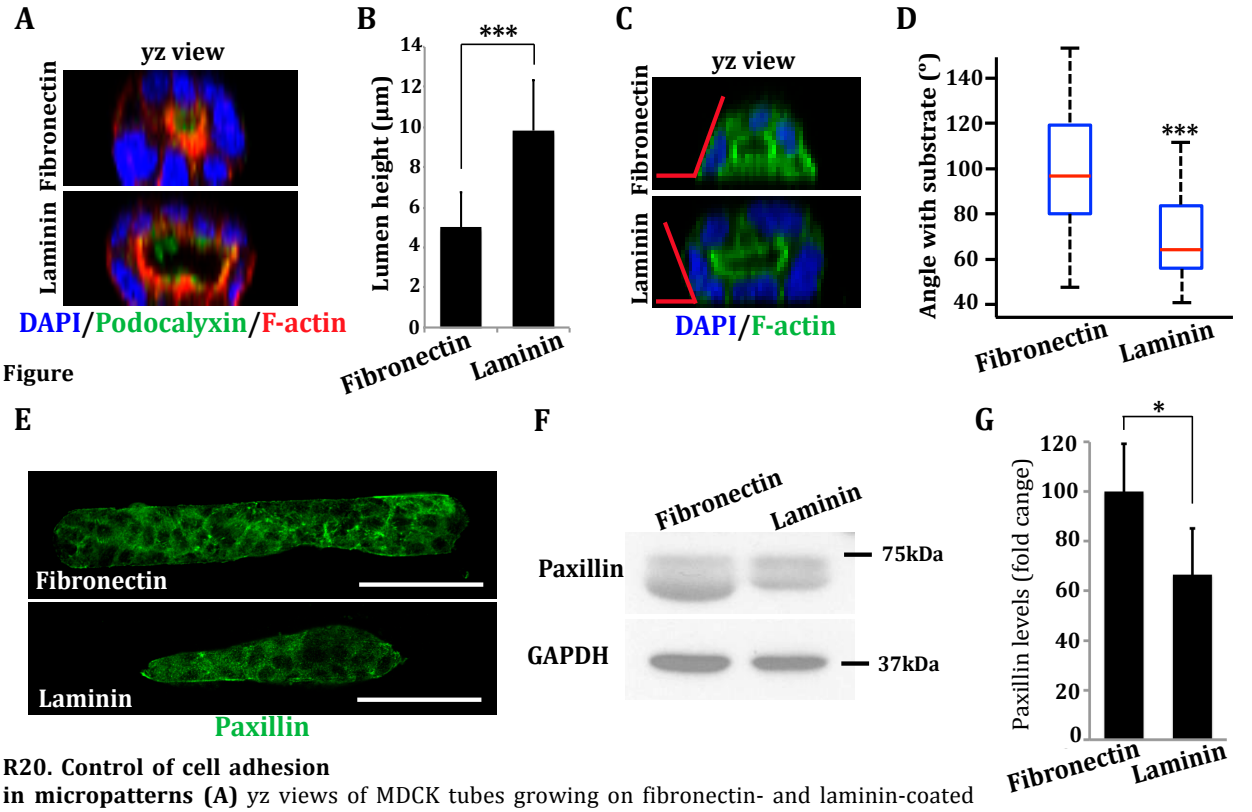

R20. Control of cell adhesion in micropatterns (A) yz views of MDCK tubes growing on fibronectin- and laminin-coated patterns. Note, lumens have different sizes **(B)** Quantification shows the lumen height measuring the top-bottom diameter of the lumen in cross-sections of tubes growing in fibronectin or laminin respectively. Values are mean ±SD from 3 different experiments (n>50 tubes/experiment; ***, P<0,001). **(C)** yz views of MDCK tubes growing on fibronectin- and laminin-coated micropatterns. Red lines show the angle between the substrate and the tube wall **(D)** Quantification shows the angles with the substrate measured for tubes growing on fibronectin and laminin. Values are mean ±SD from 3 different experiments (n>30 tubes/experiment; ***, P<0,001). **(E)** MDCK tubes growing on fibronectin- and laminin-coated micropatterns. **(F)** Immunoblot showing Paxillin protein levels in MDCK cells growing on fibronectin- and laminin-coated patterns. **(G)** Quantification of the immunoblot shows Paxillin fold-change protein levels. Values are mean ±SD from 3 different experiments (*, P<0,05).

We further depicted the differences regarding lumen dimensions by analysing cross-sections of tubes growing on fibronectin- and laminin-coated patterns. We observed that laminin lumens were taller than fibronectin ones (Figure R20.A-B) and that the angle measured between the tube wall and the substrate (Figure R20-C) was higher in fibronectin- than in laminin-tubes (Figure R20.D) suggesting that the adhesion force should be higher in fibronectin substrates. We immunostained tubes of cells growing on different ECM-coated patterns to visualise the FAs protein paxillin and found that bigger paxillin clusters form in the basal part of tubes growing on fibronectin (Figure R20.E). Paxillin protein levels are also increased in tubes on fibronectin patterns (Figure R20.F-G), indicating that basal adhesion is increased in this case.

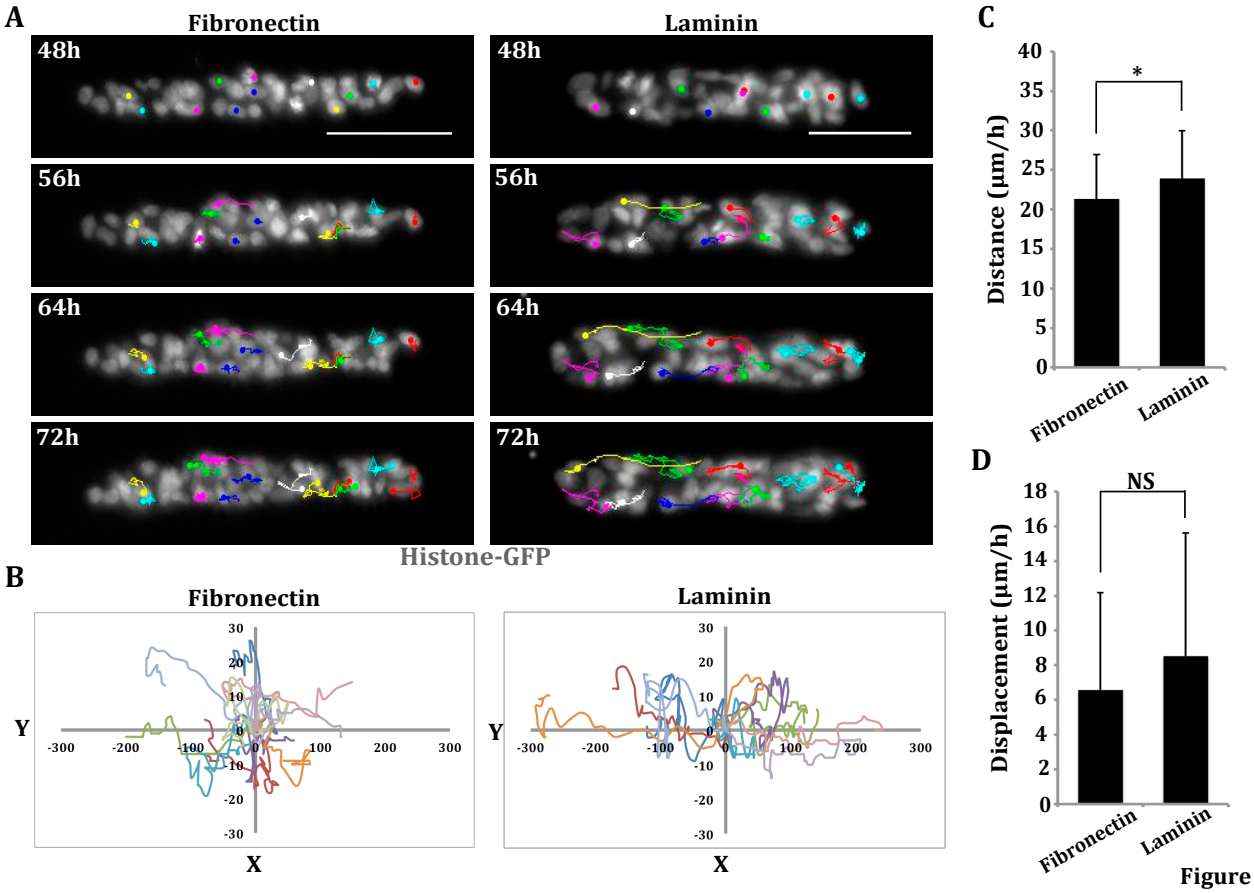

R21. Control of cell adhesion in micropatterns (A) Still-images from time-lapse experiments of MDCK tubes growing in fibronectin- and laminin-coated patterns. Coloured lines indicate the path of nuclei over time and dots indicate the position of a given cell in a particular frame. Scale bar, 50µm **(B)** Representation of the path followed by ten random cells, each line represents the route of a cell. **(C)** Quantification shows the average distance travelled by a cell per hour either on fibronectin or laminin. Values are mean ±SD from 3 different experiments (n>100 cells/experiment; *, P<0,05) **(D)** Quantification shows the average displacement travelled by a cell per hour either on fibronectin or laminin-coated patterns. Values are mean ±SD from 3 different experiments (n>100 cells/experiment; NS, P>0,05).

Next, we investigated how this differences in cell adhesion impacted in the migratory capacity of MDCK cells growing on fibronectin- or on laminin-coated micropatterns. First we analysed cell migration by using a stable cell line expressing Histone-GFP. This cell line allowed us to track nuclei movement in time-lapse images to obtain data regarding the position of each cell at a given time point (Figure R21.A). Representing the coordinates of cells in a graph, we could see that cells

growing in laminin have slightly longer paths than cells growing in fibronectin (Figure R21.B). This observation was confirmed by analysing the migratory distances of cells growing on laminin and fibronectin: a statistical significant result was obtained showing that cells growing on laminin can migrate higher distances per hour compared to cells growing on fibronectin (Figure R21.C). However, no differences in cell displacement were observed (Figure R21.D). While controversial, this last result might be explained by the fact that although laminin cells migrate faster, as laminin tubes are shorter because they occupy a lower percentage of the pattern shape (Figure R19.C), the area through which cells can migrate is more limited.

Many studies have shown that dynamic changes in cell adhesion, shape and migration are the major driving forces sculpting tissue architecture and function *in vivo*. Over the last decade, it has become increasingly evident that many of these processes are modulated by chemical, physical, and topographical cues provided by the cellular microenvironment [169, 241]. Among them, the ECM is a key regulator of developmental dynamics because it is a major component of the cellular microenvironment [238, 242]. Consistent with this, we have demonstrated that MDCK tubular architecture in micropatterns is finely controlled by the extracellular matrix components laminin and fibronectin, which are in turn regulating the adhesive and migratory properties of these cells. Furthermore, the role of the ECM in controlling the organisation of the apical domain in epithelial cells has been demonstrated by several pieces of evidence showing that basal adhesion signals are the main drivers of epithelial polarisation and differentiation [65]. Polarity orientation in the case of MDCK cysts is dependent on laminin binding by β1 integrin and activity of the small GTPase Rac1 to trigger the first steps of a polarisation [243]. In our model, as laminin is the main protein component of the MG that is surrounding the exposed regions of the tubular structure, both laminin- and fibronectin-coated tubes can polarise properly. However, the basal part of the tube is accounting for the main differences observed between laminin and fibronectin tubes. Although initial studies regarding cell adhesion depending on ECM components showed that rat liver epithelial cells spread better on laminin substrates compared to fibronectin [240], a very different phenotype was demonstrated in micropatterns. Work from our group showed that cell spreading of MDCK cells growing on laminin substrates is lower than when growing on collagen-I coated matrices [87]. This work shows that cells growing on laminin, round-up and lumen formation is facilitated by the lower actomyosin contractility acquired in this condition compared to cells growing on collagen. Consistent with this work, we have seen that cells growing on laminin do not cover the whole pattern while cells on fibronectin adhere to the whole adhesive pattern. This phenotype is likely due to different adhesive dynamics of MDCK, very likely due to the variety of integrins expressed in MDCK and its interaction with the ECM components and the assembly of FAs. As FAs link the ECM proteins with the actomyosin cytoskeleton, cell movement and remodelling

dependent on contractility may also be disturbed as seen by slight differences in cell motility of cells growing on laminin- and fibronectin-coated patterns.

II.II Influence of matrix stiffness in tube formation

The biomechanical properties of a tissue in terms of stiffness vary markedly between organs and tissues and are inherently related to tissue function. At the same time, matrix stiffness is also important for many morphogenetic events as well as for the development of pathological conditions [150, 244]. Recent advances expose a novel and remarkable complexity in extracellular control of epithelial morphogenesis [238]. Mechanical properties such as matrix stiffness and cell confinement are emerging as key regulators of epithelial behaviour, modulating cytoskeletal dynamics, which transduce into nuclear signals that regulate differentiation [87, 198, 245].

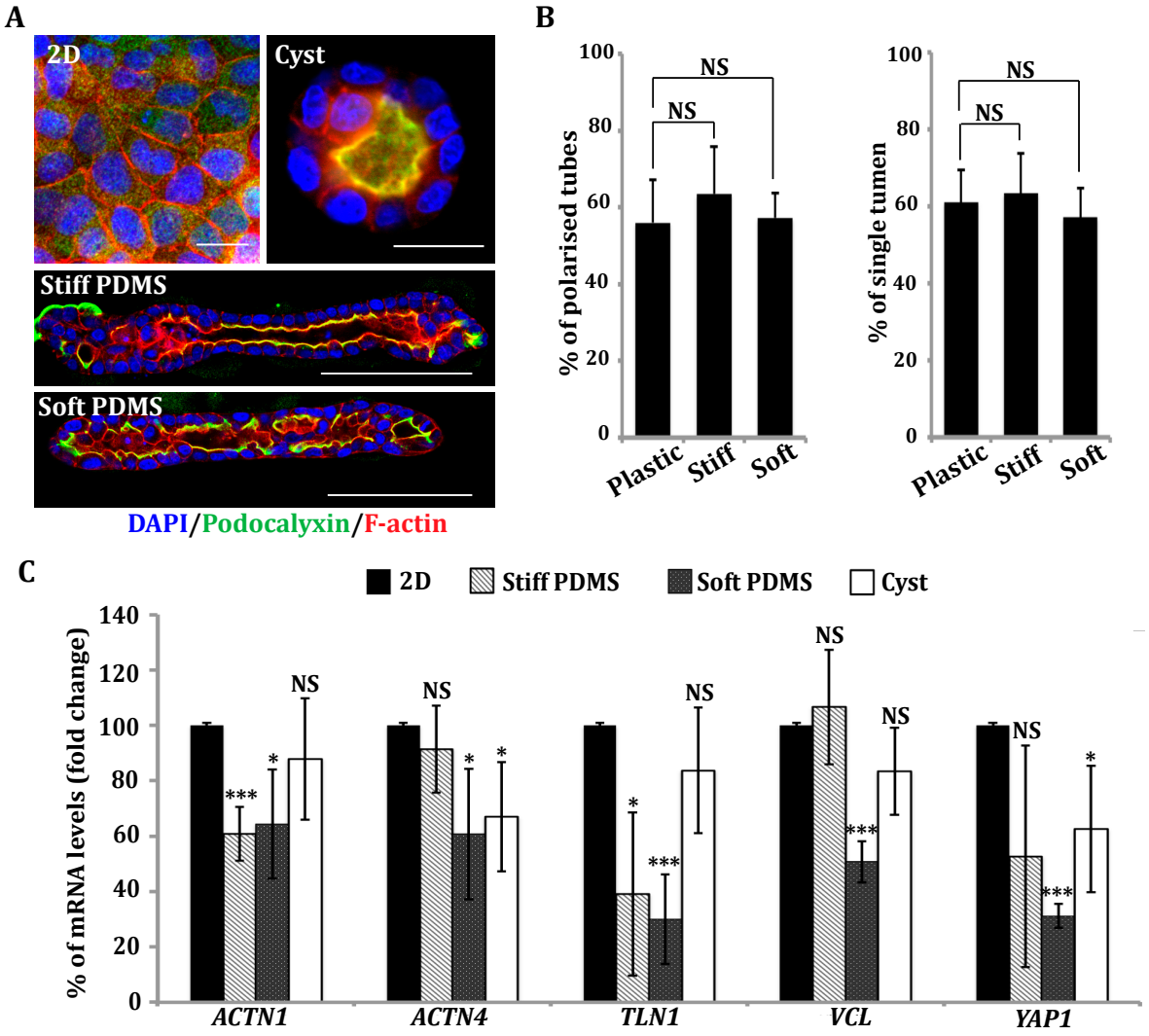

Figure R22. Culture of MDCK tubes on matrices with different stiffness (A) MDCK cells growing in 2D (upper left), in a MG substrate as cysts (upper right) and as tubes on stiff PDMS and soft PDMS (lower). Scale bar in 2D and cyst images, 20μm. Scale bar in tube images, 50μm. **(B)** Quantification shows the percentage of polarised tubes (left) and the percentage of single lumen (right) respectively of tubes growing on different stiffness. Values are mean ±SD from 3 different experiments (n>100 tubes/experiment; NS, P>0,05). **(C)** Quantification shows the mRNA levels (%) of different mechanosensitive proteins in cells growing on substrates of different stiffness relative to 2D conditions. Values are mean ±SD from 4 different experiments. NS, P>0,05; *, P<0,05; ***, P<0,001).

Cells can sense matrix stiffness through FA complexes [134] and signal through mechanotransduction processes giving rise to many different cellular responses like the modulation of cell migration [246], cell differentiation [247] and the onset of metastatic processes [30, 248]. By using μCP techniques instead of photopatterning, and combining this with the use of silicones with different Young's Moduli, we were able to fabricate micropatterns with different substrate stiffness that allowed us to analyse the contribution of this physical property in the formation of epithelial tubes (Figure R22.A). We did not find any remarkable morphological difference between tubes growing on substrates in plastic, stiff and soft PDMS regarding to polarisation (Figure R22.B). Probably, this is due to the anisotropy of the system, with only the basal part of the tube in contact with the plastic/PDMS substrate. However, by Real-time PCR (qPCR), we discovered that the expression levels of FAs proteins and other proteins known to be involved in mechanotransduction pathways varied significantly between different rigidity conditions, specially when comparing cells growing as tubes on soft PDMS with cells growing as a monolayer (Figure R22.C). Consistently, a recent work links the transcription and assembly of FAs to YAP response to matrix stiffness [143], what can explain the results observed in our system.

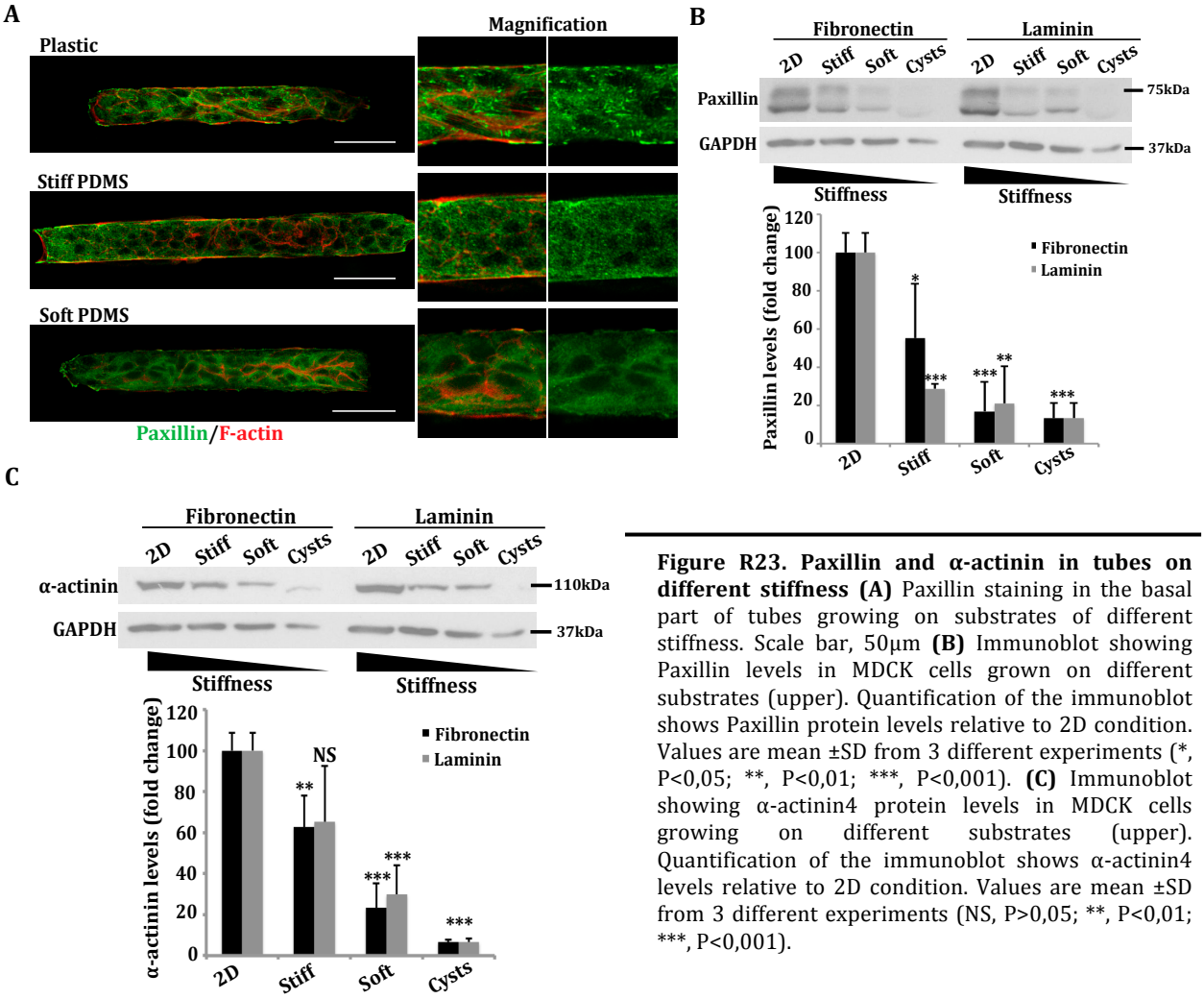

Figure R23. Paxillin and α-actinin in tubes on different stiffness (A) Paxillin staining in the basal part of tubes growing on substrates of different stiffness. Scale bar, 50μm **(B)** Immunoblot showing Paxillin levels in MDCK cells grown on different substrates (upper). Quantification of the immunoblot shows Paxillin protein levels relative to 2D condition. Values are mean ±SD from 3 different experiments (*, P<0,05; **, P<0,01; ***, P<0,001). **(C)** Immunoblot showing α-actinin4 protein levels in MDCK cells growing on different substrates (upper). Quantification of the immunoblot shows α-actinin4 levels relative to 2D condition. Values are mean ±SD from 3 different experiments (NS, P>0,05; **, P<0,01; ***, P<0,001).

Next, we analysed the effect of matrix rigidity in the expression and distribution of FA proteins and other proteins known to respond to matrix stiffness. Particularly, we observed important changes in the distribution of these proteins at the focal adhesion level (basal part of the tubes) in substrates with different stiffness. Cells form large clusters of paxillin on plastic micropatterns (Young's Modulus around ~1400MPa) while cells present more diffused distribution protein in stiff PDMS tubes (~2MPa) and in soft PDMS tubes (~0.9MPa) (Figure R23.B). Concomitantly, the amount of total paxillin protein level decreased with the stiffness of the matrices (Figure R23.B). Similarly, the protein levels of the actin crosslinker α-actinin were also lower in softer substrates (Figure R23.C). This is consistentt with the fact that assembly of FAs is force-dependent and they tend to form mechanotransduction clutches [142].

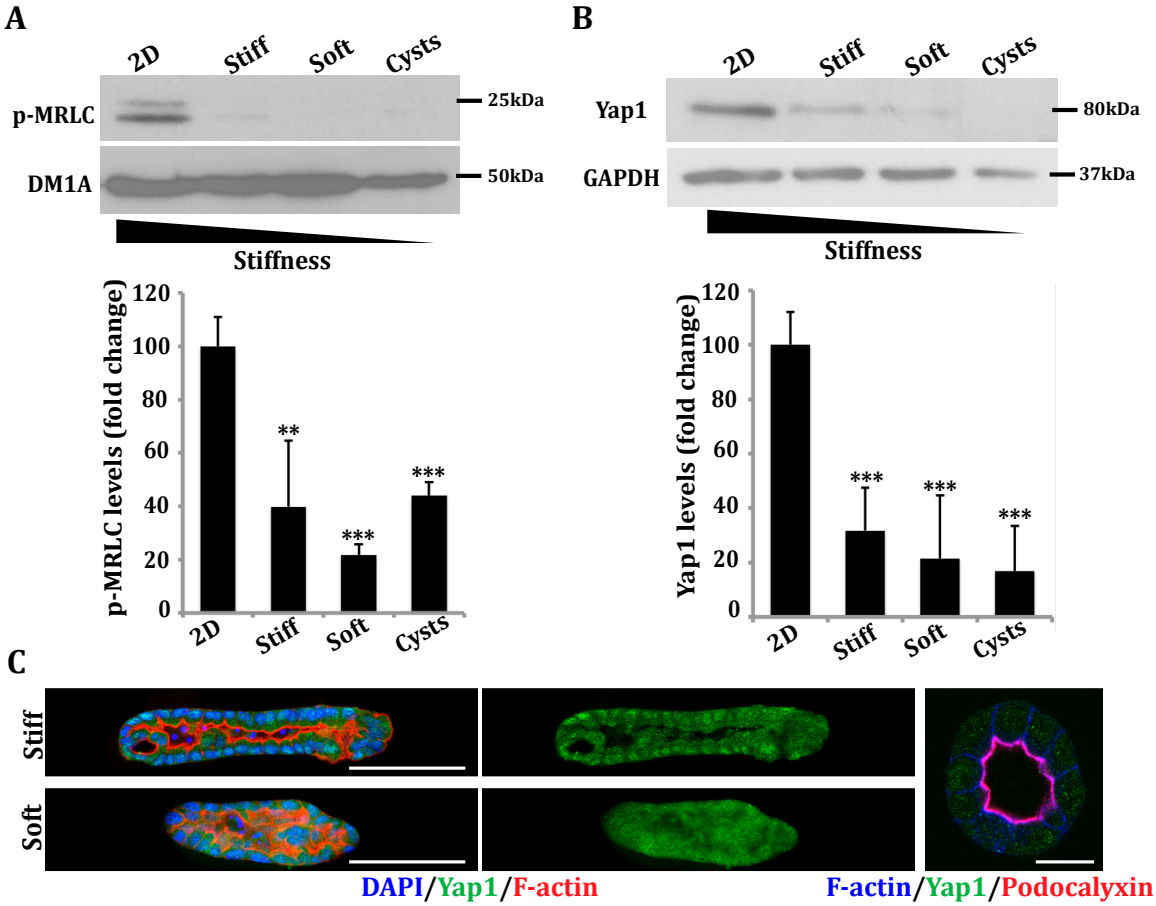

R24. P-MRLC and Yap1 in tubes on different stiffness (A) Immunoblot showing p-MRLC levels in MDCK cells grown on different substrates (upper). Quantification of the immunoblot (lower) shows p-MRLC protein levels relative to 2D condition. Values are mean ±SD from 3 different experiments (*, P<0,05; **, P<0,01; ***, P<0,001). **(B)** Immunoblot showing Yap1 protein levels in MDCK cells grown on different substrates (upper). Quantification of the immunoblot (lower) shows YAP1 levels relative to 2D condition. Values are mean ±SD from 3 different experiments (NS, P>0,05; **, P<0,01; ***, P<0,001). **(C)** Yap1 staining in tubes formed on substrates of different stiffness (left) and in cysts (right). Scale bar tubes, 100µm. Scale bar cyst, 100µm.

It has been demonstrated that substrate stiffness can control YAP localisation through processes that are downstream of actomyosin contractility [245]. YAP localises to the nucleus in stiffer substrates while being more diffuse in the cytoplasm when the stiffness lowers [140]. We found that phospho-myosin regulatory light chain (p-MRLC) levels decreased in softer substrates (Figure

R24.A), indicating that cell contractility is reduced in compliant gels as previously reported [249]. Parallel, YAP levels are also reduced in softer substrates, a result that can be explained either by the degradation of YAP in the cytoplasm [250] or by a decrease in *YAP* transcription in response to matrix stiffness (Figure R24.B). Probably, a combination of both events is responsible for this reduction, as the transcription levels alone could hardly explain the drastic reduction in the protein levels. Consistent with this, YAP localised to the nucleus at a greater extent when cells were grown on stiff substrates, such as plastic, while a more cytoplasmic distribution of YAP could be seen in softer silicone substrates or MG (Figure R24.B). Altogether, we show that our micropattern-based model system is useful to monitor the morphological responses to environmental cues occurring during tubulogenesis.

III. MICROPATTERNING AS A TOOL TO STUDY LUMEN COALESCENCE

How lumen coalescence is controlled and achieved at a molecular level is not completely elucidated yet. With our system, we have demonstrated that tubule formation *in vitro* follows the same steps observed *in vivo* by time-lapse microscopy [26]. When MDCK cells are grown on micropatterns to form tubes, they initially generate multiple small lumens, which expand and resolve by fusing with each other to form one single lumen, similarly to the mechanisms of the intestine and vasculature formation in zebrafish (Figure R.14). Therefore, our *in vitro* model provides a very powerful tool to study this issue.

III.I Influence of planar cell polarity in lumen coalescence

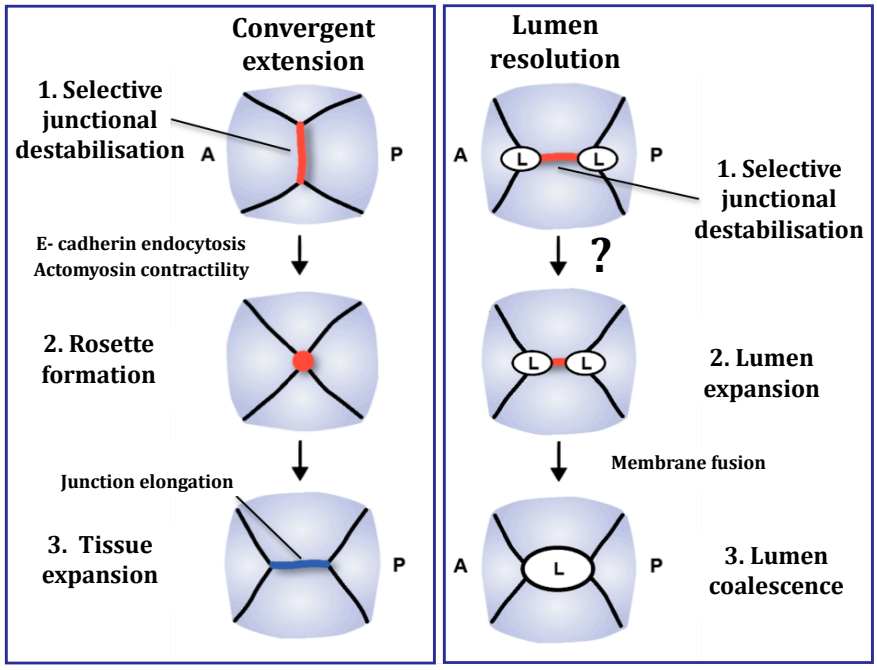

Figure R25. Principles of convergent extension and lumen resolution. The event of convergent extension involves the guided shrinking of cell-cell junction and its later expansion in a direction perpendicular to the initial one to attain tissue elongation. This targeted cellular process, involving E-cadherin endocytosis and altered actomyosin contractility among others, is controlled by PCP machinery. We hypothesised that the process of lumen resolution is similarly controlled by PCP effectors as it also involves the remodelling of targeted cell junctions. A: anterior; P: posterior; L: lumen.

It has recently been shown that epithelial cells within the tubules achieve a precise orientation and elongate medio-laterally, inferring the possibility that this process results in cellular intercalation [251] which is a similar process to convergent extension movements [4], which are known to cause narrowing and elongation of tissues in several systems during morphogenesis. CE relies on planar cell polarity (PCP) [126, 128, 251, 252], which is perpendicular to apicobasal polarity and controls asymmetric distribution of proteins and features through an epithelial sheet during development. In cord hollowing process, lumen resolution occurs through both apical membrane expansion and, more importantly, junctional remodelling. The process of junctional remodelling closely resembles convergent extension movements as it involves the disassembly of a targeted cell junction to generate cellular rearrangements (Figure R25). For this reason, we proposed that PCP controls lumen coalescence and that tubular 3D structures grown on micropatterns could become a very potent model to study planar cell polarity *in vitro*, due to the fact that this micropattern model emulates the cellular distribution of a tubular epithelial sheet. To test this hypothesis, we performed a transcriptomic expression analysis of most of PCP-related proteins in MDCK and LLC-PK1 cells grown on micropatterns compared to cells grown as monolayers to identify PCP genes that are expressed in these cell lines and, more importantly, are induced during tubulogenesis. Interestingly, we identified a number of PCP genes that were induced in 3D tubulogenesis in micropatterns including both global and core modules of PCP (Figure R26). These results suggested that PCP signalling might play a role in tube formation.

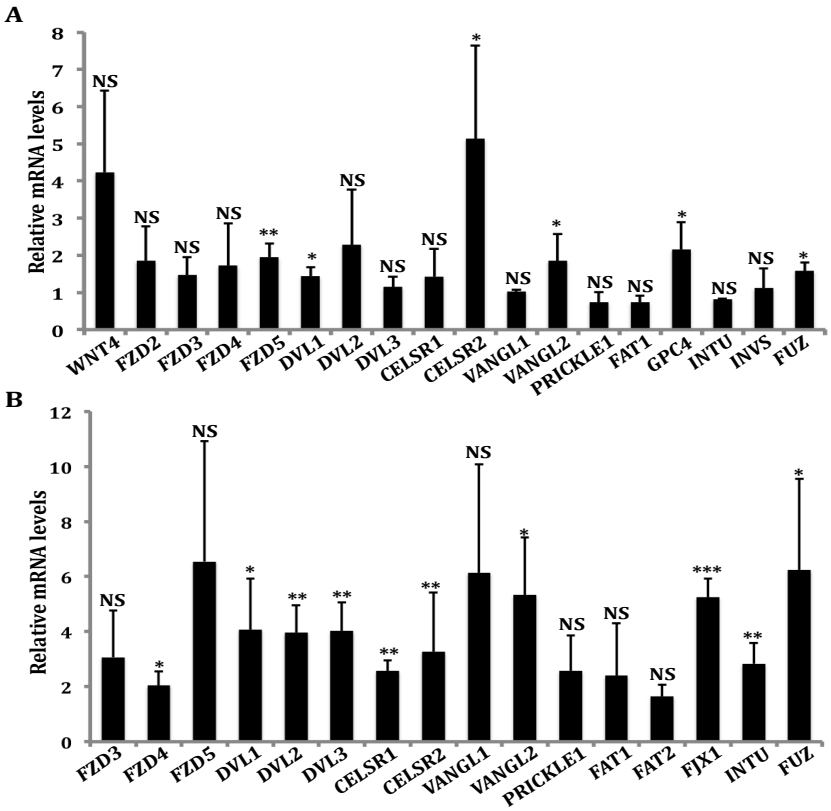

Figure R26. Expression levels of PCP genes in MDCK an LLC-PK1 cells. (A) Quantification shows the mRNA levels of different PCP genes in MDCK cells growing on micropatterns relative to cells growing as epithelial monolayers. Values are mean ±SD from 3 different experiments. (NS, P>0,05; *, P<0,05; **, P<0,01). **(B)** Quantification shows the mRNA levels of different PCP genes in LLC-PK1 cells growing in 3D as micropatterns relative to cells growing in a 2D configuration. Values are mean ±SD from 3 different experiments. (NS, P>0,05; *, P<0,05; **, P<0,01; ***, P<0,001;).

We next evaluated the role of PCP proteins in controlling junctional remodelling during lumen resolution. We selected specific PCP genes that were induced in micropatterns and used small interfering RNA molecules (siRNAs) against them to knockdown (KD) its expression levels. We designed siRNAs against the PCP effectors Fuzzy (Fuz) and Celsr1 among others (not shown) and, although they were induced at early stages of epithelial morphogenesis (Figure R26), the decrease of its expression levels (Figure R27.B) did not induce any evident morphological alteration (Figure R27.A). We deeper analysed the KD phenotypes and found that the average number of lumens per tube remained constant in the KD tubes compared to the control (Figure R27.C). As the number of lumens is dependent on tube length (Figure R17.B), we quantified the number of lumens depending on the tube length and, again, we found no differences (Figure R27.D). Finally, we concluded that these proteins do not have a role in lumen fusion because we measured the length of the longest lumen in a tube depending on the length of the whole tube and we did not find differences between KD tubes and the control structures. This implies that lumens were able to fuse at an equal rate to that of the control tubes because the length of the lumens formed remained the same. (Figure R27.E).

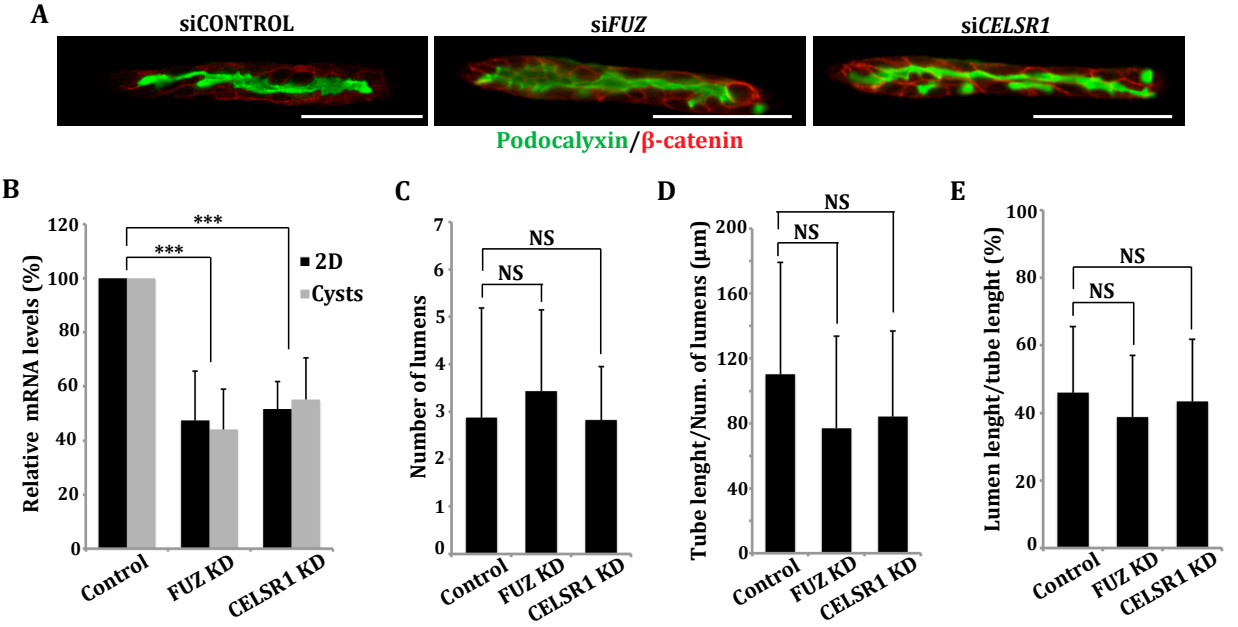

Figure R27. Knockdown of PCP-related genes in MDCK cells growing on micropatterns. (A) MDCK tubes transfected with a control siRNA, siRNA against *FUZ* and siRNA against *CELSR1* respectively. Scale bar, 100µm. **(B)** Quantification shows the mRNA levels of KD genes in MDCK cells KD for *FUZ* or *CELSR1* and growing as monolayers or as cysts relative to control levels. Values are mean ±SD from 3 different experiments. (***, P<0,001). **(C)** Quantification shows the number of lumens in tubes transfected with a control siRNA, siRNA against *FUZ* and siRNA against *CELSR1* respectively. Values are mean ±SD from three different experiments. (n>50 tubes/experiment; NS, P>0,05). **(D)** Quantification shows the lumen length (µm)/number of lumens in tubes transfected with a control siRNA, siRNA against *FUZ* and siRNA against *CELSR1* respectively. Values are mean ±SD from 3 different experiments. (n>50 tubes/experiment; NS, P>0,05). **(E)** Quantification shows the percentage of a tube occupied by the longest lumen in the tube for cells transfected with a control siRNA, siRNA against *FUZ* and siRNA against *CELSR1* respectively. Values are mean ±SD from 3 different experiments. (n>50 tubes/experiment; NS, P>0,05).

These results indicate that a decrease in the levels of PCP genes such as Fuz or Celsr1 do not have a role in lumen coalescence. Given the slight increase in expression levels found in micropatterns

when compared to 2D, we speculate that they might have a role in the first stages of cell polarisation as previous reports have shown that PCP and apicobasal polarity are coupled during development [32-34]. In this sense, though, we did not find any apparent defect in cyst formation when quantifying the formation o a single lumen in MDCK cysts KD for Fuzzy or Celsr1 among others (not shown). Further experiments in this direction should be performed in the future to better understand the intersection of apicobasal and planar cell polarity during morphogenesis.

III.II Influence of actomyosin-driven junction shrinking in lumen coalescence

Convergent extension movements, and particularly mediolateral intercalation, regulate the cytoskeleton dynamics through activation of Rho-GTPases to control cell movements and junction remodelling. Although we did not find a direct effect of PCP in regulating cytoskeleton-driven junction remodelling, we further analysed the actomyosin regulation and its effect on junction shrinking and lumen resolution.

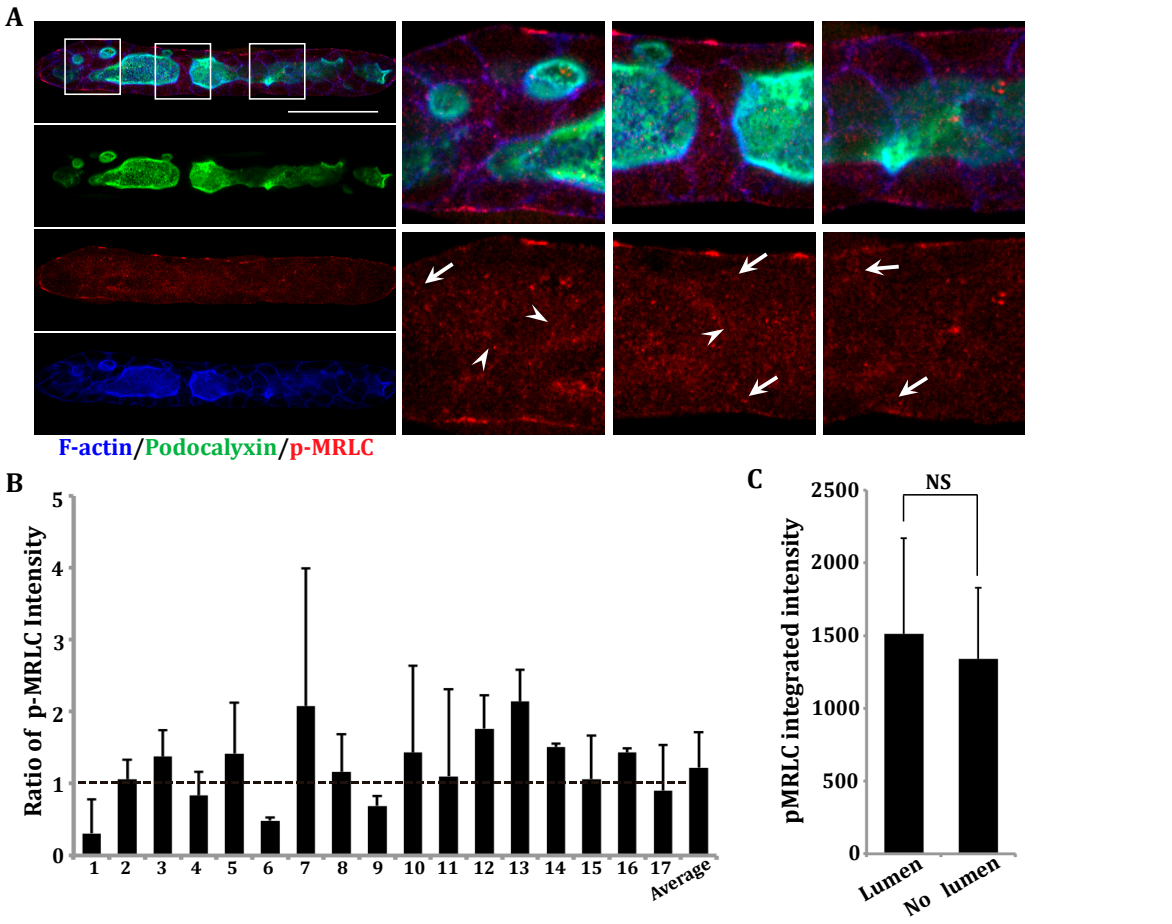

Figure R28. Myosin-dependent contractility in lumen resolution. (A) MDCK tube stained with p-MRLC antibody. Magnifications (right) show regions with cell-cell junctions. Arrowheads indicate the position of cell-cell junctions between lumens. Arrows indicate the position of normal cell-cell junctions. Scale bar, 50µm. **(B)** Quantification shows the ratio of p-MRLC intensity in junctions between lumens/normal junctions of 17 random MDCK tubes. The right value in the x-axis is the average value of the 17 tubes. A discontinuous line shows ratio=1. Values are mean ±SD from 17 different tubes. (n>10 junctions/tube). Note, the ratio of intensity fluctuates between 0 and 2 indicating that there is no clear tendency. **(C)** Quantification shows the p-MRLC integrated intensity of junctions between lumens and normal junctions. Values are mean ±SD from 3 different experiments. (n>25 tubes/experiment; NS, P>0,05).

We analysed the distribution of phospho-Myosin light chain (p-MRLC) in tubes (Figure R28.A) to examine whether it is accumulated in junctions targeted to be remodelled (those between lumens). We found that there is not an asymmetric distribution of p-MRLC indicating that there are no differences regarding actomyosin contractility in these junctions compared to other junctions (Figure R28.B-C). Thus, actomyosin-drive junction shrinking does not seem to explain lumen coalescence in MDCK tubes.

III.III Influence of lumen expansion in lumen coalescence

It has been described that in zebrafish gut and hepatic ducts, fluid filling by paracellular ion transport is necessary for lumen opening and coalescence [22, 253]. For this reason, we wondered whether lumen expansion has a direct effect on lumen coalescence in our *in vitro* system as this expansion would make adjacent lumens to be closer, thus facilitating lumen fusion. To test this hypothesis, we cultured MDCK cysts in different media with varying osmotic concentrations to decrease the fluid efflux into the lumen (Figure R29.A). We found that when culturing MDCK cyst in hyperosmotic conditions, lumen area decreases compared to normal conditions. This lower lumen inflation is translated in a decreased number of cysts with a single lumen (Figure R29.A).

During de *novo lumen* formation, once the apical membranes are formed after cell division, they have to separate to clear the internal space inside the tube. The sialomucin Podxl plays in lumen formation in MDCK cysts [81, 83]. To analyse the contribution of membrane repulsion in lumen coalescence, we transfected MDCK cells with Podxl-GFP to induce the overexpression of this protein (Figure R29.B). We analysed the lumen height of control and transfected cells to infer the approximate size of the lumens and found increased lumen height in Podxl-GFP tubes compared to not-transfected cells. Similarly, transfected cells growing on micropatterns also showed a significant increase in the percentage of single lumen tubes. This result likely correlates with the previous observation regarding the increased lumen size in transfected cells. The higher membrane repulsion observed in this case, is promoting lumen expansion and, as lumens reach a critical size and they are closer, they are more prone to fusion, (Figure R29.B). To broaden our knowledge on the contribution of lumen inflation in lumen coalescence on micropatterns, we deeper investigated the role of paracellular interchange of ions and water through the TJs. Using an electrical cell-substrate impedance system (ECIS) we measure the trans-epithelial resistance of MDCK cells and a subclone of MDCK cells known as T-23. The two cells strains had different trans-epithelial resistance (TER) values as measured by ECIS (Figure R29.C, left). This result indicates that TJs formation and sealing is retarded in T-23 cells resulting in a leaky union and, presumably, an increased paracellular transport. Consistent with this, T-23 tubes presented bigger lumens (Figure R29.C, upper right) and both an increased polarisation rate and a higher percentage of single lumen

tubes compared to MDCK cells (Figure R29.C, lower right). All these observation reinforce the idea that lumen inflation in MDCK tubes has a prominent role in lumen coalescence.

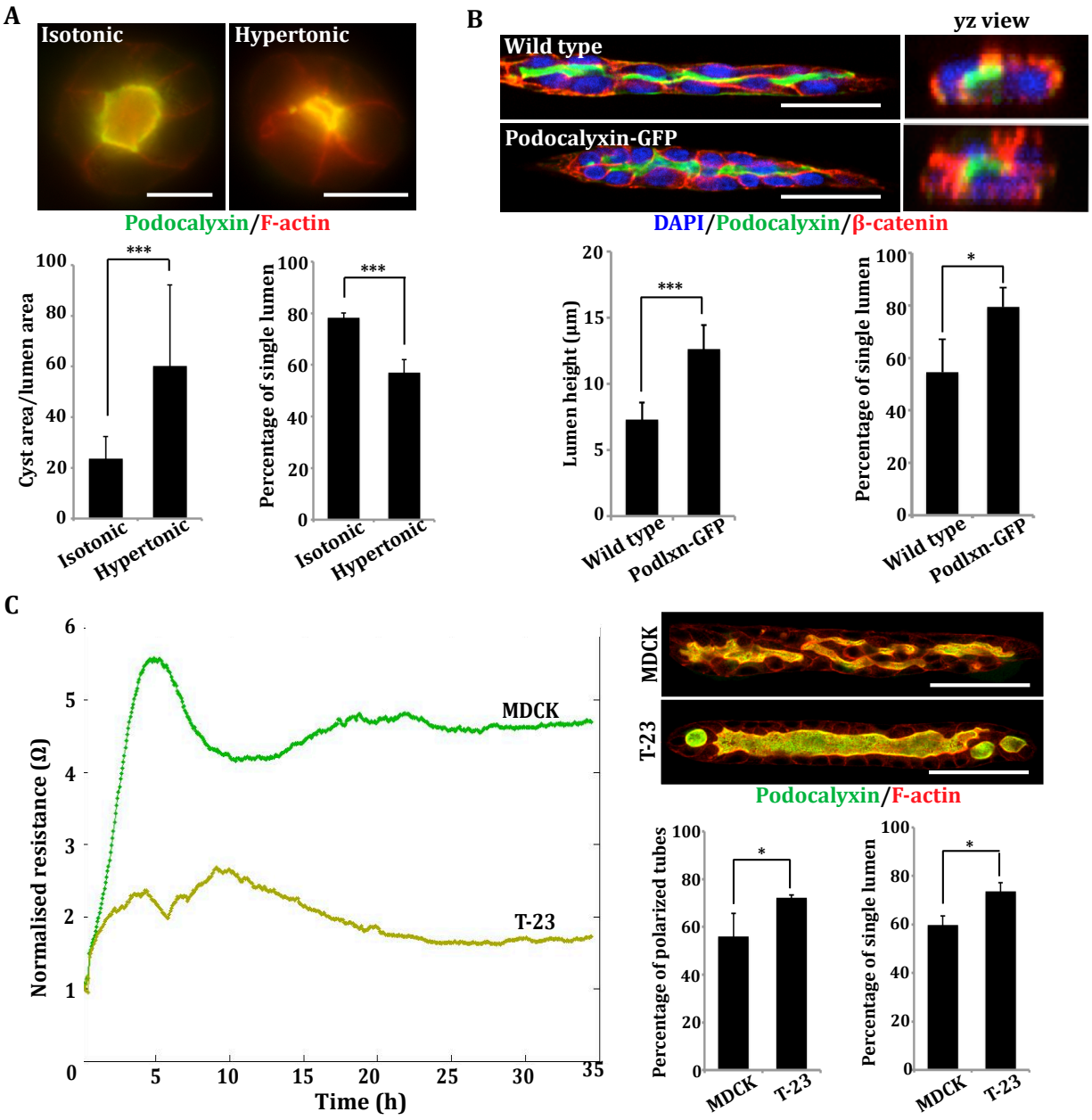

Figure R29. Role of luminal expansion in lumen resolution. (A) MDCK cells forming cysts grown in isotonic and hypertonic media (upper). Scale bar, 20µm. Quantification (lower left) shows the ratio between lumen and cyst area. Values are mean ±SD from 3 different experiments. (n>30 cysts/experiment; ***, P<0,001). Quantification (lower right) shows the percentage of single lumen cysts. Values are mean ±SD from 3 different experiments. (n>100 cysts/experiment; ***, P<0,001). **(B)** MDCK tubes and Podocalyxin-GFP transfected MDCK tubes growing on micropatterns (upper). yz views are shown next. Scale bar, 50µm. Quantification (lower left) shows the lumen height in WT MDCK tubes and cells transfected with Podocalyxin-GFP. Values are mean ±SD from 3 different experiments. (n>40 tubes/experiment; ***, P<0,001). Quantification (lower right) shows the percentage of single lumen tubes. Values are mean ±SD from 3 different experiments. (n>100 tubes/experiment; *, P<0,05). **(C)** A plot of measurement of TER showing the initial polarisation stage and stationary stage of MDCKII (green) and T-23 (yellow) cells. MDCK and T-23 tubes growing on micropatterns are shown (upper right). Scale bar, 50µm. Quantification (lower left) shows the percentage of polarised tubes in MDCK and T-23 cells. Values are mean ±SD from 3 different experiments. (n>100 tubes/experiment; *, P<0,05). Quantification (lower right) shows percentage of single lumen tubes. Values are mean ±SD from 3 different experiments. (n>100 tubes/experiment; *, P<0,05).

A plethora of different mechanisms are controlling single lumen formation. 3D MDCK cyst model has provided many insights into the processes underlying apicobasal polarity acquisition during the last decades [65, 80, 87]. However, the study of lumen coalescence, a very important step during the morphogenesis of tubular organs, is difficult to study using the cyst model. Our micropattern-based system, in which multiple lumens form before the attainment of a unique tubular cavity, is a very suitable model to study this issue. In this sense, we proposed that PCP controls lumen coalescence and that tubular 3D structures grown on micropatterns could become a very potent model to study planar cell polarity *in vitro*, due to the fact that this model emulates the cellular distribution of a tubular epithelial sheet with an AP axis. Although we found that some of the PCP genes are overexpressed in MDCK and LLC-PK1 tubes, we did not find an evident effect of PCP effectors in lumen resolution. Given the high influence of PCP in tissue remodelling during morphogenetic processes, we cannot discard that PCP is indeed playing a role in lumen coalescence *in vivo* that is not reproduced in our *in vitro* model. This might be due to the fact that the 3D architecture and extracellular constraints *per se* do not suffice to regulate PCP signalling *in vitro.* Since upstream morphogenetic signalling pathways like non-canonical Wnt and Dpp are regulating PCP during morphogenesis, stimuli triggering this signalling might also be necessary to orchestrate PCP *in vitro*.

Regarding the effect of cell contractility and cytoskeletal regulation by RhoGTPases, we have confirmed that PCP is not controlling cell contractility in our model to promote junction remodelling. Besides, we have not detected any asymmetric accumulation of p-MRLC in tube junctions, however to better assess whether there is a remodelling or shrinkage of cell junctions between lumens during coalescence, high resolution time lapse microscopy on micropatterns should be performed. Alternatively, we tried to measure differences in mechanical tension and cell-generated forces on cell junctions by laser ablation (data not shown), but the setup of the technique was complex and the reproducibility was poor in micropatterns. Furthermore, we also inhibited actomyosin contractility using Blebbistatin (MyoII inhibitor), Y-27632 (ROCK inhibitor) or BDP5290 (MRCK inhibitor) obtaining interesting and controversial effects on tube morphology (not shown). The treatment with blebbistatin promoted an expansion of luminal interfaces while ROCK inhibitor produces ectopic lumen formation. These different effects would probably be due to an imbalance in MyosinII phosphorylation, which is controlled by different kinases that are in turn finely regulated by RhoGTPases [86, 87]. The interplay between RhoGTPases, myosin phosphorylation and lumen formation is still under study. The ultimate event of lumen coalescence, in which two apical membranes are supposed to fuse to give rise to a unique lumen, is still very poorly understood. We hypothesised that this event is the result of a cytoskeleton-regulated shrinking of cell junctions and a removal of tight junctions. A deeper characterisation of this process should be addressed in the future by analysing tight junction disassembly through electron

microscopy and by tracking photoconverted ZO-1 transfected cells during the lumen coalescence process.

Although we did not find evidence of cell rearrangements and junction remodelling in controlling lumen coalescence in our micropattern model, we found that lumen inflation, though, has a key role in this process. By modifying the osmotic concentration of the culturing media, the expression of glycoproteins or the TER, we were able to readjust the dynamics of lumen inflation and, hence, the size of the lumens. The increased lumen volume observed correlated with a higher percentage of tubes with a single lumen. This is consistent with the previous results *in vivo,* which showed that lumen formation and size are controlled by the paracellular transport of ions and water. Claudins, proteins that selectively allow or inhibit the passage of ions from and to the lumen [254], are involved in the modulation of this interchange. Interestingly, Claudin2 (expressed in proximal tubules) forms a paracellular pore for the passage of cations, and therefore the downregulation of Claudin-2 induces an increase of TER [255] whereas its ectopic expression causes an increase of permeability for small cations and a decrease of TER [256]. Thus, by manipulating genetically Claudin-2 expression, further evidence for the role of lumen inflation in lumen resolution could be obtained.

Overall, our micropattern model has emerged as a novel system to study epithelial tubulogenesis, providing the first physiological *in vitro* system to study lumen coalescence.

IV. RENAL EPITHELIAL TUBES ON MICROPATTERNS TO CONDUCT NEPHROTOXICITY ASSAYS

Currently, distal and proximal kidney cell lines from different species such as MDCK, human HK-2, or LLC-PK1 growing in conventional 2D monolayers, lack the 3D epithelial architecture, and thus, they are of limited use for toxicology and drug discovery studies. When grown on planar substrates such as extracellular matrix coated glass, they lack tubular architecture and stable functional characteristics of human renal cells as they often de-differentiate or lose metabolic activities. In contrast, in 3D culture the only way to induce formation and elongation of tubes from epithelial cells is artificially through the addition of cytokine growth factors such as HGF and TGF-β. On the other hand, 3D embryonic kidney rudiments developing in culture are costly and technically challenging for high-throughput applications when using scales below 96-well format. While *in vitro* cell-based systems have been an invaluable tool in cell biology, they suffer due to the lack of physiological relevance. Particularly, the discrepancy between *in vitro* and *in vivo* systems has been a bottleneck for the pharmaceutical industry in the drug development process. Moreover, the nephrotoxic effects of some molecules imply enormous obstacles when developing a new drug. In

this sense, we hypothesised that using a more physiologically relevant system such as our micropattern-based model could help improve the process of drug development and, particularly, the assessment of nephrotoxicity in developing drugs.

A deeper characterisation of our micropattern system was necessary to assess its suitability for drug nephrotoxicity testing. To perform these experiments we used LLC-PK1 cells because they are proximal tubule cells widely used by most of the pharmaceutical companies. The proximal tube is the part of the nephron in charge of drug secretion and reabsorption, a process through which drugs are concentrated within the cell, hence causing this nephrotoxic effects. Many drug transporters and receptors participate in the regulation of interstitial and intracellular concentrations of these substances, being responsible for substrate uptake and secretion as the first step in the renal elimination of the drug. We analysed the RNA expression levels of some of them both in 2D cultures and on micropatterns (Figure R30.A).

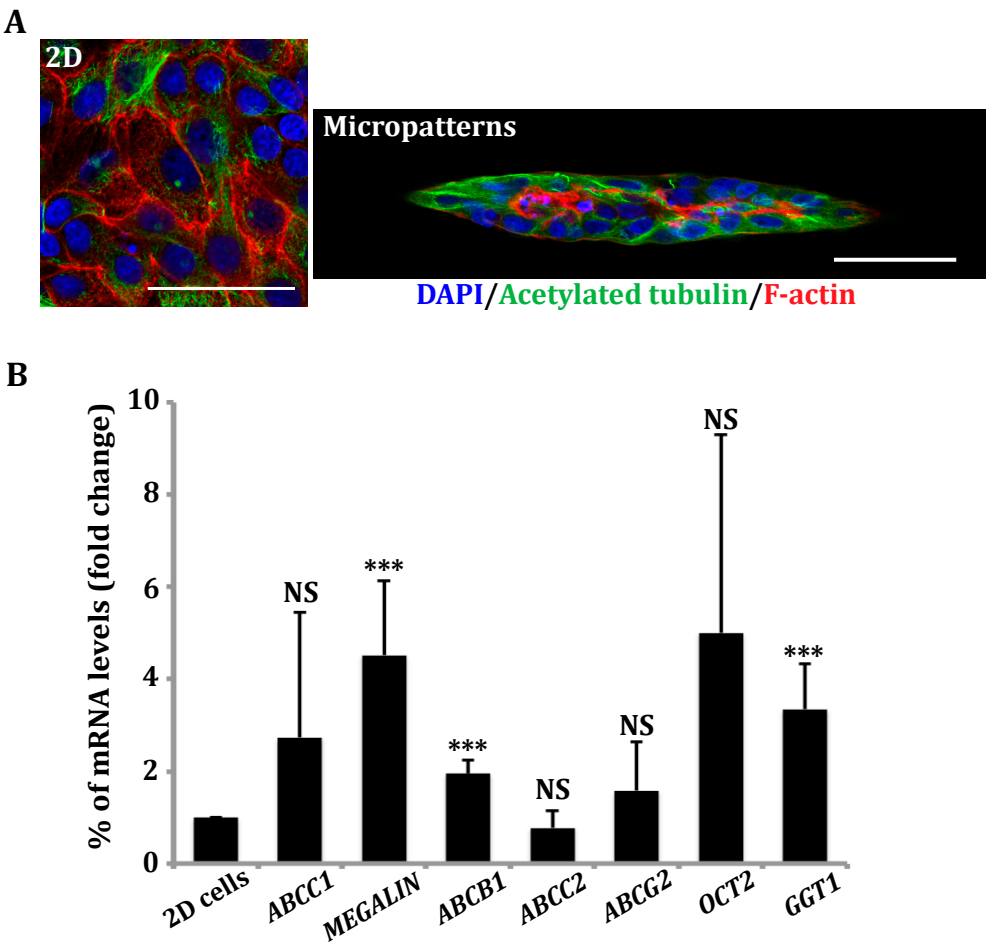

Figure R30. Drug transporter expression in LLC-PK1 cells. (A) LLC-PK1 cells growing as a monolayer (left) or in fibronectin-coated micropatterns (right) for 72h. Note, cells are better polarised in micropatterns as they assemble primary cilia in this condition. Scale bar, 50µm. **(B)** Quantification shows the mRNA levels (%) of different drug transporters expressed in the proximal tubule in cells growing on micropatterns compared to cells growing in 2D conditions. Values are mean ±SD from 4 different experiments. (NS, P>0,05; P<0,001).

We found Megalin (also known as Low density lipoprotein-related protein 2, LRP2), ATP binding cassette subfamily B member (ABCB1, also known as multi-drug resistance protein 1, MDR1) and γ-glutamyltransferase 1 (GGT1) to be upregulated in cells forming tubes on micropatterns compared to cells growing as 2D monolayers (Figure R30.B). This increased expression suggests that LLC-PK1 cells forming tubes on micropatterns are more functional as drug transport would be favoured. This, in turn, would make them more sensitive to nephrotoxic effects and thus, cells on micropatterns would detect drug-derived nephrotoxicity at lower concentrations.

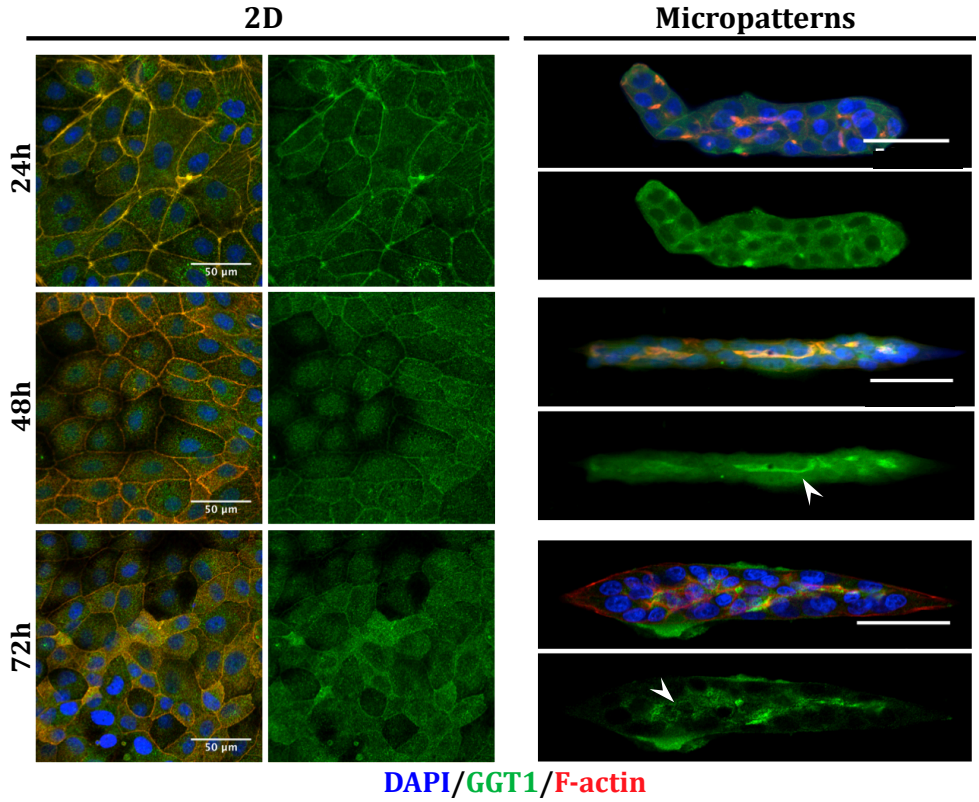

Figure R31. GGT1 transporter expression in LLC-PK1 cells. (A) Timecourse of LLC-PK1 cells growing as a monolayer (left) or in fibronectin-coated patterns (right) for 24h, 48h and 72h. Arrowheads indicate luminal localisation of GGT1. Scale bar, 50µm

To prove this, we better characterised the expression and distribution of some drug transporters. First, we performed a time-course analysis to determine the localisation of GGT1, organic cation transporter 2 (OCT2) and Megalin in 2D monolayers and micropatterns (Figures R31-R33). GGT1 is expressed on the luminal surface of excretive and absorptive cells throughout the body, with the highest level of GGT1 activity in the kidney [257]. Studies in GGT-knockout mice and cultured cells have shown that the chemotherapy drug, cisplatin, is metabolized to a nephrotoxin through this pathway, and inhibition of GGT blocks the nephrotoxicity of this drug [258, 259]. By IF, we saw that GGT1 localised to the cell cortex, accumulating at cell-cell junctions, in 2D monolayers at 24 and 48 hours, whereas GGT1 localisation in micropatterns presented striking differences as it started to

accumulate at the apical membranes from early stages (Figure R31.A). At 72h of growth, GGT1 localised to the cell cortex in monolayers while it is enriched at the apical membrane on micropatterns, staining the luminal cavity in the tubes.

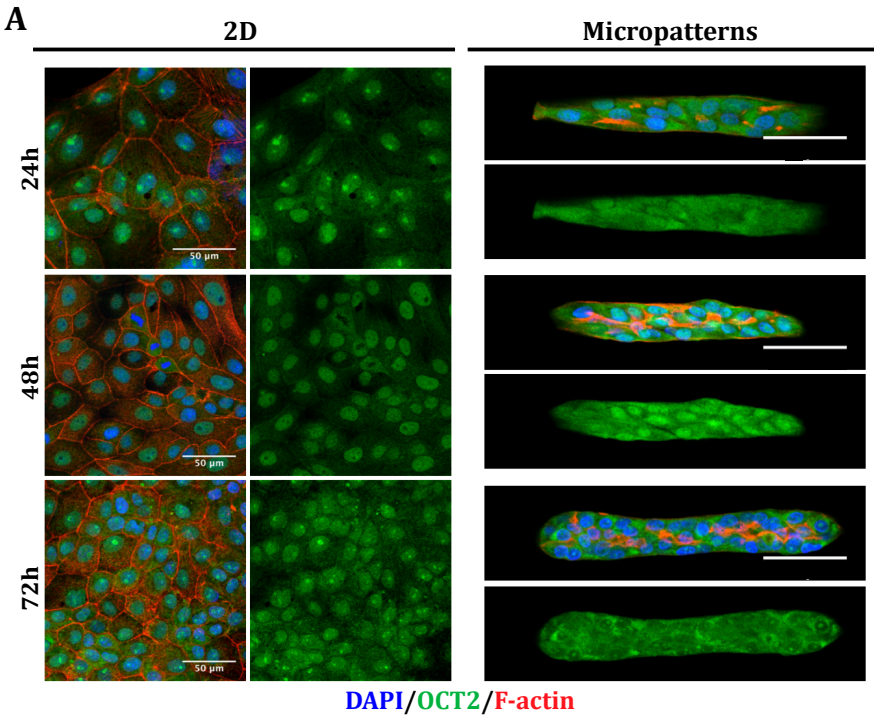

Figure R32. OCT2 transporter expression in LLC-PK1 cells. (A) Timecourse of LLC-PK1 cells growing as a monolayer (left) or growing on fibronectin-coated patterns (right) for 24h, 48h and 72h. Note, nuclear localisation of OCT1 is lost in 72h tubes. Scale bar, 50µm. **(B)** Immunoblot showing OCT1 protein levels in MDCK cells growing in 2D and on micropatterns at different time points (24h-72h).

OCT2 is a cation transporter typically localised to the basolateral membrane of proximal tubule cells. It normally behaves as an uptake transporter *in vivo*, filtering substances like organic cations, anionic and zwitterionic compounds and monoamine neurotransmitters from the blood into the proximal tubular cell [260, 261]. Is has been shown to participate in the cisplatin-derived nephrotoxic damage [262]. We observed nuclear staining in 2D monolayers and at the first stages of tube formation, while nuclear staining disappears at 72h of growth in micropatterns and appears diffused in the cytoplasm (Figure R32.A). This change in localisation seems to be related to the function of the transporter. Moreover, protein expression levels are much higher in cells growing on micropatterns as shown by immunoblot (Figure R32.B)

Megalin is a multiligand binding receptor found in the apical plasma membrane of many absorptive epithelial cells [263]. Megalin can form complexes with cubilin and mediates endocytosis of various molecules leading to degradation in lysosomes or transcytosis. However, evidence suggests that

megalin-cubilin complex is also involved in the uptake of toxic substances into proximal tubules, which leads to the development of kidney disease [264-266]. Megalin expression increased over time as low staining was detected at the first stages of growth (Figure R33). More importantly, however, was the fact that expression in the apical cell membrane was only detected in cells growing on micropatterns as early as at 42h of growth while yz views of cells in cells growing in 2D for 72h showed that megalin was diffused in the cytoplasm.

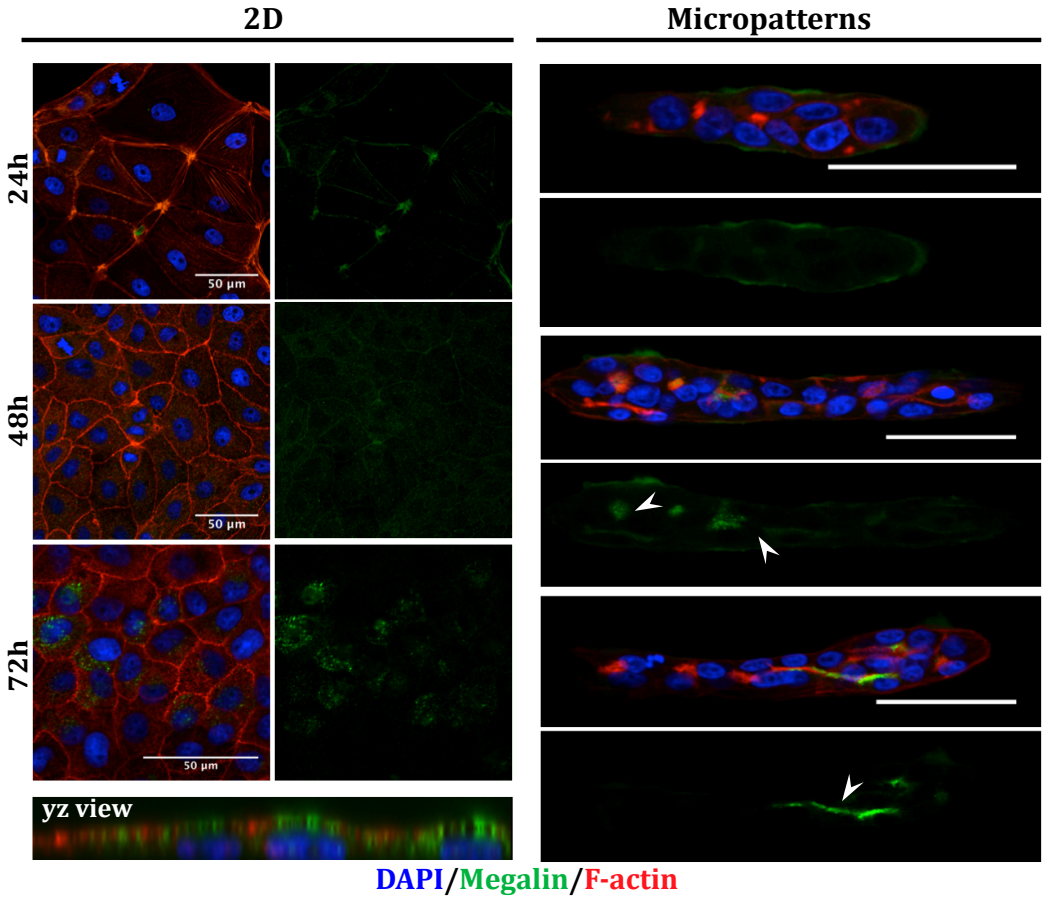

Figure R33. Megalin transporter expression in LLC-PK1 cells. (A) Timecourse of LLC-PK1 cells growing as a monolayer (left) or in fibronectin-coated patterns (right) for 24h, 48h and 72h. yz view of a 72h monolayer is shown (lower left). Arrowheads indicate luminal localisation of megalin. Scale bar, 50µm.

Besides the higher expression of some drugs transporters (Figure R30), we also demonstrated that the localisation of these proximal tubule proteins is more physiological in micropatterns than in 2D monolayers (Figures R31-R33). As many other proximal tubule proteins that are related to drug transport and metabolisation exist, a wider RNA screening would help to unveil the similarity of our model to *in vivo* proximal tubules. Moreover additional functional validation assays could be performed to confirm the metabolic competence, enzymatic activity or functionality of some of the transporters in our system. For example, fluorescent BSA or aprotonin uptake by megalin can be examined [264] as well as the transport and Lucifer Yellow using the basolaterally oriented p-aminohippurate transport system, followed by secretion into the lumen [267].

We further validated our system by treatment with a known nephrotoxic agent. Gentamicin is an antibiotic used to treat several types of bacterial infections and causes tubular damage and tubular dysfunction yielding to renal insufficiency [268, 269]. We treated LLC-PK1 cells with increasing concentrations of gentamicin and compared cell survival in 2D monolayers and on micropatterns. (Figure R34.A).

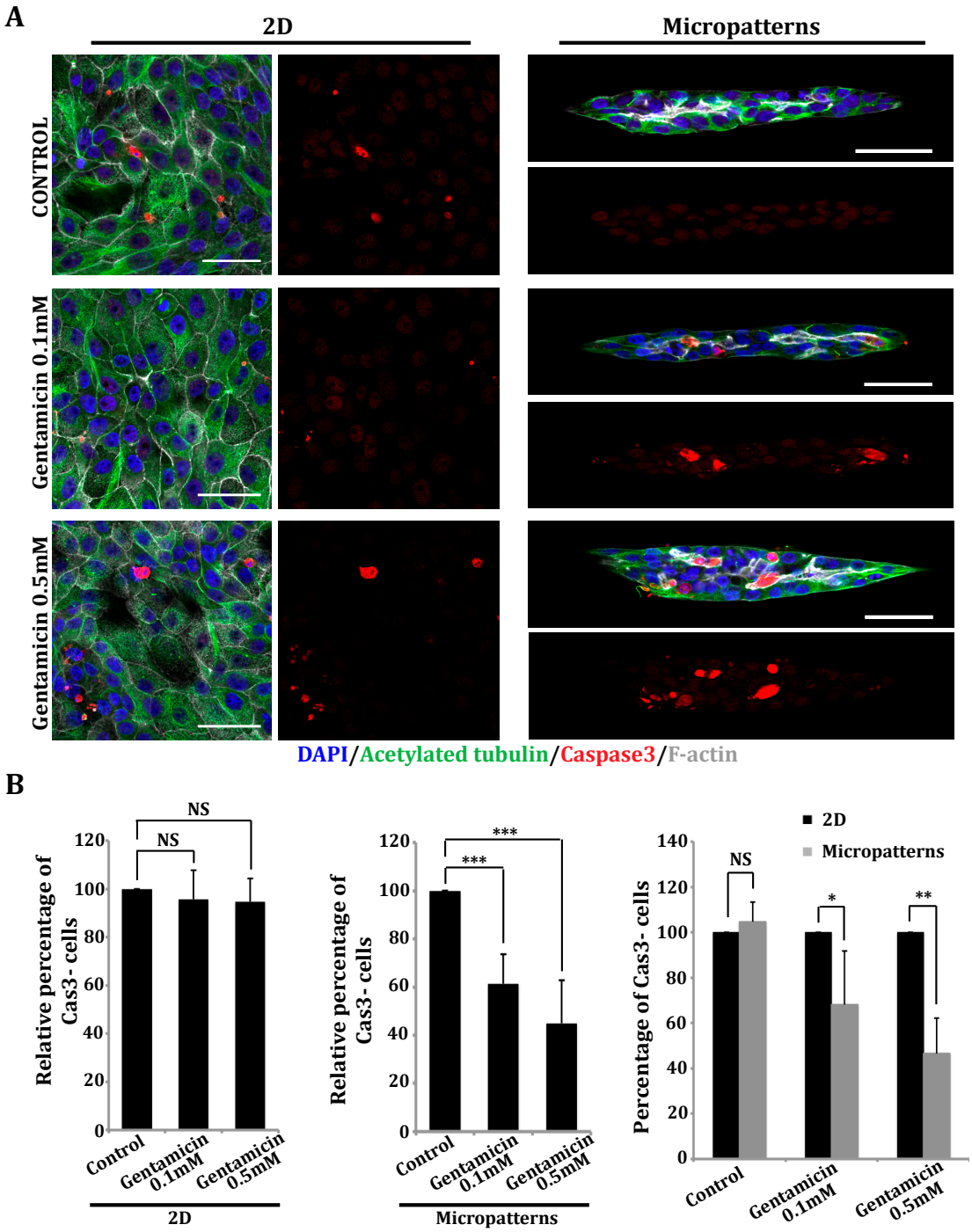

Figure R34. Gentamicin treatment and cell viability. (A) Gentamicin-treated LLC-PK1 cells growing as a monolayer (left) or in fibronectin-coated micropatterns (right) for 72h. Caspase3 staining labels apoptotic cells. Scale bar, 50µm. **(B)** Quantifications (left and central) show the percentage of Cas3$^-$ cells in control and gentamicin-treated cells relative to non treated cells growing as monolayers and on micropatterns respectively. Values are mean ±SD from 3 different experiments. (n>100 cells/condition; NS, P>0,05; ***P<0,001). Quantification (right) show the percentage of Cas3$^-$ cells in control and gentamicin-treated cells growing on micropatterns relative to cells growing as monolayers. Values are mean ±SD from 3 different experiments. (n>100 cells/condition; NS, P>0,05; ***P<0,001).

We treated cells with two different concentrations lower than those used in previous reports performed in 2D [270]. We did not observe a statistically significant difference in cell survival when analysing LLC-PK1 monolayers (Figure R34.B) between the control cells and cells treated either with 0.1mM or 0.5mM of gentamicin. However, we quantified the number of non-apoptotic cells on micropatterns and found that cell survival decreased in a dose-dependent manner compared to untreated cells (Figure R34.C). Strikingly, we observed that the same gentamicin doses produced different apoptotic responses depending on the culture model (Figure R34.D), with cells growing on micropatterns showing a higher sensitivity to gentamicin nephrotoxic effect.

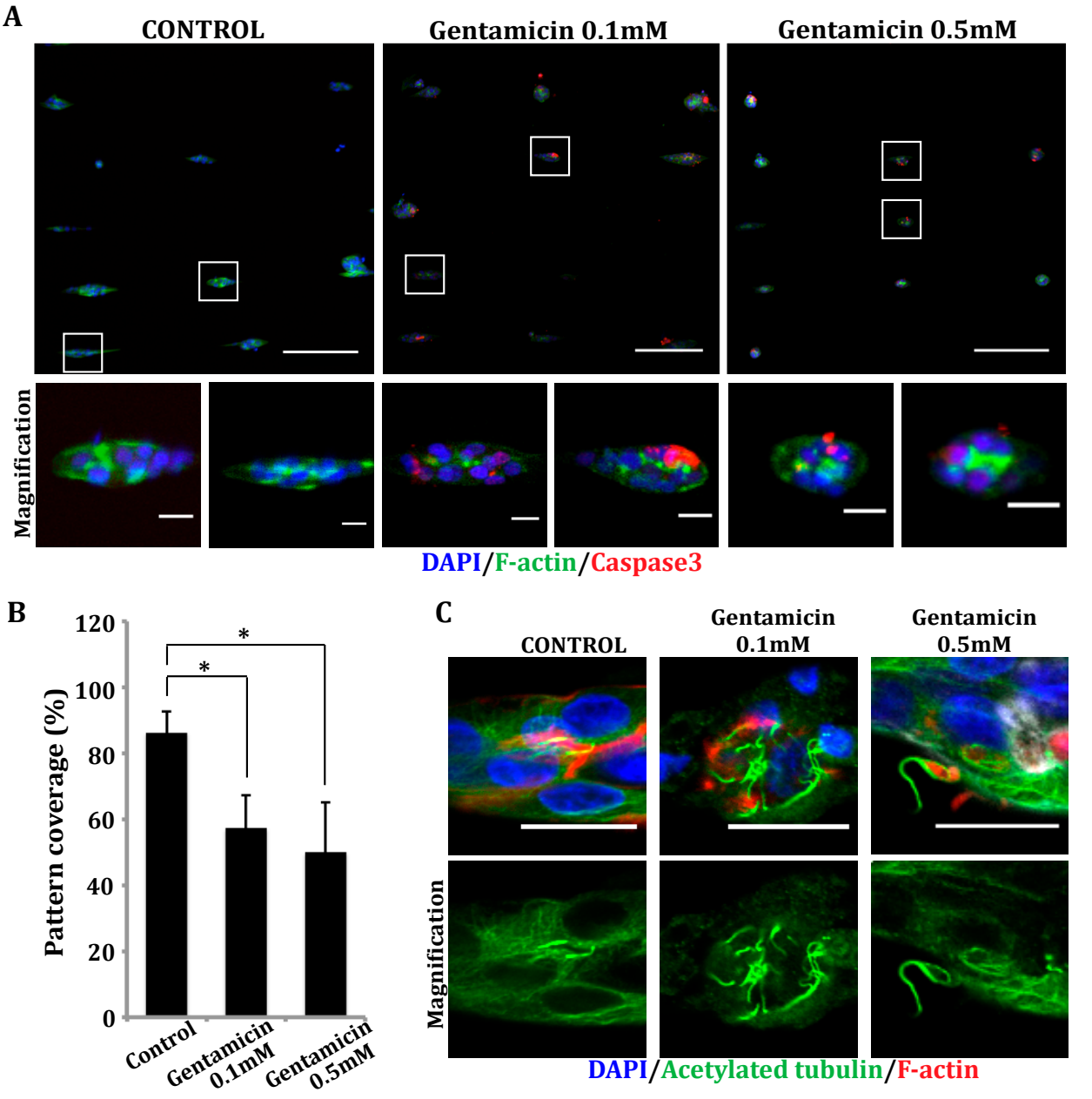

Figure R35. Gentamicin treatment and cell morphology. (A) Low magnification images of control and gentamicin-treated LLC-PK1 cells growing on fibronectin-coated micropatterns (upper) for 72h. Scale bar, 200µm. Scale bar magnification, 20µm. **(B)** Quantification shows the percentage of pattern coverage of gentamicin-treated tubes relative to control tubes. Values are mean ±SD from 3 different experiments. (n>1000 tubes/experiment *P<0,05). **(C)** Control and gentamicin-treated LLC-PK1 cells growing on fibronectin-coated micropatterns stained for acetylated tubulin to visualise primary cilia. Scale bar, 20µm.

We further correlated the toxicity response observed to visual endpoints such as cytoskeletal reorganisation, cell polarisation and primary cilia formation (Figure R35). Actually, we observed that tube spreading on the adhesive area was patently different when comparing gentamicin-treated cells with untreated cells (Figure R35.A-B). Indeed, treated tubes did also exhibit enlarged lumens (Figure R35.A). We also analysed the morphology of the primary cilium a hallmark of apicobasal polarity and cell functionality (Figure R35.A). We found aberrant formation of primary cilium as longer cilia were observed in some cases, more than one cilium per cell was frequently seen, and cilia formation in the outer part of the tubes indicated inverted polarity in cells treated with gentamicin.

The validation procedure has allowed us to highlight the advantages of this novel micropatterned-based platform versus the 2D traditional *in vitro* models and biopsies, providing a first-proof-of-concept for the pharmaceutical industry. By testing additional nephrotoxic drugs (such as cisplatin and acetylsalicylic acid) a more exhaustive determination, identification and classification of further growth defects could be done and used as nephrotoxicity markers. With a complete compilation of nephrotoxic hallmarks in micropatterns, the system would easily be used to extrapolate and predict the nephrotoxicity of new drugs with unknown nephrotoxic effects. Further validation involving the use of animal models could be used to corroborate the predictions *in vivo*.

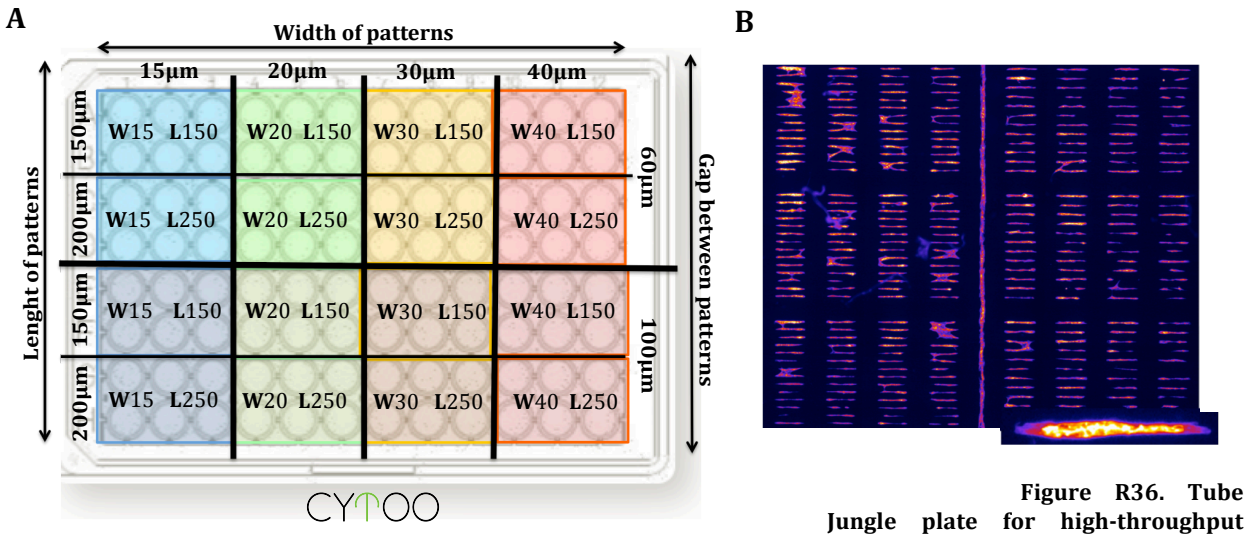

Figure R36. Tube Jungle plate for high-throughput nephrotoxicity screenings. (A) CYTOO design for a new 96-well plate with lines of different width, lengths and gaps. Not commercially available yet. **(B)** Pseudo-coloured tile-scan image of LLC-PK1 cells growing on tube patterns.

This proximal tubule model was adapted for the culture in 96-well plates, the minimum format for high-throughput nephrotoxicity screening purposes (Figure R36). Given the fact that various cell lines are used by the pharmacological industry to perform toxicology and drug discovery assays, the design of the patterns was done taking into consideration that different cell types may require distinct patterns shapes to form optimal tubes (Figure R36.A). With tube lengths of 150µm and 250µm and widths ranging between 15µm and 40µm, the platform was aimed to provide a system

in which to optimise and select the conditions to grow a specific cell line selected to be used in further pharmacological tests. Future directions should undertake studies analysing 3D tubes undergoing compound exposure to be used to detect biomarkers indicative of nephrotoxicity *in vivo*, thus enabling the translation from the *in vitro* to the *in vivo* situation. Bioengineered 3D tissues have been used for toxicity testing for both human liver [271] and skin [272], but a 3D system for human nephrotoxicity testing does not currently exist. Here we described a micropattern-based 3D porcine renal tube system and its assessment as a predictor of nephrotoxicity. However, this micropattern device can also be used to culture human renal epithelial cells (Figure R11) growing in 3D, which are morphologically similar to human kidney nephrons *in vivo*. Treatment of RPTEC/TERT1 cells with known nephrotoxicants could show that the human 3D tubes *in vitro* would be more sensitive to lower drug concentration than the same cells growing as 2D monolayers.

Modelling new devices, platforms or culture techniques that could mimic *in vitro*, to some extent, those processes occurring *in vivo* has been a major challenge in many fields, from molecular biology to translational research. These *in vitro* model systems can highly accelerate research as they are easy to handle and manipulate and, moreover, they present a way to circumvent animal experimentation when possible. In our case, growing renal tubes *in vitro* would provide a new platform for drug discovery and nephrotoxicity assays. This 'organ-on-a-chip' system is very interesting for the pharmaceutical industry as well as for molecular biology laboratories since it presents many advantages over traditional culture methods. Micropatterns allow the control of the size and shape of the culture platform, enabling precise control of extracellular microenvironmental constraints, thus providing geometrical and mechanical characteristics similar to those of the physiological models with high reproducibility. Furthermore, the coating with ECM proteins and the addition of MG provide polarisation signals that allow bypassing the use of porous filter supports. Since the platform is fabricated on a glass support, the resulting tubules are well suited for high-throughput screening, and high-content imaging and analysis, being also easily scaled to a 96-well format for high performance assays. Furthermore, tubes growing on micropatterns can also undergo genetic and biochemical modifications (such as siRNA, transfections, drugs, function-blocking antibodies, etc.).

Besides its potential use by the pharmaceutical industry, this tubule culture method will allow a deep characterisation of the processes taking place during tubulogenesis *in vitro* as shown by the similarity of tubulogenesis on micropatterns with morphogenetic processes occurring *in vivo.* This would be of great interest, as the molecular signalling events that govern cell rearrangements and membrane fusion to achieve lumen coalescence are not completely elucidated yet.

CONCLUSIONS

1. Mediante la tecnología basada en micropatrones adherentes se han generado sistemas de cultivo que permiten el crecimiento de túbulos epiteliales *in vitro*. La formación de dichas estructuras tubulares radica en el recubrimiento con componentes de la matriz extracelular que controlan la adhesión celular y orientan el eje apicobasal de las células. Esto permite que se forme un lúmen en el interior de la estructura. Estos sistemas de cultivo pueden fabricarse utilizando técnicas de "photopatterning" y "microcontact-printing" siendo adecuados tanto para el crecimiento de diferentes líneas de células epiteliales renales como para células derivadas de glándulas mamarias de ratón.

2. El proceso de formación de los túbulos renales en micropatrones sigue las mismas etapas de que la tubulogénesis de algunos órganos epiteliales como el intestino. Al cultivar células MDCK en micropatrones, éstas generan inicialmente múltiples lúmenes que se expanden y fusionan entre sí para generar un único lumen. Por lo tanto, el proceso fisiológico de tubulogénesis epitelial se puede reproducir *in vitro* mediante el uso de micropatrones.

3. Las dimensiones del área adhesiva determinan la morfología de los tubos de células MDCK ya que la longitud y el ancho de los micropatrones controlan tanto el número d células que se adhieren como el número de lúmenes formados. El tamaño y la forma del lumen también es controlado la anchura de la zona de adhesión del micropatrón, ya que las líneas estrechas promueven lúmenes más altos en comparación con las líneas anchas, cuyo efecto es el contrario. Además, la anchura del micropatrón influye en la orientación del huso mitótico, lo que favorece la alineación del eje del tubo con el eje del micropatrón

4. Los túbulos de células MDCK son capaces de crecer sobre diferentes proteínas de la matriz extracelular, hecho que genera la aparición de diferentes morfologías en función de la proteína utilizada para recubrir el micropatrón. La fibronectina favorece la extensión de las células mientras que la laminina promueve la adquisición de una estructura tubular más redondeada. El sustrato sobre el que crecen los túbulos afecta a la fuerza de adhesión de la células y explica las diferentes morfologías observadas en diferentes sustratos.

5. La rigidez del sustrato controla la expresión y la organización de los componentes de las adhesiones focales (paxilina, talina, vinculina α-actinina) y de algunos efectores de procesos de mecanotransducción (YAP1 y miosina-II) pero no tiene ningún papel en la morfología de los túbulos de MDCK cultivados en micropatrones.

6. Algunas proteínas de polaridad planar se sobreexpresan en células MDCK creciendo en micropatrones, pero los efectores Fuzzy y Celsr1 no tienen ningún papel en la coalescencia de lúmenes durante la tubulogénesis en micropatrones. Del mismo modo, la contracción mediada por miosina no esté controlando la remodelación de la uniones célula-célula en dicho modelo.

7. La expansión del lumen, debido tanto a la acumulación de fluido mediada por el transporte paracelular como a la repulsión de la membrana, favorece la coalescencia de lúmenes la formación de túbulos con un único lumen en células MDCK creciendo sobre micropatrones.

8. La expresión de algunos transportadores de fármacos específicos de túbulos proximales aumenta en células LLC-PK1 cultivadas sobre micropatrones en comparación con células creciendo en monocapa. Además, el crecimiento sobre micropatrones fomenta la correcta orientación y localización de dichos transportadores en la membrana celular. De acuerdo con esto, los túbulos de LLC-PK1 son más sensibles a bajas dosis de gentamicina que las células cultivadas en monocapa, ya que se induce una respuesta apoptótica en el caso de los túbulos que no se produce en células creciendo en 2D.

9. El tratamiento con gentamicina también induce defectos morfológicos y funcionales en los túbulos de células LLC-PK1 que no pueden observarse en monocapas. Entre dichos defectos se incluyen cambios en la forma tubular o la formación de cilios primarios

10. La configuración de este sistema de cultivo celular es fácilmente escalable a un formato de placa de 96 pocillos. Este formato resulta más adecuado para el cribado de alto rendimiento así como más atractivo para su comercialización.

1. Micropatterning technology, allows the generation of devices to grow epithelial tubes *in vitro*. The formation of the hollowed tubes is dependent on the coating with defined matrix components that control cell adhesion and orient the forming apical domain of the cells towards the centre of the closed tubule. These cell culture platforms can be developed using photo-patterning and microcontact-printing techniques and permit the growth of different renal epithelial cell lines, as well as mammary gland-derived cells.

2. Tube formation on micropatterns follows the same developmental stages as tubulogenesis in some epithelial organs such as the gut. When MDCK cells are grown in micropatterns, they initially generate multiple small lumens, which expand and resolve by fusing with each other to generate one single lumen. Thus, the process of epithelial tubulogenesis can be closely mimicked *in vitro* by using micropatterning technology.

3. The dimensions of the adhesive area determine the morphology of MDCK tubes as the length and width of the patterns control the number of lumens formed. Lumen size and shape are also controlled by pattern width as narrow lines promote taller lumens than wide ones. Moreover, pattern width influences spindle orientation favouring the alignment of the spindle with the tube axis in narrow patterns.

4. MDCK tubes can grow over different ECM components giving rise to tubes with different morphology. Fibronectin favours cell spreading and laminin promotes cell rounding, what impacts the adhesive strength of cells on these substrates and accounts for the different morphologies observed.

5. The stiffness of the substrate controls the expression and organisation of focal adhesion proteins (paxillin, talin, vinculin and α-actinin) and some mechanotransduction effectors (YAP1 and MyosinII) but have no impact on MDCK tube morphology.

6. Some planar cell polarity proteins are overexpressed in MDCK cells growing on micropatterns, but Fuzzy and Celsr1 effectors do not have a role in lumen coalescence. Likewise, myosin-mediated junction shrinking is not conducting junctional remodelling in MDCK cells growing on micropatterns.

7. Lumen expansion, due to both fluid accumulation driven by paracellular transport and membrane repulsion, is favouring lumen coalescence and the formation of single lumen tubes in MDCK cells.

8. In LLC-PK1 cells, the expression of some proximal tubule drug transporters is increased in micropatterns when compared to 2D monolayers. Moreover, micropatterns foster the correct targeting of drug transporters to the cell membrane. Consistent with this, LLC-PK1 tubes but no monolayers are sensitive to low doses of gentamicin, inducing an apoptotic response.

9. Gentamicin treatment also induces morphological and functional defects in LLC-PK1 tubes that cannot be observed in monolayers such as changes in tubular shape or the formation aberrant primary cilia.

10. The setup of this cell culture device is easily scalable to a 96-well plate format suitable for high-throughput screening and more attractive for its commercialisation.

REFERENCES

1. Leptin, M. (2005). Gastrulation movements: the logic and the nuts and bolts. Developmental cell *8*, 305-320.

2. Leptin, M. (1995). Drosophila gastrulation: from pattern formation to morphogenesis. Annual review of cell and developmental biology *11*, 189-212.

3. Oda, H., and Tsukita, S. (2001). Real-time imaging of cell-cell adherens junctions reveals that Drosophila mesoderm invagination begins with two phases of apical constriction of cells. Journal of cell science *114*, 493-501.

4. Wallingford, J.B., Fraser, S.E., and Harland, R.M. (2002). Convergent extension: the molecular control of polarized cell movement during embryonic development. Developmental cell *2*, 695-706.

5. Gumbiner, B.M. (1996). Cell adhesion: the molecular basis of tissue architecture and morphogenesis. Cell *84*, 345-357.

6. Kosmalska, A.J., Casares, L., Elosegui-Artola, A., Thottacherry, J.J., Moreno-Vicente, R., Gonzalez-Tarrago, V., del Pozo, M.A., Mayor, S., Arroyo, M., Navajas, D., et al. (2015). Physical principles of membrane remodelling during cell mechanoadaptation. Nature communications *6*, 7292.

7. Baum, B., and Georgiou, M. (2011). Dynamics of adherens junctions in epithelial establishment, maintenance, and remodeling. The Journal of cell biology *192*, 907-917.

8. Borghi, N., Lowndes, M., Maruthamuthu, V., Gardel, M.L., and Nelson, W.J. (2010). Regulation of cell motile behavior by crosstalk between cadherin- and integrin-mediated adhesions. Proceedings of the National Academy of Sciences of the United States of America *107*, 13324-13329.

9. Gudipaty, S.A., Lindblom, J., Loftus, P.D., Redd, M.J., Edes, K., Davey, C.F., Krishnegowda, V., and Rosenblatt, J. (2017). Mechanical stretch triggers rapid epithelial cell division through Piezo1. Nature *543*, 118-121.

10. Eisenhoffer, G.T., Loftus, P.D., Yoshigi, M., Otsuna, H., Chien, C.B., Morcos, P.A., and Rosenblatt, J. (2012). Crowding induces live cell extrusion to maintain homeostatic cell numbers in epithelia. Nature *484*, 546-549.

11. Andrade, D., and Rosenblatt, J. (2011). Apoptotic regulation of epithelial cellular extrusion. Apoptosis : an international journal on programmed cell death *16*, 491-501.

12. Lecuit, T., and Yap, A.S. (2015). E-cadherin junctions as active mechanical integrators in tissue dynamics. Nature cell biology *17*, 533-539.

13. Hogan, B.L., and Kolodziej, P.A. (2002). Organogenesis: molecular mechanisms of tubulogenesis. Nature reviews. Genetics *3*, 513-523.

14. Lubarsky, B., and Krasnow, M.A. (2003). Tube morphogenesis: making and shaping biological tubes. Cell *112*, 19-28.

15. Datta, A., Bryant, D.M., and Mostov, K.E. (2011). Molecular regulation of lumen morphogenesis. Current biology : CB *21*, R126-136.

16. Bryant, D.M., and Mostov, K.E. (2008). From cells to organs: building polarized tissue. Nature reviews. Molecular cell biology *9*, 887-901.

17. Iruela-Arispe, M.L., and Beitel, G.J. (2013). Tubulogenesis. Development *140*, 2851-2855.

18. Dessaud, E., McMahon, A.P., and Briscoe, J. (2008). Pattern formation in the vertebrate neural tube: a sonic hedgehog morphogen-regulated transcriptional network. Development *135*, 2489-2503.

19. Kerman, B.E., Cheshire, A.M., and Andrew, D.J. (2006). From fate to function: the Drosophila trachea and salivary gland as models for tubulogenesis. Differentiation; research in biological diversity *74*, 326-348.

20. Schottenfeld, J., Song, Y., and Ghabrial, A.S. (2010). Tube continued: morphogenesis of the Drosophila tracheal system. Current opinion in cell biology *22*, 633-639.

21. Debnath, J., Mills, K.R., Collins, N.L., Reginato, M.J., Muthuswamy, S.K., and Brugge, J.S. (2002). The role of apoptosis in creating and maintaining luminal space within normal and oncogene-expressing mammary acini. Cell *111*, 29-40.

22. Bagnat, M., Cheung, I.D., Mostov, K.E., and Stainier, D.Y. (2007). Genetic control of single lumen formation in the zebrafish gut. Nature cell biology *9*, 954-960.

23. Herwig, L., Blum, Y., Krudewig, A., Ellertsdottir, E., Lenard, A., Belting, H.G., and Affolter, M. (2013). Distinct cellular mechanisms of blood vessel fusion in the zebrafish embryo. Curr Biol *21*, 1942-1948.

24. Horne-Badovinac, S., Lin, D., Waldron, S., Schwarz, M., Mbamalu, G., Pawson, T., Jan, Y., Stainier, D.Y., and Abdelilah-Seyfried, S. (2001). Positional cloning of heart and soul reveals multiple roles for PKC lambda in zebrafish organogenesis. Current biology : CB *11*, 1492-1502.

25. Martin-Belmonte, F., and Mostov, K. (2008). Regulation of cell polarity during epithelial morphogenesis. Current opinion in cell biology *20*, 227-234.

26. Alvers, A.L., Ryan, S., Scherz, P.J., Huisken, J., and Bagnat, M. (2014). Single continuous lumen formation in the zebrafish gut is mediated by smoothened-dependent tissue remodeling. Development *141*, 1110-1119.

27. Seiler, C., Davuluri, G., Abrams, J., Byfield, F.J., Janmey, P.A., and Pack, M. (2012). Smooth muscle tension induces invasive remodeling of the zebrafish intestine. PLoS biology *10*, e1001386.

28. Barriere, G., Fici, P., Gallerani, G., Fabbri, F., and Rigaud, M. (2015). Epithelial Mesenchymal Transition: a double-edged sword. Clinical and translational medicine *4*, 14.

29. Martin-Belmonte, F., and Perez-Moreno, M. (2011). Epithelial cell polarity, stem cells and cancer. Nature reviews. Cancer *12*, 23-38.

30. Wei, S.C., Fattet, L., Tsai, J.H., Guo, Y., Pai, V.H., Majeski, H.E., Chen, A.C., Sah, R.L., Taylor, S.S., Engler, A.J., et al. (2015). Matrix stiffness drives epithelial-mesenchymal transition and tumour metastasis through a TWIST1-G3BP2 mechanotransduction pathway. Nature cell biology *17*, 678-688.

31. Tatin, F., Taddei, A., Weston, A., Fuchs, E., Devenport, D., Tissir, F., and Makinen, T. (2013). Planar cell polarity protein Celsr1 regulates endothelial adherens junctions and directed cell rearrangements during valve morphogenesis. Developmental cell *26*, 31-44.

32. Ossipova, O., Kim, K., Lake, B.B., Itoh, K., Ioannou, A., and Sokol, S.Y. (2014). Role of Rab11 in planar cell polarity and apical constriction during vertebrate neural tube closure. Nature communications *5*, 3734.

33. Djiane, A., Yogev, S., and Mlodzik, M. (2005). The apical determinants aPKC and dPatj regulate Frizzled-dependent planar cell polarity in the Drosophila eye. Cell *121*, 621-631.

34. Banerjee, J.J., Aerne, B.L., Holder, M.V., Hauri, S., Gstaiger, M., and Tapon, N. (2017). Meru couples planar cell polarity with apical-basal polarity during asymmetric cell division. eLife *6*.

35. VanderVorst, K., Hatakeyama, J., Berg, A., Lee, H., and Carraway, K.L., 3rd (2017). Cellular and molecular mechanisms underlying planar cell polarity pathway contributions to cancer malignancy. Seminars in cell & developmental biology.

36. Yang, J., and Weinberg, R.A. (2008). Epithelial-mesenchymal transition: at the crossroads of development and tumor metastasis. Developmental cell *14*, 818-829.

37. Vizirianakis, I.S., Chen, Y.Q., Kantak, S.S., Tsiftsoglou, A.S., and Kramer, R.H. (2002). Dominant-negative E-cadherin alters adhesion and reverses contact inhibition of growth in breast carcinoma cells. International journal of oncology *21*, 135-144.

38. Sigurbjornsdottir, S., Mathew, R., and Leptin, M. (2014). Molecular mechanisms of de novo lumen formation. Nature reviews. Molecular cell biology *15*, 665-676.

39. Roman-Fernandez, A., and Bryant, D.M. (2016). Complex Polarity: Building Multicellular Tissues Through Apical Membrane Traffic. Traffic *17*, 1244-1261.

40. Pocha, S.M., and Knust, E. (2013). Complexities of Crumbs function and regulation in tissue morphogenesis. Current biology : CB *23*, R289-293.

41. Goldstein, B., and Macara, I.G. (2007). The PAR proteins: fundamental players in animal cell polarization. Developmental cell *13*, 609-622.

42. Bulgakova, N.A., and Knust, E. (2009). The Crumbs complex: from epithelial-cell polarity to retinal degeneration. Journal of cell science *122*, 2587-2596.

43. Yamanaka, T., and Ohno, S. (2008). Role of Lgl/Dlg/Scribble in the regulation of epithelial junction, polarity and growth. Frontiers in bioscience : a journal and virtual library *13*, 6693-6707.

44. Asnacios, A., and Hamant, O. (2012). The mechanics behind cell polarity. Trends in cell biology *22*, 584-591.

45. Hynes, R.O., and Naba, A. (2012). Overview of the matrisome--an inventory of extracellular matrix constituents and functions. Cold Spring Harbor perspectives in biology *4*, a004903.

46. Geiger, B., and Yamada, K.M. (2011). Molecular architecture and function of matrix adhesions. Cold Spring Harbor perspectives in biology *3*.

47. Nelson, C.M., and Bissell, M.J. (2006). Of extracellular matrix, scaffolds, and signaling: tissue architecture regulates development, homeostasis, and cancer. Annual review of cell and developmental biology *22*, 287-309.

48. Lu, P., Takai, K., Weaver, V.M., and Werb, Z. (2011). Extracellular matrix degradation and remodeling in development and disease. Cold Spring Harbor perspectives in biology *3*.

49. Denef, N., Chen, Y., Weeks, S.D., Barcelo, G., and Schupbach, T. (2008). Crag regulates epithelial architecture and polarized deposition of basement membrane proteins in Drosophila. Developmental cell *14*, 354-364.

50. Urbano, J.M., Torgler, C.N., Molnar, C., Tepass, U., Lopez-Varea, A., Brown, N.H., de Celis, J.F., and Martin-Bermudo, M.D. (2009). Drosophila laminins act as key regulators of basement membrane assembly and morphogenesis. Development *136*, 4165-4176.

51. Akhtar, N., and Streuli, C.H. (2013). An integrin-ILK-microtubule network orients cell polarity and lumen formation in glandular epithelium. Nature cell biology *15*, 17-27.

52. Wu, W., Kitamura, S., Truong, D.M., Rieg, T., Vallon, V., Sakurai, H., Bush, K.T., Vera, D.R., Ross, R.S., and Nigam, S.K. (2009). Beta1-integrin is required for kidney collecting duct morphogenesis and maintenance of renal function. American journal of physiology. Renal physiology *297*, F210-217.

53. Naylor, M.J., Li, N., Cheung, J., Lowe, E.T., Lambert, E., Marlow, R., Wang, P., Schatzmann, F., Wintermantel, T., Schuetz, G., et al. (2005). Ablation of beta1 integrin in mammary epithelium reveals a key role for integrin in glandular morphogenesis and differentiation. The Journal of cell biology *171*, 717-728.

54. Yu, W., Datta, A., Leroy, P., O'Brien, L.E., Mak, G., Jou, T.S., Matlin, K.S., Mostov, K.E., and Zegers, M.M. (2005). Beta1-integrin orients epithelial polarity via Rac1 and laminin. Molecular biology of the cell *16*, 433-445.

55. Di Paolo, G., and De Camilli, P. (2006). Phosphoinositides in cell regulation and membrane dynamics. Nature *443*, 651-657.

56. Carracedo, A., and Pandolfi, P.P. (2008). The PTEN-PI3K pathway: of feedbacks and cross-talks. Oncogene *27*, 5527-5541.

57. Rodriguez-Boulan, E., Kreitzer, G., and Musch, A. (2005). Organization of vesicular trafficking in epithelia. Nature reviews. Molecular cell biology *6*, 233-247.

58. Mostov, K., Su, T., and ter Beest, M. (2003). Polarized epithelial membrane traffic: conservation and plasticity. Nature cell biology *5*, 287-293.

59. Folsch, H. (2008). Regulation of membrane trafficking in polarized epithelial cells. Current opinion in cell biology *20*, 208-213.

60. Eaton, S., and Martin-Belmonte, F. (2014). Cargo sorting in the endocytic pathway: a key regulator of cell polarity and tissue dynamics. Cold Spring Harbor perspectives in biology *6*, a016899.

61. Rodriguez-Fraticelli, A.E., Bagwell, J., Bosch-Fortea, M., Boncompain, G., Reglero-Real, N., Garcia-Leon, M.J., Andres, G., Toribio, M.L., Alonso, M.A., Millan, J., et al. (2015). Developmental regulation of apical endocytosis controls epithelial patterning in vertebrate tubular organs. Nature cell biology *17*, 241-250.

62. Desclozeaux, M., Venturato, J., Wylie, F.G., Kay, J.G., Joseph, S.R., Le, H.T., and Stow, J.L. (2008). Active Rab11 and functional recycling endosome are required for E-cadherin trafficking and lumen formation during epithelial morphogenesis. American journal of physiology. Cell physiology *295*, C545-556.

63. Langevin, J., Morgan, M.J., Sibarita, J.B., Aresta, S., Murthy, M., Schwarz, T., Camonis, J., and Bellaiche, Y. (2005). Drosophila exocyst components Sec5, Sec6, and Sec15 regulate DE-Cadherin trafficking from recycling endosomes to the plasma membrane. Developmental cell *9*, 365-376.

64. Madrid, R., Aranda, J.F., Rodriguez-Fraticelli, A.E., Ventimiglia, L., Andres-Delgado, L., Shehata, M., Fanayan, S., Shahheydari, H., Gomez, S., Jimenez, A., et al. (2010). The formin INF2 regulates basolateral-to-apical transcytosis and lumen formation in association with Cdc42 and MAL2. Developmental cell *18*, 814-827.

65. Bryant, D.M., Datta, A., Rodriguez-Fraticelli, A.E., Peranen, J., Martin-Belmonte, F., and Mostov, K.E. (2010). A molecular network for de novo generation of the apical surface and lumen. Nature cell biology *12*, 1035-1045.

66. Lujan, P., Varsano, G., Rubio, T., Hennrich, M.L., Sachsenheimer, T., Galvez-Santisteban, M., Martin-Belmonte, F., Gavin, A.C., Brugger, B., and Kohn, M. (2016). PRL-3 disrupts epithelial architecture by altering the post-mitotic midbody position. Journal of cell science *129*, 4130-4142.

67. Schluter, M.A., Pfarr, C.S., Pieczynski, J., Whiteman, E.L., Hurd, T.W., Fan, S., Liu, C.J., and Margolis, B. (2009). Trafficking of Crumbs3 during cytokinesis is crucial for lumen formation. Molecular biology of the cell *20*, 4652-4663.

68. Bernabe-Rubio, M., Andres, G., Casares-Arias, J., Fernandez-Barrera, J., Rangel, L., Reglero-Real, N., Gershlick, D.C., Fernandez, J.J., Millan, J., Correas, I., et al. (2016). Novel role for the midbody in primary ciliogenesis by polarized epithelial cells. The Journal of cell biology *214*, 259-273.

69. Siller, K.H., and Doe, C.Q. (2009). Spindle orientation during asymmetric cell division. Nature cell biology *11*, 365-374.

70. Yu, F., Morin, X., Cai, Y., Yang, X., and Chia, W. (2000). Analysis of partner of inscuteable, a novel player of Drosophila asymmetric divisions, reveals two distinct steps in inscuteable apical localization. Cell *100*, 399-409.

71. Schaefer, M., Shevchenko, A., Shevchenko, A., and Knoblich, J.A. (2000). A protein complex containing Inscuteable and the Galpha-binding protein Pins orients asymmetric cell divisions in Drosophila. Current biology : CB *10*, 353-362.

72. Du, Q., Stukenberg, P.T., and Macara, I.G. (2001). A mammalian Partner of inscuteable binds NuMA and regulates mitotic spindle organization. Nature cell biology *3*, 1069-1075.

73. Cai, Y., Yu, F., Lin, S., Chia, W., and Yang, X. (2003). Apical complex genes control mitotic spindle geometry and relative size of daughter cells in Drosophila neuroblast and pI asymmetric divisions. Cell *112*, 51-62.

74. Morin, X., Jaouen, F., and Durbec, P. (2007). Control of planar divisions by the G-protein regulator LGN maintains progenitors in the chick neuroepithelium. Nature neuroscience *10*, 1440-1448.

75. Peyre, E., Jaouen, F., Saadaoui, M., Haren, L., Merdes, A., Durbec, P., and Morin, X. (2011). A lateral belt of cortical LGN and NuMA guides mitotic spindle movements and planar division in neuroepithelial cells. The Journal of cell biology *193*, 141-154.

76. Zheng, Z., Zhu, H., Wan, Q., Liu, J., Xiao, Z., Siderovski, D.P., and Du, Q. (2010). LGN regulates mitotic spindle orientation during epithelial morphogenesis. The Journal of cell biology *189*, 275-288.

77. Hao, Y., Du, Q., Chen, X., Zheng, Z., Balsbaugh, J.L., Maitra, S., Shabanowitz, J., Hunt, D.F., and Macara, I.G. (2010). Par3 controls epithelial spindle orientation by aPKC-mediated phosphorylation of apical Pins. Current biology : CB *20*, 1809-1818.

78. Durgan, J., Kaji, N., Jin, D., and Hall, A. (2011). Par6B and atypical PKC regulate mitotic spindle orientation during epithelial morphogenesis. The Journal of biological chemistry *286*, 12461-12474.

79. Le, L.T., Cazares, O., Mouw, J.K., Chatterjee, S., Macias, H., Moran, A., Ramos, J., Keely, P.J., Weaver, V.M., and Hinck, L. (2016). Loss of miR-203 regulates cell shape and matrix adhesion through ROBO1/Rac/FAK in response to stiffness. The Journal of cell biology *212*, 707-719.

80. Banon-Rodriguez, I., Galvez-Santisteban, M., Vergarajauregui, S., Bosch, M., Borreguero-Pascual, A., and Martin-Belmonte, F. (2014). EGFR controls IQGAP basolateral membrane localization and mitotic spindle orientation during epithelial morphogenesis. The EMBO journal *33*, 129-145.

81. Strilic, B., Kucera, T., Eglinger, J., Hughes, M.R., McNagny, K.M., Tsukita, S., Dejana, E., Ferrara, N., and Lammert, E. (2009). The molecular basis of vascular lumen formation in the developing mouse aorta. Developmental cell *17*, 505-515.

82. Strilic, B., Eglinger, J., Krieg, M., Zeeb, M., Axnick, J., Babal, P., Muller, D.J., and Lammert, E. (2010). Electrostatic cell-surface repulsion initiates lumen formation in developing blood vessels. Current biology : CB *20*, 2003-2009.

83. Meder, D., Shevchenko, A., Simons, K., and Fullekrug, J. (2005). Gp135/podocalyxin and NHERF-2 participate in the formation of a preapical domain during polarization of MDCK cells. The Journal of cell biology *168*, 303-313.

84. Martin, A.C., Kaschube, M., and Wieschaus, E.F. (2009). Pulsed contractions of an actin-myosin network drive apical constriction. Nature *457*, 495-499.

85. Gutzman, J.H., and Sive, H. (2010). Epithelial relaxation mediated by the myosin phosphatase regulator Mypt1 is required for brain ventricle lumen expansion and hindbrain morphogenesis. Development *137*, 795-804.

86. Zihni, C., Vlassaks, E., Terry, S., Carlton, J., Leung, T.K.C., Olson, M., Pichaud, F., Balda, M.S., and Matter, K. (2017). An apical MRCK-driven morphogenetic pathway controls epithelial polarity. Nature cell biology *19*, 1049-1060.

87. Rodriguez-Fraticelli, A.E., Auzan, M., Alonso, M.A., Bornens, M., and Martin-Belmonte, F. (2012). Cell confinement controls centrosome positioning and lumen initiation during epithelial morphogenesis. The Journal of cell biology *198*, 1011-1023.

88. Krupinski, T., and Beitel, G.J. (2009). Unexpected roles of the Na-K-ATPase and other ion transporters in cell junctions and tubulogenesis. Physiology *24*, 192-201.

89. Zhang, J., Piontek, J., Wolburg, H., Piehl, C., Liss, M., Otten, C., Christ, A., Willnow, T.E., Blasig, I.E., and Abdelilah-Seyfried, S. (2010). Establishment of a neuroepithelial barrier by Claudin5a is essential for zebrafish brain ventricular lumen expansion. Proceedings of the National Academy of Sciences of the United States of America *107*, 1425-1430.

90. Cheung, I.D., Bagnat, M., Ma, T.P., Datta, A., Evason, K., Moore, J.C., Lawson, N.D., Mostov, K.E., Moens, C.B., and Stainier, D.Y. (2012). Regulation of intrahepatic biliary duct morphogenesis by Claudin 15-like b. Developmental biology *361*, 68-78.

91. Yang, B., Sonawane, N.D., Zhao, D., Somlo, S., and Verkman, A.S. (2008). Small-molecule CFTR inhibitors slow cyst growth in polycystic kidney disease. Journal of the American Society of Nephrology : JASN *19*, 1300-1310.

92. Bagnat, M., Navis, A., Herbstreith, S., Brand-Arzamendi, K., Curado, S., Gabriel, S., Mostov, K., Huisken, J., and Stainier, D.Y. (2010). Cse1l is a negative regulator of CFTR-dependent fluid secretion. Current biology : CB *20*, 1840-1845.

93. Laprise, P., Paul, S.M., Boulanger, J., Robbins, R.M., Beitel, G.J., and Tepass, U. (2010). Epithelial polarity proteins regulate Drosophila tracheal tube size in parallel to the luminal matrix pathway. Current biology : CB *20*, 55-61.

94. Laprise, P., Lau, K.M., Harris, K.P., Silva-Gagliardi, N.F., Paul, S.M., Beronja, S., Beitel, G.J., McGlade, C.J., and Tepass, U. (2009). Yurt, Coracle, Neurexin IV and the Na(+),K(+)-ATPase form a novel group of epithelial polarity proteins. Nature *459*, 1141-1145.

95. Jones, C., Roper, V.C., Foucher, I., Qian, D., Banizs, B., Petit, C., Yoder, B.K., and Chen, P. (2008). Ciliary proteins link basal body polarization to planar cell polarity regulation. Nature genetics *40*, 69-77.

96. Song, H., Hu, J., Chen, W., Elliott, G., Andre, P., Gao, B., and Yang, Y. (2010). Planar cell polarity breaks bilateral symmetry by controlling ciliary positioning. Nature *466*, 378-382.

97. Carvajal-Gonzalez, J.M., Roman, A.C., and Mlodzik, M. (2016). Positioning of centrioles is a conserved readout of Frizzled planar cell polarity signalling. Nature communications *7*, 11135.

98. Montcouquiol, M., Sans, N., Huss, D., Kach, J., Dickman, J.D., Forge, A., Rachel, R.A., Copeland, N.G., Jenkins, N.A., Bogani, D., et al. (2006). Asymmetric localization of Vangl2 and Fz3 indicate novel mechanisms for planar cell polarity in mammals. The Journal of neuroscience : the official journal of the Society for Neuroscience *26*, 5265-5275.

99. Dabdoub, A., Donohue, M.J., Brennan, A., Wolf, V., Montcouquiol, M., Sassoon, D.A., Hseih, J.C., Rubin, J.S., Salinas, P.C., and Kelley, M.W. (2003). Wnt signaling mediates reorientation of outer hair cell stereociliary bundles in the mammalian cochlea. Development *130*, 2375-2384.

100. Wang, J., Mark, S., Zhang, X., Qian, D., Yoo, S.J., Radde-Gallwitz, K., Zhang, Y., Lin, X., Collazo, A., Wynshaw-Boris, A., et al. (2005). Regulation of polarized extension and planar cell polarity in the cochlea by the vertebrate PCP pathway. Nature genetics *37*, 980-985.

101. Devenport, D., and Fuchs, E. (2008). Planar polarization in embryonic epidermis orchestrates global asymmetric morphogenesis of hair follicles. Nature cell biology *10*, 1257-1268.

102. Sagner, A., Merkel, M., Aigouy, B., Gaebel, J., Brankatschk, M., Julicher, F., and Eaton, S. (2012). Establishment of global patterns of planar polarity during growth of the Drosophila wing epithelium. Current biology : CB *22*, 1296-1301.

103. Kibar, Z., Salem, S., Bosoi, C.M., Pauwels, E., De Marco, P., Merello, E., Bassuk, A.G., Capra, V., and Gros, P. (2011). Contribution of VANGL2 mutations to isolated neural tube defects. Clinical genetics *80*, 76-82.

104. Murdoch, J.N., Doudney, K., Paternotte, C., Copp, A.J., and Stanier, P. (2001). Severe neural tube defects in the loop-tail mouse result from mutation of Lpp1, a novel gene involved in floor plate specification. Human molecular genetics *10*, 2593-2601.

105. Curtin, J.A., Quint, E., Tsipouri, V., Arkell, R.M., Cattanach, B., Copp, A.J., Henderson, D.J., Spurr, N., Stanier, P., Fisher, E.M., et al. (2003). Mutation of Celsr1 disrupts planar polarity of inner ear hair cells and causes severe neural tube defects in the mouse. Current biology : CB *13*, 1129-1133.

106. Wang, Y., Zhang, J., Mori, S., and Nathans, J. (2006). Axonal growth and guidance defects in Frizzled3 knock-out mice: a comparison of diffusion tensor magnetic resonance imaging, neurofilament staining, and genetically directed cell labeling. The Journal of neuroscience : the official journal of the Society for Neuroscience *26*, 355-364.

107. Wang, Y., Guo, N., and Nathans, J. (2006). The role of Frizzled3 and Frizzled6 in neural tube closure and in the planar polarity of inner-ear sensory hair cells. The Journal of neuroscience : the official journal of the Society for Neuroscience *26*, 2147-2156.

108. Kim, S.K., Shindo, A., Park, T.J., Oh, E.C., Ghosh, S., Gray, R.S., Lewis, R.A., Johnson, C.A., Attie-Bittach, T., Katsanis, N., et al. (2010). Planar cell polarity acts through septins to control collective cell movement and ciliogenesis. Science *329*, 1337-1340.

109. Bayly, R., and Axelrod, J.D. (2011). Pointing in the right direction: new developments in the field of planar cell polarity. Nature reviews. Genetics *12*, 385-391.

110. Vladar, E.K., Antic, D., and Axelrod, J.D. (2009). Planar cell polarity signaling: the developing cell's compass. Cold Spring Harbor perspectives in biology *1*, a002964.

111. Axelrod, J.D. (2001). Unipolar membrane association of Dishevelled mediates Frizzled planar cell polarity signaling. Genes & development *15*, 1182-1187.

112. Strutt, D.I. (2001). Asymmetric localization of frizzled and the establishment of cell polarity in the Drosophila wing. Molecular cell *7*, 367-375.

113. Feiguin, F., Hannus, M., Mlodzik, M., and Eaton, S. (2001). The ankyrin repeat protein Diego mediates Frizzled-dependent planar polarization. Developmental cell *1*, 93-101.

114. Tree, D.R., Shulman, J.M., Rousset, R., Scott, M.P., Gubb, D., and Axelrod, J.D. (2002). Prickle mediates feedback amplification to generate asymmetric planar cell polarity signaling. Cell *109*, 371-381.

115. Bastock, R., Strutt, H., and Strutt, D. (2003). Strabismus is asymmetrically localised and binds to Prickle and Dishevelled during Drosophila planar polarity patterning. Development *130*, 3007-3014.

116. Shimada, Y., Usui, T., Yanagawa, S., Takeichi, M., and Uemura, T. (2001). Asymmetric colocalization of Flamingo, a seven-pass transmembrane cadherin, and Dishevelled in planar cell polarization. Current biology : CB *11*, 859-863.

117. Brittle, A., Thomas, C., and Strutt, D. (2012). Planar polarity specification through asymmetric subcellular localization of Fat and Dachsous. Current biology : CB *22*, 907-914.

118. Matis, M., and Axelrod, J.D. (2013). Regulation of PCP by the Fat signaling pathway. Genes & development *27*, 2207-2220.

119. Ambegaonkar, A.A., Pan, G., Mani, M., Feng, Y., and Irvine, K.D. (2012). Propagation of Dachsous-Fat planar cell polarity. Current biology : CB *22*, 1302-1308.

120. Matakatsu, H., and Blair, S.S. (2004). Interactions between Fat and Dachsous and the regulation of planar cell polarity in the Drosophila wing. Development *131*, 3785-3794.

121. Tree, D.R., Ma, D., and Axelrod, J.D. (2002). A three-tiered mechanism for regulation of planar cell polarity. Seminars in cell & developmental biology *13*, 217-224.

122. Heisenberg, C.P., Tada, M., Rauch, G.J., Saude, L., Concha, M.L., Geisler, R., Stemple, D.L., Smith, J.C., and Wilson, S.W. (2000). Silberblick/Wnt11 mediates convergent extension movements during zebrafish gastrulation. Nature *405*, 76-81.

123. Kilian, B., Mansukoski, H., Barbosa, F.C., Ulrich, F., Tada, M., and Heisenberg, C.P. (2003). The role of Ppt/Wnt5 in regulating cell shape and movement during zebrafish gastrulation. Mechanisms of development *120*, 467-476.

124. Qian, D., Jones, C., Rzadzinska, A., Mark, S., Zhang, X., Steel, K.P., Dai, X., and Chen, P. (2007). Wnt5a functions in planar cell polarity regulation in mice. Developmental biology *306*, 121-133.

125. Gao, B., Song, H., Bishop, K., Elliot, G., Garrett, L., English, M.A., Andre, P., Robinson, J., Sood, R., Minami, Y., et al. (2011). Wnt signaling gradients establish planar cell polarity by inducing Vangl2 phosphorylation through Ror2. Developmental cell *20*, 163-176.

126. Wallingford, J.B., Rowning, B.A., Vogeli, K.M., Rothbacher, U., Fraser, S.E., and Harland, R.M. (2000). Dishevelled controls cell polarity during Xenopus gastrulation. Nature *405*, 81-85.

127. Keller, R. (2002). Shaping the vertebrate body plan by polarized embryonic cell movements. Science *298*, 1950-1954.

128. Darken, R.S., Scola, A.M., Rakeman, A.S., Das, G., Mlodzik, M., and Wilson, P.A. (2002). The planar polarity gene strabismus regulates convergent extension movements in Xenopus. The EMBO journal *21*, 976-985.

129. Tada, M., and Smith, J.C. (2000). Xwnt11 is a target of Xenopus Brachyury: regulation of gastrulation movements via Dishevelled, but not through the canonical Wnt pathway. Development *127*, 2227-2238.

130. Goto, T., and Keller, R. (2002). The planar cell polarity gene strabismus regulates convergence and extension and neural fold closure in Xenopus. Developmental biology *247*, 165-181.

131. Jessen, J.R., Topczewski, J., Bingham, S., Sepich, D.S., Marlow, F., Chandrasekhar, A., and Solnica-Krezel, L. (2002). Zebrafish trilobite identifies new roles for Strabismus in gastrulation and neuronal movements. Nature cell biology *4*, 610-615.

132. Nishimura, T., Honda, H., and Takeichi, M. (2012). Planar cell polarity links axes of spatial dynamics in neural-tube closure. Cell *149*, 1084-1097.

133. Shindo, A., and Wallingford, J.B. (2014). PCP and septins compartmentalize cortical actomyosin to direct collective cell movement. Science *343*, 649-652.

134. Discher, D.E., Janmey, P., and Wang, Y.L. (2005). Tissue cells feel and respond to the stiffness of their substrate. Science *310*, 1139-1143.

135. Niessen, C.M., Leckband, D., and Yap, A.S. (2011). Tissue organization by cadherin adhesion molecules: dynamic molecular and cellular mechanisms of morphogenetic regulation. Physiological reviews *91*, 691-731.

136. Hoffman, B.D., Grashoff, C., and Schwartz, M.A. (2011). Dynamic molecular processes mediate cellular mechanotransduction. Nature *475*, 316-323.

137. Geiger, B., Spatz, J.P., and Bershadsky, A.D. (2009). Environmental sensing through focal adhesions. Nature reviews. Molecular cell biology *10*, 21-33.

138. Kanchanawong, P., Shtengel, G., Pasapera, A.M., Ramko, E.B., Davidson, M.W., Hess, H.F., and Waterman, C.M. (2010). Nanoscale architecture of integrin-based cell adhesions. Nature *468*, 580-584.

139. Hall, M.S., Alisafaei, F., Ban, E., Feng, X., Hui, C.Y., Shenoy, V.B., and Wu, M. (2016). Fibrous nonlinear elasticity enables positive mechanical feedback between cells and ECMs. Proceedings of the National Academy of Sciences of the United States of America *113*, 14043-14048.

140. Dupont, S. (2016). Role of YAP/TAZ in cell-matrix adhesion-mediated signalling and mechanotransduction. Experimental cell research *343*, 42-53.

141. Lilja, J., Zacharchenko, T., Georgiadou, M., Jacquemet, G., De Franceschi, N., Peuhu, E., Hamidi, H., Pouwels, J., Martens, V., Nia, F.H., et al. (2017). SHANK proteins limit integrin activation by directly interacting with Rap1 and R-Ras. Nature cell biology *19*, 292-305.

142. Besser, A., and Safran, S.A. (2006). Force-induced adsorption and anisotropic growth of focal adhesions. Biophysical journal *90*, 3469-3484.

143. Nardone, G., Oliver-De La Cruz, J., Vrbsky, J., Martini, C., Pribyl, J., Skladal, P., Pesl, M., Caluori, G., Pagliari, S., Martino, F., et al. (2017). YAP regulates cell mechanics by controlling focal adhesion assembly. Nature communications *8*, 15321.

144. Horton, E.R., Humphries, J.D., Stutchbury, B., Jacquemet, G., Ballestrem, C., Barry, S.T., and Humphries, M.J. (2016). Modulation of FAK and Src adhesion signaling occurs independently of adhesion complex composition. The Journal of cell biology *212*, 349-364.

145. Kumar, A., Ouyang, M., Van den Dries, K., McGhee, E.J., Tanaka, K., Anderson, M.D., Groisman, A., Goult, B.T., Anderson, K.I., and Schwartz, M.A. (2016). Talin tension sensor reveals novel features of focal adhesion force transmission and mechanosensitivity. The Journal of cell biology *213*, 371-383.

146. Stutchbury, B., Atherton, P., Tsang, R., Wang, D.Y., and Ballestrem, C. (2017). Distinct focal adhesion protein modules control different aspects of mechanotransduction. Journal of cell science *130*, 1612-1624.

147. Grashoff, C., Hoffman, B.D., Brenner, M.D., Zhou, R., Parsons, M., Yang, M.T., McLean, M.A., Sligar, S.G., Chen, C.S., Ha, T., et al. (2010). Measuring mechanical tension across vinculin reveals regulation of focal adhesion dynamics. Nature *466*, 263-266.

148. Franco, S.J., Rodgers, M.A., Perrin, B.J., Han, J., Bennin, D.A., Critchley, D.R., and Huttenlocher, A. (2004). Calpain-mediated proteolysis of talin regulates adhesion dynamics. Nature cell biology *6*, 977-983.

149. Saxena, M., Changede, R., Hone, J.C., Wolfenson, H., and Sheetz, M.P. (2017). Force induced calpain cleavage of talin is critical for growth, adhesion development and rigidity sensing. Nano letters.

150. Assoian, R.K., and Klein, E.A. (2008). Growth control by intracellular tension and extracellular stiffness. Trends in cell biology *18*, 347-352.

151. Yang, N., Williams, J., Pekovic-Vaughan, V., Wang, P., Olabi, S., McConnell, J., Gossan, N., Hughes, A., Cheung, J., Streuli, C.H., et al. (2017). Cellular mechano-environment regulates the mammary circadian clock. Nature communications *8*, 14287.

152. Lo, C.M., Wang, H.B., Dembo, M., and Wang, Y.L. (2000). Cell movement is guided by the rigidity of the substrate. Biophysical journal *79*, 144-152.

153. Alcaraz, J., Xu, R., Mori, H., Nelson, C.M., Mroue, R., Spencer, V.A., Brownfield, D., Radisky, D.C., Bustamante, C., and Bissell, M.J. (2008). Laminin and biomimetic extracellular elasticity enhance functional differentiation in mammary epithelia. The EMBO journal *27*, 2829-2838.

154. Leight, J.L., Wozniak, M.A., Chen, S., Lynch, M.L., and Chen, C.S. (2012). Matrix rigidity regulates a switch between TGF-beta1-induced apoptosis and epithelial-mesenchymal transition. Molecular biology of the cell *23*, 781-791.

155. Paszek, M.J., Zahir, N., Johnson, K.R., Lakins, J.N., Rozenberg, G.I., Gefen, A., Reinhart-King, C.A., Margulies, S.S., Dembo, M., Boettiger, D., et al. (2005). Tensional homeostasis and the malignant phenotype. Cancer cell *8*, 241-254.

156. Leerberg, J.M., Gomez, G.A., Verma, S., Moussa, E.J., Wu, S.K., Priya, R., Hoffman, B.D., Grashoff, C., Schwartz, M.A., and Yap, A.S. (2014). Tension-sensitive actin assembly supports contractility at the epithelial zonula adherens. Current biology : CB *24*, 1689-1699.

157. Yonemura, S., Wada, Y., Watanabe, T., Nagafuchi, A., and Shibata, M. (2010). alpha-Catenin as a tension transducer that induces adherens junction development. Nature cell biology *12*, 533-542.

158. Borghi, N., Sorokina, M., Shcherbakova, O.G., Weis, W.I., Pruitt, B.L., Nelson, W.J., and Dunn, A.R. (2012). E-cadherin is under constitutive actomyosin-generated tension that is increased at cell-cell contacts upon externally applied stretch. Proceedings of the National Academy of Sciences of the United States of America *109*, 12568-12573.

159. Streichan, S.J., Hoerner, C.R., Schneidt, T., Holzer, D., and Hufnagel, L. (2014). Spatial constraints control cell proliferation in tissues. Proceedings of the National Academy of Sciences of the United States of America *111*, 5586-5591.

160. Kim, N.G., Koh, E., Chen, X., and Gumbiner, B.M. (2011). E-cadherin mediates contact inhibition of proliferation through Hippo signaling-pathway components. Proceedings of the National Academy of Sciences of the United States of America *108*, 11930-11935.

161. Benham-Pyle, B.W., Pruitt, B.L., and Nelson, W.J. (2015). Cell adhesion. Mechanical strain induces E-cadherin-dependent Yap1 and beta-catenin activation to drive cell cycle entry. Science *348*, 1024-1027.

162. Gomez-Escudero, J., Moreno, V., Martin-Alonso, M., de Riquer, M.V.H., Feinberg, T., Colmenar, A., Calvo, E., Camafeita, E., Martinez, F., Oudhoff, M.J., et al. (2017). E-cadherin cleavage by MT2-MMP regulates apical junctional signaling and epithelial homeostasis in the intestine. Journal of cell science.

163. Marinari, E., Mehonic, A., Curran, S., Gale, J., Duke, T., and Baum, B. (2012). Live-cell delamination counterbalances epithelial growth to limit tissue overcrowding. Nature *484*, 542-545.

164. Levayer, R., Dupont, C., and Moreno, E. (2016). Tissue Crowding Induces Caspase-Dependent Competition for Space. Current biology : CB *26*, 670-677.

165. Grieve, A.G., and Rabouille, C. (2014). Extracellular cleavage of E-cadherin promotes epithelial cell extrusion. Journal of cell science *127*, 3331-3346.

166. Chiba, T., Ishihara, E., Miyamura, N., Narumi, R., Kajita, M., Fujita, Y., Suzuki, A., Ogawa, Y., and Nishina, H. (2016). MDCK cells expressing constitutively active Yes-associated protein (YAP) undergo apical extrusion depending on neighboring cell status. Scientific reports *6*, 28383.

167. Saw, T.B., Doostmohammadi, A., Nier, V., Kocgozlu, L., Thampi, S., Toyama, Y., Marcq, P., Lim, C.T., Yeomans, J.M., and Ladoux, B. (2017). Topological defects in epithelia govern cell death and extrusion. Nature *544*, 212-216.

168. Tseng, Q., Duchemin-Pelletier, E., Deshiere, A., Balland, M., Guillou, H., Filhol, O., and Thery, M. (2012). Spatial organization of the extracellular matrix regulates cell-cell junction positioning. Proceedings of the National Academy of Sciences of the United States of America *109*, 1506-1511.

169. Thery, M., Racine, V., Piel, M., Pepin, A., Dimitrov, A., Chen, Y., Sibarita, J.B., and Bornens, M. (2006). Anisotropy of cell adhesive microenvironment governs cell internal organization and orientation of polarity. Proceedings of the National Academy of Sciences of the United States of America *103*, 19771-19776.

170. Higashi, T., and Miller, A.L. (2017). Tricellular junctions: how to build junctions at the TRICkiest points of epithelial cells. Molecular biology of the cell *28*, 2023-2034.

171. Bosveld, F., Markova, O., Guirao, B., Martin, C., Wang, Z., Pierre, A., Balakireva, M., Gaugue, I., Ainslie, A., Christophorou, N., et al. (2016). Epithelial tricellular junctions act as interphase cell shape sensors to orient mitosis. Nature *530*, 495-498.

172. Salomon, J., Gaston, C., Magescas, J., Duvauchelle, B., Canioni, D., Sengmanivong, L., Mayeux, A., Michaux, G., Campeotto, F., Lemale, J., et al. (2017). Contractile forces at tricellular contacts modulate epithelial organization and monolayer integrity. Nature communications *8*, 13998.

173. Affolter, M., and Caussinus, E. (2008). Tracheal branching morphogenesis in Drosophila: new insights into cell behaviour and organ architecture. Development *135*, 2055-2064.

174. Pack, M., Solnica-Krezel, L., Malicki, J., Neuhauss, S.C., Schier, A.F., Stemple, D.L., Driever, W., and Fishman, M.C. (1996). Mutations affecting development of zebrafish digestive organs. Development *123*, 321-328.

175. Wallace, K.N., Akhter, S., Smith, E.M., Lorent, K., and Pack, M. (2005). Intestinal growth and differentiation in zebrafish. Mechanisms of development *122*, 157-173.

176. Ng, A.N., de Jong-Curtain, T.A., Mawdsley, D.J., White, S.J., Shin, J., Appel, B., Dong, P.D., Stainier, D.Y., and Heath, J.K. (2005). Formation of the digestive system in zebrafish: III. Intestinal epithelium morphogenesis. Developmental biology *286*, 114-135.

177. Zhong, T.P. (2005). Zebrafish genetics and formation of embryonic vasculature. Current topics in developmental biology *71*, 53-81.

178. Rubin, D.C. (2007). Intestinal morphogenesis. Current opinion in gastroenterology *23*, 111-114.

179. Zegers, M.M., O'Brien, L.E., Yu, W., Datta, A., and Mostov, K.E. (2003). Epithelial polarity and tubulogenesis in vitro. Trends in cell biology *13*, 169-176.

180. Montesano, R., Schaller, G., and Orci, L. (1991). Induction of epithelial tubular morphogenesis in vitro by fibroblast-derived soluble factors. Cell *66*, 697-711.

181. Xia, Y., Nivet, E., Sancho-Martinez, I., Gallegos, T., Suzuki, K., Okamura, D., Wu, M.Z., Dubova, I., Esteban, C.R., Montserrat, N., et al. (2013). Directed differentiation of human pluripotent cells to ureteric bud kidney progenitor-like cells. Nature cell biology *15*, 1507-1515.

182. Sato, T., Vries, R.G., Snippert, H.J., van de Wetering, M., Barker, N., Stange, D.E., van Es, J.H., Abo, A., Kujala, P., Peters, P.J., et al. (2009). Single Lgr5 stem cells build crypt-villus structures in vitro without a mesenchymal niche. Nature *459*, 262-265.

183. Nguyen-Ngoc, K.V., Shamir, E.R., Huebner, R.J., Beck, J.N., Cheung, K.J., and Ewald, A.J. (2015). 3D culture assays of murine mammary branching morphogenesis and epithelial invasion. Methods in molecular biology *1189*, 135-162.

184. Eiraku, M., Takata, N., Ishibashi, H., Kawada, M., Sakakura, E., Okuda, S., Sekiguchi, K., Adachi, T., and Sasai, Y. (2011). Self-organizing optic-cup morphogenesis in three-dimensional culture. Nature *472*, 51-56.

185. Thery, M. (2010). Micropatterning as a tool to decipher cell morphogenesis and functions. Journal of cell science *123*, 4201-4213.

186. Tozluoglu, M., Tournier, A.L., Jenkins, R.P., Hooper, S., Bates, P.A., and Sahai, E. (2013). Matrix geometry determines optimal cancer cell migration strategy and modulates response to interventions. Nature cell biology *15*, 751-762.

187. Madsen, C.D., Hooper, S., Tozluoglu, M., Bruckbauer, A., Fletcher, G., Erler, J.T., Bates, P.A., Thompson, B., and Sahai, E. (2015). STRIPAK components determine mode of cancer cell migration and metastasis. Nature cell biology *17*, 68-80.

188. Carter, S.B. (1967). Haptotactic islands: a method of confining single cells to study individual cell reactions and clone formation. Experimental cell research *48*, 189-193.

189. Balakirev, M.Y., Porte, S., Vernaz-Gris, M., Berger, M., Arie, J.P., Fouque, B., and Chatelain, F. (2005). Photochemical patterning of biological molecules inside a glass capillary. Analytical chemistry *77*, 5474-5479.

190. Dillmore, W.S., Yousaf, M.N., and Mrksich, M. (2004). A photochemical method for patterning the immobilization of ligands and cells to self-assembled monolayers. Langmuir : the ACS journal of surfaces and colloids *20*, 7223-7231.

191. Kim, M., Choi, J.C., Jung, H.R., Katz, J.S., Kim, M.G., and Doh, J. (2010). Addressable micropatterning of multiple proteins and cells by microscope projection photolithography based on a protein friendly photoresist. Langmuir : the ACS journal of surfaces and colloids *26*, 12112-12118.

192. Azioune, A., Carpi, N., Tseng, Q., Thery, M., and Piel, M. (2010). Protein micropatterns: A direct printing protocol using deep UVs. Methods in cell biology *97*, 133-146.

193. Doyle, A.D. (2009). Generation of micropatterned substrates using micro photopatterning. Current protocols in cell biology *Chapter 10*, Unit 10 15.

194. Welle, A., Gottwald, E., and Weibezahn, K.F. (2002). Patterned polymer surfaces for cell culture applications. Biomedizinische Technik. Biomedical engineering *47 Suppl 1 Pt 1*, 401-403.

195. Thery, M., Pepin, A., Dressaire, E., Chen, Y., and Bornens, M. (2006). Cell distribution of stress fibres in response to the geometry of the adhesive environment. Cell motility and the cytoskeleton *63*, 341-355.

196. Khatau, S.B., Hale, C.M., Stewart-Hutchinson, P.J., Patel, M.S., Stewart, C.L., Searson, P.C., Hodzic, D., and Wirtz, D. (2009). A perinuclear actin cap regulates nuclear shape. Proceedings of the National Academy of Sciences of the United States of America *106*, 19017-19022.

197. Versaevel, M., Grevesse, T., and Gabriele, S. (2012). Spatial coordination between cell and nuclear shape within micropatterned endothelial cells. Nature communications *3*, 671.

198. Pitaval, A., Tseng, Q., Bornens, M., and Thery, M. (2010). Cell shape and contractility regulate ciliogenesis in cell cycle-arrested cells. The Journal of cell biology *191*, 303-312.

199. Pouthas, F., Girard, P., Lecaudey, V., Ly, T.B., Gilmour, D., Boulin, C., Pepperkok, R., and Reynaud, E.G. (2008). In migrating cells, the Golgi complex and the position of the centrosome depend on geometrical constraints of the substratum. Journal of cell science *121*, 2406-2414.

200. Doyle, A.D., Wang, F.W., Matsumoto, K., and Yamada, K.M. (2009). One-dimensional topography underlies three-dimensional fibrillar cell migration. The Journal of cell biology *184*, 481-490.

201. Szabo, A., Melchionda, M., Nastasi, G., Woods, M.L., Campo, S., Perris, R., and Mayor, R. (2016). In vivo confinement promotes collective migration of neural crest cells. The Journal of cell biology *213*, 543-555.

202. Fink, J., Carpi, N., Betz, T., Betard, A., Chebah, M., Azioune, A., Bornens, M., Sykes, C., Fetler, L., Cuvelier, D., et al. (2011). External forces control mitotic spindle positioning. Nature cell biology *13*, 771-778.

203. Thery, M., Jimenez-Dalmaroni, A., Racine, V., Bornens, M., and Julicher, F. (2007). Experimental and theoretical study of mitotic spindle orientation. Nature *447*, 493-496.

204. Connelly, J.T., Gautrot, J.E., Trappmann, B., Tan, D.W., Donati, G., Huck, W.T., and Watt, F.M. (2010). Actin and serum response factor transduce physical cues from the microenvironment to regulate epidermal stem cell fate decisions. Nature cell biology *12*, 711-718.

205. McBeath, R., Pirone, D.M., Nelson, C.M., Bhadriraju, K., and Chen, C.S. (2004). Cell shape, cytoskeletal tension, and RhoA regulate stem cell lineage commitment. Developmental cell *6*, 483-495.

206. DiMasi, J.A., Hansen, R.W., and Grabowski, H.G. (2003). The price of innovation: new estimates of drug development costs. Journal of health economics *22*, 151-185.

207. Uchino, S. (2006). The epidemiology of acute renal failure in the world. Current opinion in critical care *12*, 538-543.

208. Hoste, E.A., and Kellum, J.A. (2006). Acute kidney injury: epidemiology and diagnostic criteria. Current opinion in critical care *12*, 531-537.

209. Zager, R.A. (1997). Pathogenetic mechanisms in nephrotoxic acute renal failure. Seminars in nephrology *17*, 3-14.

210. Markowitz, G.S., and Perazella, M.A. (2005). Drug-induced renal failure: a focus on tubulointerstitial disease. Clinica chimica acta; international journal of clinical chemistry *351*, 31-47.

211. Fored, C.M., Ejerblad, E., Lindblad, P., Fryzek, J.P., Dickman, P.W., Signorello, L.B., Lipworth, L., Elinder, C.G., Blot, W.J., McLaughlin, J.K., et al. (2001). Acetaminophen, aspirin, and chronic renal failure. The New England journal of medicine *345*, 1801-1808.

212. Bunel, V., Tournay, Y., Baudoux, T., De Prez, E., Marchand, M., Mekinda, Z., Marechal, R., Roumeguere, T., Antoine, M.H., and Nortier, J.L. (2017). Early detection of acute cisplatin nephrotoxicity: interest of urinary monitoring of proximal tubular biomarkers. Clinical kidney journal *10*, 639-647.

213. Markowitz, G.S., Fine, P.L., Stack, J.I., Kunis, C.L., Radhakrishnan, J., Palecki, W., Park, J., Nasr, S.H., Hoh, S., Siegel, D.S., et al. (2003). Toxic acute tubular necrosis following treatment with zoledronate (Zometa). Kidney international *64*, 281-289.

214. Harpur, E., Ennulat, D., Hoffman, D., Betton, G., Gautier, J.C., Riefke, B., Bounous, D., Schuster, K., Beushausen, S., Guffroy, M., et al. (2011). Biological qualification of biomarkers of chemical-induced renal toxicity in two strains of male rat. Toxicological sciences : an official journal of the Society of Toxicology *122*, 235-252.

215. Garrett, S.H., Somji, S., Todd, J.H., and Sens, D.A. (1998). Exposure of human proximal tubule cells to cd2+, zn2+, and Cu2+ induces metallothionein protein accumulation but not metallothionein isoform 2 mRNA. Environmental health perspectives *106*, 587-595.

216. Chen, J.C., Stevens, J.L., Trifillis, A.L., and Jones, T.W. (1990). Renal cysteine conjugate beta-lyase-mediated toxicity studied with primary cultures of human proximal tubular cells. Toxicology and applied pharmacology *103*, 463-473.

217. Cukierman, E., Pankov, R., Stevens, D.R., and Yamada, K.M. (2001). Taking cell-matrix adhesions to the third dimension. Science *294*, 1708-1712.

218. Baker, B.M., and Chen, C.S. (2012). Deconstructing the third dimension: how 3D culture microenvironments alter cellular cues. Journal of cell science *125*, 3015-3024.

219. Ghibaudo, M., Di Meglio, J.M., Hersen, P., and Ladoux, B. (2011). Mechanics of cell spreading within 3D-micropatterned environments. Lab on a chip *11*, 805-812.

220. Greiner, A.M., Richter, B., and Bastmeyer, M. (2012). Micro-engineered 3D scaffolds for cell culture studies. Macromolecular bioscience *12*, 1301-1314.

221. Khetan, S., Guvendiren, M., Legant, W.R., Cohen, D.M., Chen, C.S., and Burdick, J.A. (2013). Degradation-mediated cellular traction directs stem cell fate in covalently crosslinked three-dimensional hydrogels. Nature materials *12*, 458-465.

222. Pampaloni, F., Reynaud, E.G., and Stelzer, E.H. (2007). The third dimension bridges the gap between cell culture and live tissue. Nature reviews. Molecular cell biology *8*, 839-845.

223. Khanafer, K., Duprey, A., Schlicht, M., and Berguer, R. (2009). Effects of strain rate, mixing ratio, and stress-strain definition on the mechanical behavior of the polydimethylsiloxane (PDMS) material as related to its biological applications. Biomedical microdevices *11*, 503-508.

224. Zhixin Wang, A.A.V., Nathan D. Gallant (2014). Crosslinking Effect on Polydimethylsiloxane Elastic Modulus Measured by Custom-Built Compression Instrument. Journal of Applied Polymer Science, 1-4.

225. I D Johnston, D.K.M., C K L Tan and M C Tracey (2014). Mechanical characterization of bulk Sylgard184 for microfluidics and microengineering. Journal of Micromechanics and Microengineering *24*, 1-7.

226. Yilmaz, C.O., Xu, Z.S., and Gracias, D.H. (2014). Curved and folded micropatterns in 3D cell culture and tissue engineering. Methods in cell biology *121*, 121-139.

227. Li, Q., Zhang, Y., Pluchon, P., Robens, J., Herr, K., Mercade, M., Thiery, J.P., Yu, H., and Viasnoff, V. (2016). Extracellular matrix scaffolding guides lumen elongation by inducing anisotropic intercellular mechanical tension. Nature cell biology *18*, 311-318.

228. Simon-Friedt, B.R., Wilson, M.J., Blake, D.A., Yu, H., Eriksson, Y., and Wickliffe, J.K. (2015). The RPTEC/TERT1 Cell Line as an Improved Tool for In Vitro Nephrotoxicity Assessments. Biological trace element research *166*, 66-71.

229. Choi, Y.Y., Chung, B.G., Lee, D.H., Khademhosseini, A., Kim, J.H., and Lee, S.H. (2010). Controlled-size embryoid body formation in concave microwell arrays. Biomaterials *31*, 4296-4303.

230. Kandikonda, S., Oda, D., Niederman, R., and Sorkin, B.C. (1996). Cadherin-mediated adhesion is required for normal growth regulation of human gingival epithelial cells. Cell adhesion and communication *4*, 13-24.

231. McClatchey, A.I., and Yap, A.S. (2012). Contact inhibition (of proliferation) redux. Current opinion in cell biology *24*, 685-694.

232. Rodriguez-Fraticelli, A.E., Galvez-Santisteban, M., and Martin-Belmonte, F. (2011). Divide and polarize: recent advances in the molecular mechanism regulating epithelial tubulogenesis. Current opinion in cell biology *23*, 638-646.

233. Lancaster, O.M., and Baum, B. (2011). Might makes right: Using force to align the mitotic spindle. Nature cell biology *13*, 736-738.

234. Baena-Lopez, L.A., Baonza, A., and Garcia-Bellido, A. (2005). The orientation of cell divisions determines the shape of Drosophila organs. Current biology : CB *15*, 1640-1644.

235. Lu, C., Wu, N., Jiao, X., Luo, C., and Cao, W. (2003). Micropatterns constructed from Au nanoparticles. Chemical communications, 1056-1057.

236. Yan, J., Sun, Y., Zhu, H., Marcu, L., and Revzin, A. (2009). Enzyme-containing hydrogel micropatterns serving a dual purpose of cell sequestration and metabolite detection. Biosensors & bioelectronics *24*, 2604-2610.

237. Ladoux, B., Anon, E., Lambert, M., Rabodzey, A., Hersen, P., Buguin, A., Silberzan, P., and Mege, R.M. (2010). Strength dependence of cadherin-mediated adhesions. Biophysical journal *98*, 534-542.

238. Enemchukwu, N.O., Cruz-Acuna, R., Bongiorno, T., Johnson, C.T., Garcia, J.R., Sulchek, T., and Garcia, A.J. (2016). Synthetic matrices reveal contributions of ECM biophysical and biochemical properties to epithelial morphogenesis. The Journal of cell biology *212*, 113-124.

239. Salas, P.J., Vega-Salas, D.E., and Rodriguez-Boulan, E. (1987). Collagen receptors mediate early events in the attachment of epithelial (MDCK) cells. The Journal of membrane biology *98*, 223-236.

240. Junker, J.L., and Heine, U.I. (1987). Effect of adhesion factors fibronectin, laminin, and type IV collagen on spreading and growth of transformed and control rat liver epithelial cells. Cancer research *47*, 3802-3807.

241. Bershadsky, A., Kozlov, M., and Geiger, B. (2006). Adhesion-mediated mechanosensitivity: a time to experiment, and a time to theorize. Current opinion in cell biology *18*, 472-481.

242. Carey, S.P., Martin, K.E., and Reinhart-King, C.A. (2017). Three-dimensional collagen matrix induces a mechanosensitive invasive epithelial phenotype. Scientific reports *7*, 42088.

243. O'Brien, L.E., Jou, T.S., Pollack, A.L., Zhang, Q., Hansen, S.H., Yurchenco, P., and Mostov, K.E. (2001). Rac1 orientates epithelial apical polarity through effects on basolateral laminin assembly. Nature cell biology *3*, 831-838.

244. Levental, K.R., Yu, H., Kass, L., Lakins, J.N., Egeblad, M., Erler, J.T., Fong, S.F., Csiszar, K., Giaccia, A., Weninger, W., et al. (2009). Matrix crosslinking forces tumor progression by enhancing integrin signaling. Cell *139*, 891-906.

245. Aragona, M., Panciera, T., Manfrin, A., Giulitti, S., Michielin, F., Elvassore, N., Dupont, S., and Piccolo, S. (2013). A mechanical checkpoint controls multicellular growth through YAP/TAZ regulation by actin-processing factors. Cell *154*, 1047-1059.

246. Sunyer, R., Conte, V., Escribano, J., Elosegui-Artola, A., Labernadie, A., Valon, L., Navajas, D., Garcia-Aznar, J.M., Munoz, J.J., Roca-Cusachs, P., et al. (2016). Collective cell durotaxis emerges from long-range intercellular force transmission. Science *353*, 1157-1161.

247. Engler, A.J., Sen, S., Sweeney, H.L., and Discher, D.E. (2006). Matrix elasticity directs stem cell lineage specification. Cell *126*, 677-689.

248. Reid, S.E., Kay, E.J., Neilson, L.J., Henze, A.T., Serneels, J., McGhee, E.J., Dhayade, S., Nixon, C., Mackey, J.B., Santi, A., et al. (2017). Tumor matrix stiffness promotes metastatic cancer cell interaction with the endothelium. The EMBO journal *36*, 2373-2389.

249. Polte, T.R., Eichler, G.S., Wang, N., and Ingber, D.E. (2004). Extracellular matrix controls myosin light chain phosphorylation and cell contractility through modulation of cell shape and cytoskeletal prestress. American journal of physiology. Cell physiology *286*, C518-528.

250. Zhao, B., Li, L., Tumaneng, K., Wang, C.Y., and Guan, K.L. (2010). A coordinated phosphorylation by Lats and CK1 regulates YAP stability through SCF(beta-TRCP). Genes & development *24*, 72-85.

251. Lienkamp, S.S., Liu, K., Karner, C.M., Carroll, T.J., Ronneberger, O., Wallingford, J.B., and Walz, G. (2012). Vertebrate kidney tubules elongate using a planar cell polarity-dependent, rosette-based mechanism of convergent extension. Nature genetics *44*, 1382-1387.

252. Simoes Sde, M., Mainieri, A., and Zallen, J.A. (2014). Rho GTPase and Shroom direct planar polarized actomyosin contractility during convergent extension. The Journal of cell biology *204*, 575-589.

253. Navis, A., Marjoram, L., and Bagnat, M. (2013). Cftr controls lumen expansion and function of Kupffer's vesicle in zebrafish. Development *140*, 1703-1712.

254. Hou, J., Rajagopal, M., and Yu, A.S. (2013). Claudins and the kidney. Annual review of physiology *75*, 479-501.

255. Yasuda, T., Saegusa, C., Kamakura, S., Sumimoto, H., and Fukuda, M. (2012). Rab27 effector Slp2-a transports the apical signaling molecule podocalyxin to the apical surface of MDCK II cells and regulates claudin-2 expression. Molecular biology of the cell *23*, 3229-3239.

256. Borovac, J., Barker, R.S., Rievaj, J., Rasmussen, A., Pan, W., Wevrick, R., and Alexander, R.T. (2012). Claudin-4 forms a paracellular barrier, revealing the interdependence of claudin expression in the loose epithelial cell culture model opossum kidney cells. American journal of physiology. Cell physiology *303*, C1278-1291.

257. Hanigan, M.H., and Frierson, H.F., Jr. (1996). Immunohistochemical detection of gamma-glutamyl transpeptidase in normal human tissue. The journal of histochemistry and cytochemistry : official journal of the Histochemistry Society *44*, 1101-1108.

258. Hanigan, M.H., Gallagher, B.C., Taylor, P.T., Jr., and Large, M.K. (1994). Inhibition of gamma-glutamyl transpeptidase activity by acivicin in vivo protects the kidney from cisplatin-induced toxicity. Cancer research *54*, 5925-5929.

259. Hanigan, M.H., Lykissa, E.D., Townsend, D.M., Ou, C.N., Barrios, R., and Lieberman, M.W. (2001). Gamma-glutamyl transpeptidase-deficient mice are resistant to the nephrotoxic effects of cisplatin. The American journal of pathology *159*, 1889-1894.

260. Wagner, D.J., Hu, T., and Wang, J. (2016). Polyspecific organic cation transporters and their impact on drug intracellular levels and pharmacodynamics. Pharmacological research *111*, 237-246.

261. Jonker, J.W., and Schinkel, A.H. (2004). Pharmacological and physiological functions of the polyspecific organic cation transporters: OCT1, 2, and 3 (SLC22A1-3). The Journal of pharmacology and experimental therapeutics *308*, 2-9.

262. AA, E.L.-A., and Abdalla, M. (2017). New Insight of OCT2 Regulation as Mediator for Cisplatin-Induced Nephrotoxicity. Asian Pacific journal of cancer prevention : APJCP *18*, 1459-1460.

263. De, S., Kuwahara, S., and Saito, A. (2014). The endocytic receptor megalin and its associated proteins in proximal tubule epithelial cells. Membranes *4*, 333-355.

264. Moestrup, S.K., Cui, S., Vorum, H., Bregengard, C., Bjorn, S.E., Norris, K., Gliemann, J., and Christensen, E.I. (1995). Evidence that epithelial glycoprotein 330/megalin mediates uptake of polybasic drugs. The Journal of clinical investigation *96*, 1404-1413.

265. Saito, A., Nagai, R., Tanuma, A., Hama, H., Cho, K., Takeda, T., Yoshida, Y., Toda, T., Shimizu, F., Horiuchi, S., et al. (2003). Role of megalin in endocytosis of advanced glycation end products: implications for a novel protein binding to both megalin and advanced glycation end products. Journal of the American Society of Nephrology : JASN *14*, 1123-1131.

266. Suzuki, T., Yamaguchi, H., Ogura, J., Kobayashi, M., Yamada, T., and Iseki, K. (2013). Megalin contributes to kidney accumulation and nephrotoxicity of colistin. Antimicrobial agents and chemotherapy *57*, 6319-6324.

267. Han, H.J., Sigurdson, W.J., Nickerson, P.A., and Taub, M. (2004). Both mitogen activated protein kinase and the mammalian target of rapamycin modulate the development of functional renal proximal tubules in matrigel. Journal of cell science *117*, 1821-1833.

268. Plaut, M.E., Schentag, J.J., and Jusko, W.J. (1979). Nephrotoxicity with gentamicin or tobramycin. Lancet *2*, 526-527.

269. Laurent, G., Kishore, B.K., and Tulkens, P.M. (1990). Aminoglycoside-induced renal phospholipidosis and nephrotoxicity. Biochemical pharmacology *40*, 2383-2392.

270. Choi, K.H., Kim, T.I., Chong, D.L., Lee, H.Y., and Han, D.S. (2000). Gentamicin induced apoptosis of renal tubular epithelial (LLC-PK1) cells. The Korean journal of internal medicine *15*, 218-223.

271. Chang, R., Emami, K., Wu, H., and Sun, W. (2010). Biofabrication of a three-dimensional liver micro-organ as an in vitro drug metabolism model. Biofabrication *2*, 045004.

272. Canton, I., Cole, D.M., Kemp, E.H., Watson, P.F., Chunthapong, J., Ryan, A.J., MacNeil, S., and Haycock, J.W. (2010). Development of a 3D human in vitro skin co-culture model for detecting irritants in real-time. Biotechnology and bioengineering *106*, 794-803.

ANNEX

Supplementary table 1: list of primers used for qPCR

Gene	Species	Forward 5'-3'	Reverse 5'-3'
INTU	*Canis lupus*	TCCATGTGGCTTATTGGAAAGA	ACCTGGCAAAAGGCACTATC
GPC4	*Canis lupus*	TTGGACCGACTGGTTACTGAT	GGATTATTGCCCTGGTTGGC
Inversin	*Canis lupus*	ATACGGCGGCTACATCAACT	AGGGGAGTGTACCTTTCTTCA
Vangl1	*Canis lupus*	CAAATTCCGAGCAGCCAAGC	CGACCACCAGTCTTGCTCT
Vangl2	*Canis lupus*	TCTACAACCCCGCTTCTCCT	CTCGTTATGGCTGTTGTCCC
Celsr1	*Canis lupus*	GTCGCTGTCACATCTGGCTT	GGGACTCTAGCGCGGGAAC
Celsr2	*Canis lupus*	TACAGCTTCGAGAGGGGGAA	TCCGTGATGATGGTGACACG
Prickle1	*Canis lupus*	TTCTGCTGCCTTGAGTGTGA	GTCGTAGGTCATCTGGGCAT
Fat1	*Canis lupus*	TCTGGACAAGGACAAGGGGA	GTGGATTGCCTTGGTCGGTA
Fuzzy	*Canis lupus*	CCTTCTGGGGATCAAGAGCCTTC	TCTTGGCACCTGGGTCCTCT
Wnt4	*Canis lupus*	CCCGCAGGGCTTCCAGTGGT	TCGCGCACGTCCACGAAGG
Dishevelled1	*Canis lupus*	GGAGCTACTTCACCATCCCG	GCCTCCTCCAGTTCGTAGC
Dishevelled2	*Canis lupus*	ACCCTCGGTGATTTCAAGAGC	CTTCACCACCCCGAAATCC
Dishevelled3	*Canis lupus*	CCCAATGCTGATGATGCCCC	AGCCCGAAATTCTTGGTGGG
Frizzled2	*Canis lupus*	TCCGGCAAGACGTTGCACTCG	CTCACACGGTGGTCTCGCCG
Frizzled3	*Canis lupus*	AGGTCCCGTGATGGCAGGTACA	TCCGTCAGTCGTGACATGCTGC
Frizzled4	*Canis lupus*	GCTCCAGCCAGCTGCAGTTCTTC	CGCACGGGCCTATGGGGATGT
Frizzled5	*Canis lupus*	ATCCACTGCTCGCCCGACCT	GGCGGCAGCGGCTTGTGATA
α-actinin1	*Canis lupus*	GACTACATGCAGCCCGAAGA	ACCATGCCGTGAACGTCTTT
α-actinin4	*Canis lupus*	AAGCTGAGAAAGGACGACCC	GGCCTCAGAGTGCCTACAAT
YAP1	*Canis lupus*	TCCTGATGGATGGGAACAAGC	GTTCATGGCAAAACGAGGGTC
Talin	*Canis lupus*	CGAGAGAGTGTCGAAGGGAG	CTGGCTATACCTGCGCTGC
Vinculin	*Canis lupus*	TCTTACAGGTATGCGAGCGA	GGGCATTGTGAACCAGCATC
Megalin	*Sus scrofa*	ATTCAGATGAGCGGGACTGC	GAAAGCGAGTGGGACAAGTG
ABCB1	*Sus scrofa*	CTGAGACAGGACGTGAGCTG	AAGCCTGGAACCAATAGCCC
ABCC2	*Sus scrofa*	CAGTCCGAGACGTGAACCTG	CAGTGACATGCCCGTGGATA
ABCG2	*Sus scrofa*	GCGTCCGTAGCCCAGATAAT	GCTGCTGAAACACTGGTTGG
OCT2	*Sus scrofa*	CTCCATCGTCACCGAGTTCGAC	AGCAAGAGGCAGAGCTTACG
GGT1	*Sus scrofa*	CAATGTGACCGAGGTGGTCC	CGGTGTGTAGAACTCAGGCTC
INTU	*Sus scrofa*	CGCAAGTTACTAGCTCATCCCT	CTCAACCTGGCAAAAGGCAC
Frizzled5	*Sus scrofa*	CTACCAGCCGTCCTTTAGCC	GAAAGATGATGGGGCGCTCA
Frizzled4	*Sus scrofa*	ACAACTTTCACGCCGCTCAT	CCGAATTCCTTCAGGACGGG
Frizzled3	*Sus scrofa*	TGGAAGCGTTTGGTGGGTAA	CCAACAAAACACACGCCACT
Vangl1	*Sus scrofa*	CGCTTCTACAGCTTGGGACA	GCATTGTTACTGGGGCCATC
Vangl2	*Sus scrofa*	AATGTGGGCCATCTCAGCATC	GTGGAGTTGTTGGTGCTGTTT

Celsr1	*Sus scrofa*	AAGAAAACGGGTCGTCTCCC	CTGTTGAGCACGCAGTGAAG
Celsr2	*Sus scrofa*	GTGACTACTGCGAGACGGAG	GAAGACACCCAGGGCACTAC
Dishevelled1	*Sus scrofa*	ATCACATGGACGAGGAGGAGA	GCAGCTTGGCATTATCGTCAG
Dishevelled2	*Sus scrofa*	ACCCTCGGCGATTTCAAGAG	GACACCAGCCAGGATACCAC
Dishevelled3	*Sus scrofa*	GCTTTCATTGGCTCGGATGTG	AAGGGAGAGGTTGGCCATGT
Prickle1	*Sus scrofa*	AAACCAGAGCAAAGTGTTCGC	CTCCTGTGCAGCATGGAAGA
Fat1	*Sus scrofa*	GGTCAGAGGTGCCAGCTTAG	CGTATTCTCACAAAGCGCCC
Fat2	*Sus scrofa*	TACTGGTCAGAGGTGCCAGC	GGCACATTCGTCAACGTCAC
Four-jointed	*Sus scrofa*	GCGCTGGTTTTTCTGGACAAT	GCTGGTAGAGGCGCAGTAG
Fuzzy	*Sus scrofa*	AAGGAGCTGAGGGCCAGTTA	TCTGTTGCTGCCACCACTC